Challenges and opportunities towards silicon-based all-solid-state batteries

Xiao Zhan [a,1], Miao Li [a,1], Sha Li [a], Xikun Pang [a], Fangqin Mao [a], Huiqun Wang [a], Zhefei Sun [a], Xiang Han [e], Bing Jiang [c], Yan-Bing He [b], Meicheng Li [c], Qiaobao Zhang [a,d,*], Li Zhang [a,*]

[a] State Key Laboratory of Physical Chemistry of Solid Surfaces, College of Chemistry and Chemical Engineering, College of Materials, Collaborative Innovation Centre of Chemistry for Energy Materials (iChEM), Tan Kah Kee Innovation Laboratory, Xiamen University, Xiamen, Fujian 361005, China
[b] Shenzhen All-Solid-State Lithium Battery Electrolyte Engineering Research Center and Shenzhen Geim Graphene Center, Institute of Materials Research (IMR), Tsinghua Shenzhen International Graduate School, Tsinghua University, Shenzhen, China
[c] State Key Laboratory of Alternate Electrical Power System with Renewable Energy Sources, School of New Energy, North China Electric Power University, Beijing102206, China
[d] Shenzhen Research Institute of Xiamen University, Shenzhen 518000 China
[e] College of Materials Science and Engineering, Co-Innovation Center of Efficient Processing and Utilization of Forest Resources, Nanjing Forestry University, Nanjing 210037, Jiangsu, China

ARTICLE INFO

ABSTRACT

Silicon-based all-solid-state batteries (Si-based ASSBs) are recognized as the most promising alternatives to lithium-based (Li-based) ASSBs due to their low-cost, high-energy density, and reliable safety. In this review, we describe in detail the electro-chemo-mechanical behavior of Si anode during cycling, including the lithiation mechanism, volume expansion, dynamic solid-electrolyte-interphase (SEI) reconstruction of Si anode, the evolution and effect of stress in Si-based ASSBs as well. We also comprehensively summarize the development of all-solid-state electrolytes (ASSEs, *e.g.*, LiPON, sulfide, garnet, and polymer) and structural designs of Si anodes (*e.g.*, nano-structure and composite structure) in Si-based ASSBs. Moreover, we elaborate in detail the challenges and strategies towards high-voltage cathodes of Si-based ASSBs for further construction and application of full batteries. Hence, the significant research advancements of Si-based ASSBs from fundamentals to applications are presented in detail. Finally, we propose some rational suggestions and prospects for in-depth research on failure mechanisms and the further development of ASSEs and Si-based anodes in Si-based ASSBs. We hope that this review will provide valuable insights into failure mechanisms and advanced optimization strategies for the development of next-generation Si-based ASSBs, and bridge the gap between fundamental research and practical applications, particularly for the readers who are new to this field and have an interest in it.

1. Introduction

In recent decades, lithium-ion batteries (LIBs) have achieved tremendous development due to their advantages of high energy density, low self-discharge rate, long-term life, and light weight [1,2]. Nowadays, LIBs have been applied a lot in commercial applications, including 3C electronic products, electronic vehicles (EVs), grid storage, and so on [3]. However, conventional LIBs based on liquid electrolytes suffer from electrolyte leakage, flammability, toxicity, *etc.* [4]. And the use of graphite anode with a theoretical specific capacity of only 372 mAh g^{-1} critically limits the energy density of LIBs, which hinders their further development [5]. Safety issue and range anxiety have been two main barriers to the widespread application of EVs [6]. Recently, ASSBs based on advanced ASSEs (*e.g.*, LiPON, sulfide, garnet, and polymer) have been proposed to alleviate the safety anxiety of liquid batteries [7, 8]. Benefiting from the little interfacial side effect, ASSBs could be compatible with high-energy-density anodes, such as lithium-metal (Li-metal) anodes and Si-based anodes, for breaking the bottleneck of the energy density of commercial LIBs [9–13].

Li-metal anodes with ultra-high theoretical specific capacity (3860 mAh g^{-1}) and ultra-low potential (−3.04 V *vs.* standard hydrogen electrode) have been considered as the most potential anode materials [8,14]. However, the application of Li-metal batteries based on ASSEs still faces many issues caused by excess Li. For example, the formation of

* Corresponding authors.
  E-mail addresses: zhangqiaobao@xmu.edu.cn (Q. Zhang), zhangli81@xmu.edu.cn (L. Zhang).
[1] X. Zhan and M. Li contributed equally to this work.

unstable SEI, instability and inhomogeneous contact of interfaces, diffusion limitation of Li-metal, and the growth of lithium dendrites could shorten the life span of the ASSBs [4,15]. Besides, the dramatically rising price of Li mineral and the poor processability of Li-metal anode further impede the development of Li-based ASSBs [16].

Hence, alloy-type anodes (*e.g.*, silicon, tin, aluminum, indium) without excess Li have attracted a great of interest recently [17–20]. Specially, Si-based anode materials possess the highest theoretical specific capacity (4200 mAh g^{-1}) and low potential (0.3 V *vs.* Li$^+$/Li), which are considered as another potential anodes for the next-generation ASSBs [21–23]. Fig. 1(a) compares key aspects of Si-based ASSBs and Li-based ASSBs systems, including cost, energy densities, interface compatibility, processability, *etc.* [16]. Firstly, Si is significantly competitive with Li in terms of resource and cost. For example, the annual production of Si could achieve 8.0 million tons and the price is only $2100 ton^{-1}, whereas the annual production of Li only reaches 0.082 million tons and the price of battery-grade lithium carbonate is up to $17,000 ton^{-1} [16]. Secondly, Si-based ASSBs demonstrate gravimetric and volumetric energy densities of 356 Wh kg^{-1} and 965 Wh L^{-1}, respectively, which are comparable to those of Li-based ASSBs (410 Wh kg^{-1} and 928 Wh L^{-1}, respectively). Next, Si is thermodynamically stable with most ASSEs, whereas Li-metal undergoes drastic chemical reactions with ASSEs, especially sulfide-type ASSEs [24]. Impressively, Si could mix with ASSE to improve the internal ionic conductivity of Si composite anode [23]. However, Li-metal anode generally contacts with ASSEs *via* "piece to piece" connections, which causes a low critical current density (CCD) and finally leads to severe lithium-dendrite growth [5,21]. Lastly, high stacking pressure is usually applied in ASSB to maintain intimate contact between electrode and electrolyte, whereas it also causes a short circuit in Li-based ASSBs [25,26]. In contrast, Si-based ASSBs can adapt to extra stacking pressure and operate at room temperature [27]. Unfortunately, Li-based ASSBs always require elevated temperatures to improve the reaction kinetics [16]. Therefore, Si-based ASSBs are the more promising alternatives to Li-based ASSBs.

Nevertheless, the electro-chemo-mechanical behavior of Si anode still hinders the practical application (Fig. 1(b)) [28,31]. The huge volume expansion of Si anode (> 300%) upon the lithiation process results in long-term issues for Si-based LIBs [28,32,33]. For example, the dramatically expansion/contraction induces substantial stresses during the lithiation/delithiation process, leading to cracks formation and pulverization of Si anode, denoted as "mechanical pulverization" [34, 35]. Furthermore, it causes the disconnection of electronic/ionic surroundings in Si anode as well, denoted as "decay of conductive environment" [36]. Simultaneously, the significant volume variation of Si anode during long-cycling life results in the formation of an unstable SEI layer, denoted as "dynamic SEI reconstruction" [37]. Eventually, Si-based LIBs suffer from critically irreversible capacity loss, low Coulombic efficiency (CE) and the formation of a thick SEI layer [28, 38-40].

Notably, Si-based ASSBs assembled with ASSEs show novel interfacial interactions and electro-chemo-mechanical behaviors, which are more compatible and stable than that assembled with liquid electrolytes [21,22]. Hence, Si-based ASSBs not only possess reliable safety and low cost, but also alleviate the intrinsic electro-chemo-mechanical issues of Si anode [41]. Furthermore, Si-based all-solid-state full batteries with
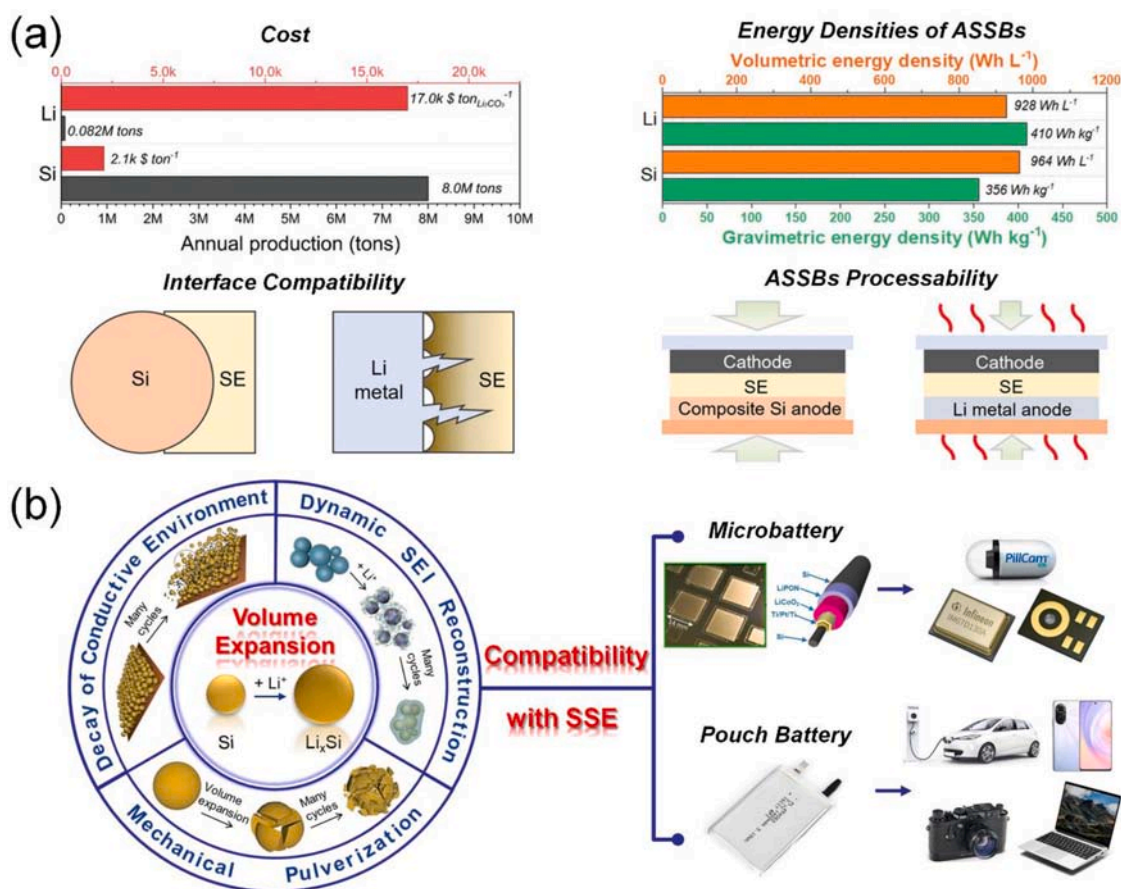

Fig. 1. (a) Comprehensive comparison of Si-based and Li-based ASSBs [16]. (b) The development of Si-based ASSBs from fundamental research to practical applications [28–30]. (a) Reproduced with permission from ref. [16]. Copyright WILEY-VCH, 2022. (b) Reproduced with permission from ref. [28]. Copyright Nature Publishing Group, 2016. Reproduced with permission from ref. [29]. Copyright WILEY-VCH, 2012. Reproduced with permission from ref. [30]. Copyright American Chemical Society, 2012.

various designs (*e.g.*, thin-film or micro battery and pouch battery) are anticipated to cater to diverse applications, such as micro-batteries for micro-electro-mechanical system (MEMS), and pouch batteries for 3C electronic products, EVs, *etc.* [29,30,42-45].

Owing to the multiple advantages, Si-based ASSBs have attracted increasing interests year by year, as indicated by the growing number of related literatures shown in Fig. 2. In this review article, we describe in detail the electro-chemo-mechanical behavior of Si anode, including the lithiation mechanism, volume expansion behavior and dynamic SEI reconstruction of Si anode, as well as the evolution and effect of stress in Si-based ASSBs, which clearly offer an in-depth understanding of the failure mechanism of Si-based ASSBs. And then, we comprehensively summarize the research progress of Si-based ASSBs, including ASSEs, Si-based anode and high-voltage cathode, which could provide advanced optimization strategies for further constructing long-cycle and high-energy-density Si-based all-solid-state full batteries. Finally, the grand challenges and opportunities in the promising field of Si-based ASSBs towards the practical application in energy storage systems are highlighted. Compared to other review articles about Si-based ASSBs, the review comprehensively summarizes the research advancements of all components in Si-based ASSBs (*e.g.*, Si anodes, ASSEs, and cathodes), and provide an in-depth understanding of failure mechanism, which is intended to bridge the gap between fundamental research and practical applications.

2. Electro-chemo-mechanical behavior of Si anode

Since 1976, Si-based anodes have attracted worldwide attention from scientific research institutes and the commercial industry due to their high specific capacity and low lithiation potential [46,47]. However, the electro-chemo-mechanical behavior of Si anode seriously hinders the practical application of Si-based LIBs [48]. The huge volume expansion, severe mechanical pulverization, and drastic cracks generation of Si anode during the lithiation process could further deteriorate the electrochemical performance of Si-based LIBs [49,50]. Hence, the in-depth understanding of failure mechanism in Si-based LIBs is needed. In this chapter, the lithiation mechanism and volume expansion of Si anode are firstly introduced in detail. And then, the dynamic SEI reconstruction at Si anode/ASSE interface is clarified accurately as follows. Lastly, the evolution and effect of stress in Si-based ASSBs are also revealed in detail.

2.1. Lithiation mechanism of Si anode

As is well known, Wen et al. had studied the intermediate phases in the Li-Si system at 415 °C by equilibrium coulometric titration in 1981, which were constituted of $Li_{12}Si_7$, Li_7Si_3, $Li_{13}Si_4$, and $Li_{22}Si_5$, [47]. It seemingly indicated that the lithiation process of Si anode underwent multiple phases (Fig. 3(a), the dotted line) [32]. In fact, the lithiation process of Si anode goes from crystalline Si to amorphous Li_xSi *via* a two-phase transformation, which was firstly discovered by Limthongkul et al. in 2003 [51]. And the mechanism could be also demonstrated by the corresponding galvanostatic voltage profiles of Si electrodes with a relatively flat voltage plateau around 0.1 V *vs.* Li^+/Li (Fig. 3(a), the solid line) [32]. Since the Gibbs free energy of the amorphous phase is lower than that of intermediate phases, Si anode tends to form amorphous Li_xSi rather than intermediate phases during the lithiation process [51]. In 2004, Obrovac and coworkers also verified a similar amorphization process, and even showed that amorphous Li_xSi was crystallized to form a $Li_{15}Si_4$ phase when it was further lithiated below 50 mV (*vs.* Li^+/Li) [52]. And Netz et al. demonstrated the electrochemical phenomena as well [53]. Therefore, the final lithiation product of Si anode is $Li_{15}Si_4$, corresponding to a specific capacity of 3579 mAh g^{-1}, which is different from that of the theoretical $Li_{22}Si_5$ product (4200 mAh g^{-1}).

In 2007, Dahn et al. employed an *in situ* X-ray diffraction (XRD) to reveal the lithiation mechanism of Si anode (Fig. 3(b-c) [54]. Fig. 3(b) presents the *in situ* XRD of the first cycle during the lithiation/delithiation process [54]. Upon the first lithiation process, the intensities of peaks corresponding to Si(111), Si(220), and Si(311) gradually decrease, which indicates that crystalline Si transforms into an amorphous Li_xSi. And these Si peaks almost disappear after the 19th scan cycle. Meanwhile, two new peaks representing $Li_{15}Si_4(332)$ and $Li_{15}Si_4(431)$ appear, demonstrating that highly lithiated amorphous Si crystallizes to the $Li_{15}Si_4$ phase. Upon the initial delithiation process, the intensities of peaks attributing to $Li_{15}Si_4(332)$ and $Li_{15}Si_4(431)$ decrease and the peaks finally disappear. And no crystalline Si peaks could be found during the first delithiation process, which suggests that the crystalline $Li_{15}Si_4$ is delithiated to form an amorphous Li_xSi, and finally transforms to amorphous Si. The first lithiation process is characterized by *in situ* XRD techniques and galvanostatic discharge tests, both of which display the same trend that crystalline Si forms an amorphous phase (Fig. 3(c)) [54].

In addition, the lithiation mechanism of amorphous Si anode was also investigated by Dahn et al., and the lithiation/delithiation process
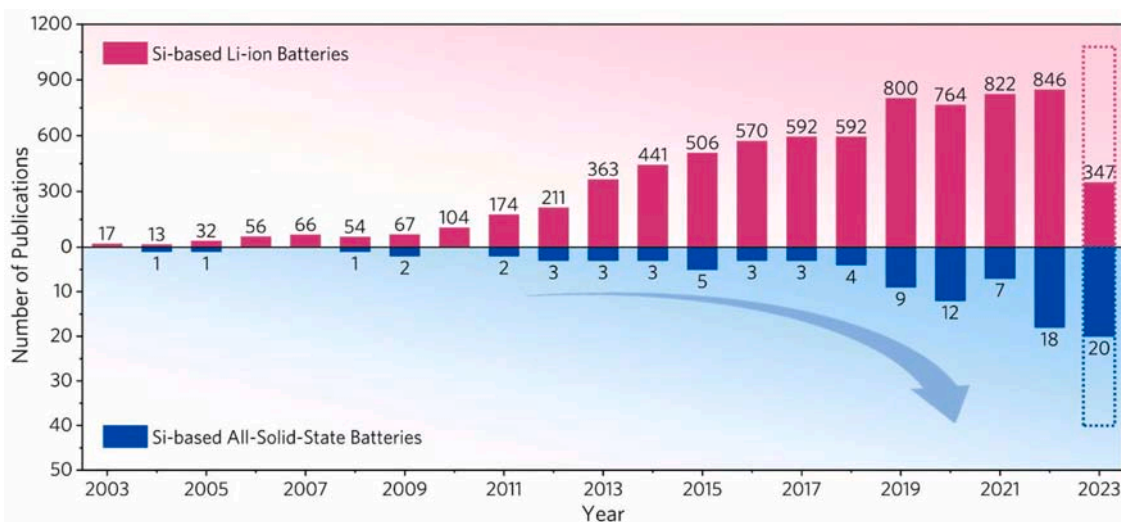

Fig. 2. Bar charts of publication trends for Si-based Li-ion batteries and Si-based all-solid-state batteries applied into energy-related fields, showing advancements in Si-based anode materials (Data collected from Web of Science, including Jun.−2023 and expected publications in the year of 2023 and by using the keywords "silicon anode, lithium-ion battery", and "silicon anode, lithium-ion batteries, all-solid-state electrolyte", respectively).
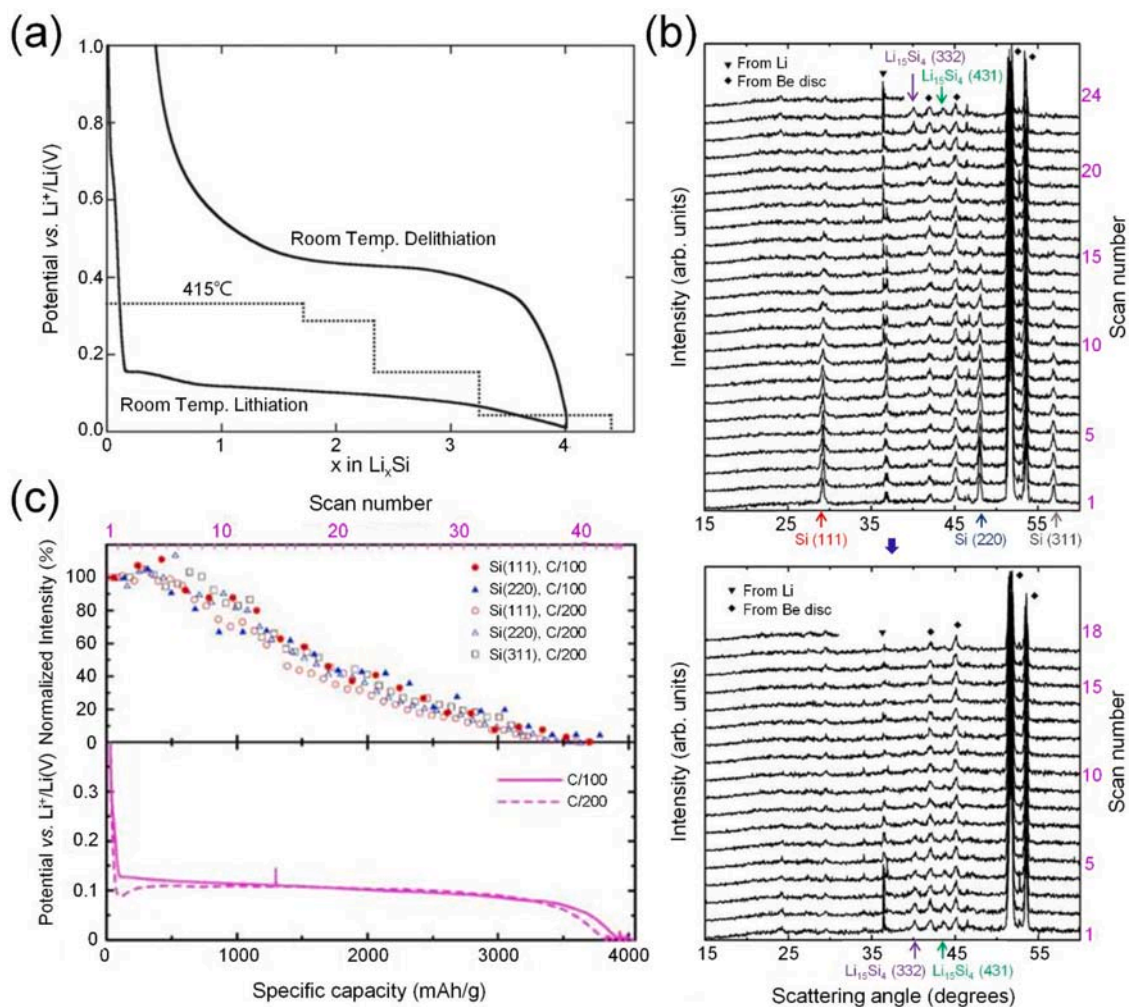
Fig. 3. (a) Coulometric titration curve of Li-Si system at 415 °C (dotted line) and typical galvanostatic charge/discharge of Si anode at room temperature (solid line) [32]. (b) Plots of *in situ* XRD patterns collected during the cycling of the test cell at C/100. The images above and below show XRD scans of the first discharge (upper panel) and the first charge (bottom panel), respectively [54]. (c) Normalized Si Bragg peak intensity *vs.* specific capacity and potential *vs.* specific capacity profiles for cell#1 cycled at C/100 and cell#2 cycled at C/200, respectively [54]. (a) Reproduced with permission from ref. [32]. Copyright WILEY-VCH, 2013. (b, c) Reproduced with permission from ref. [54]. Copyright The Electrochemical Society, 2007.

was similar to that of crystalline Si [55]. In fact, the volume variation of amorphous Si during cycling is isotropous, which is more homogeneous than crystalline Si [56]. Unfortunately, amorphous Si is difficult for large-scale commercialization due to the complicated manufacture process [57].

2.2. Volume expansion of Si anode

Various types of anodes for LIBs are usually divided into Li-metal anodes, intercalation- and insertion-type anodes, conversion-type anodes, and alloy-type anodes [58,59]. The alloy-type anodes, especially Si anodes, feature high Li storage capacity, yet are accompanied with huge volume expansion during the lithiation process. And the volume variation leads to stress evolution and fracture of Si anodes, eventually causing the capacity decay of Si-based LIBs [59]. Thus, many researchers employ *in situ* visualizing-characterization techniques to capture the volume variation of Si anode, and the results are described as follows.

As is well-known, Si anode has an anisotropic swelling during the lithiation process, which is proved by the *in situ* transmission electron microscopy (*in situ* TEM) [60,61]. Fig. 4(a) displays the liquid and solid open-cells inside a TEM chamber for the *in situ* experiments, where Si nanowires and Si nanoparticles are used as anodes in liquid and solid open-cells, respectively [60]. The morphology evolution of the bent Si

nanowire in the liquid cell along [112] direction before (left panel) and after (right panel) the lithiation process is shown in Fig. 4(b) [60]. Obviously, the shape of Si nanowire is transformed from a cylinder to a widened-dumbbell during the lithiation process [60]. There are two orthogonal directions on the cross-section, *i.e.*, [11_0] and [111_], where the lithiation is much faster along the [11_0] direction than [111_], indicating that Si undergoes an anisotropic swelling process in the liquid cell [60]. And newly formed Li-Si alloy tends to expand to the opposite directions of lithiation, thus leading to fast swelling along the ⟨110⟩ direction [60]. Furthermore, the lithiation process of Si nanowire along [112] direction is showed in Fig. 4(c), and the Si nanowire finally forms a core-shell structure of crystalline-Si@amorphous-Li$_x$Si (c-Si@a-Li$_x$Si) [60]. Due to the poor electrical conductivity of Si, c-Si at the core could not be lithiated completely during the long-term cycling processes. Fortunately, Si could be completely lithiated when combined with phosphorus (P) or carbon (C) due to the improving electronic conductivity, which could enhance the rate and cycle performance of batteries [62,63]. In addition, Xia et al. investigated the damage tolerance of Si nanowires during the lithiation process, which revealed a rapid brittle-to-ductile transition of fracture as the Li-to-Si molar ratio increasing to above 1.5 (Fig. 4(d)) [61]. Cho et al. demonstrated the volume expansion of Si nanoparticles (n-Si) during the lithiation process, revealing that the mechanical stability of n-Si depends on their
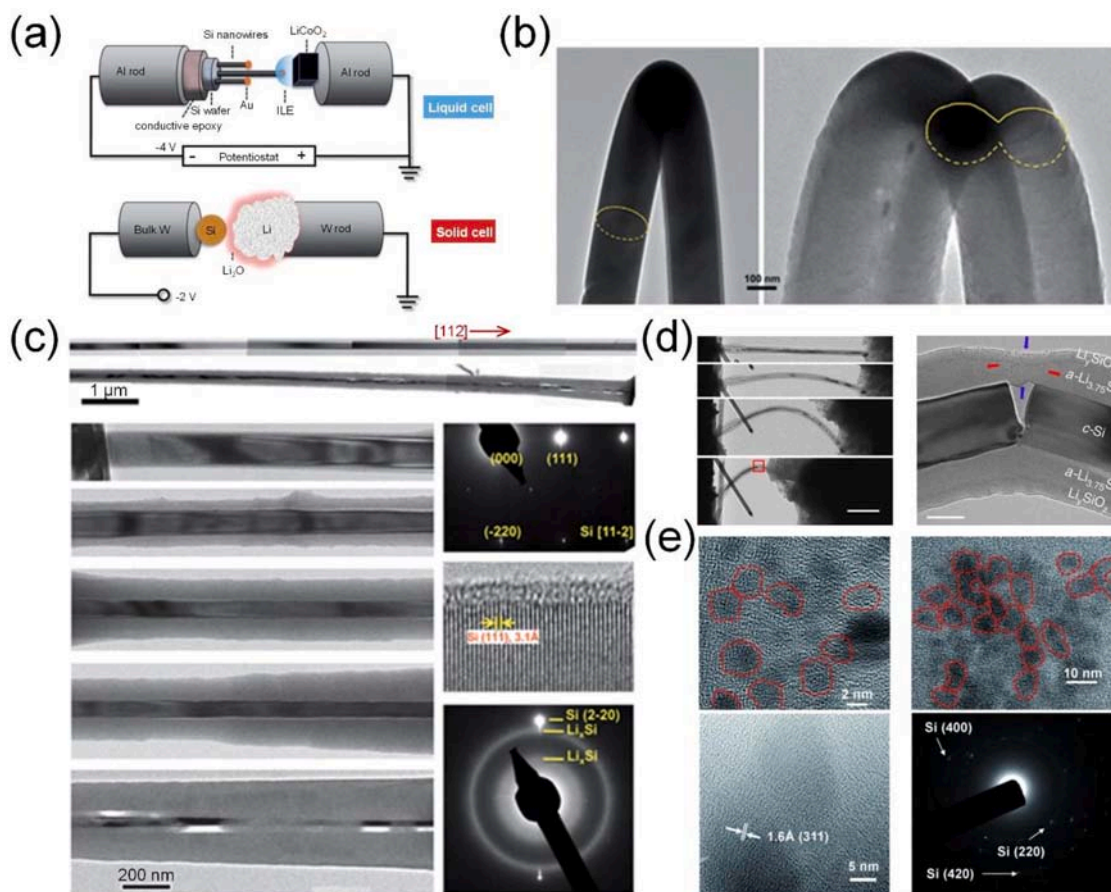
Fig. 4. (a) Schematic illustrations of *in situ* TEM electrochemical experiments. Liquid cell (upper panel): Si nanowires, room temperature ionic liquid electrolyte and LiCoO$_2$ were used as anode, electrolyte and cathode, respectively. Solid cell (bottom panel): Si nanoparticles, thin Li$_2$O layer and Li metal were used as working electrode, solid-state electrolyte and counter electrode, respectively [60]. (b) Anisotropic swelling of bent Si nanowire before (left panel) and after (right panel) lithiation [60]. (c) Core-shell lithiation manner of Si nanowire along with [112] direction [60]. (d) A process of axial compression shown by sequential TEM images (scale bar, 1 mm); a sharply kinked region indicated by the red box and zoom-in TEM image [61]. (e) *Ex situ* TEM images of 5-nm sized Si particles (left upper panel, red lines indicate n-Si crystallites), 10-nm sized particles (right upper panel and left bottom panel, red lines indicate n-Si particles), and selected area diffraction pattern of 10-nm sized particles after 40 cycles (right bottom panel, arrows indicate crystalline regions). All electrodes were dissembled after fully charging to 1.5 V (after lithium removal) [64]. (a-c) Reproduced with permission from ref. [60]. Copyright Royal Society of Chemistry, 2011. (d) Reproduced with permission from ref. [61]. Copyright Nature Publishing Group, 2015. (e) Reproduced with permission from ref. [64]. Copyright WILEY-VCH, 2010.

particle sizes (Fig. 4(e)) [64]. Notably, the 5-nm (left upper panel) and 10-nm (right upper panel) n-Si nanoparticles from assembled cells after 40 cycles show no particle growth, indicating that the ultra-small particles maintain the original morphology during the lithiation process [64]. And some researches indicated that any dislocations induced by volume variation could be quickly drawn to the surface for an ultra-high specific surface area of ultra-small sized particles [56,65]. Furthermore, the 10-nm sized Si sample shows mixed amorphous/crystalline phases while appears to retain its pristine particle size after cycling (Fig. 4(e), bottom panel) [64]. However, the 20-nm sized Si sample after cycling only presents an amorphous phase with loss of its original morphology [64]. Hence, a critical particle size of 10 nm was put forward, above which the particles firstly formed surface cracks and then fractured due to the swelling induced by the lithiation behavior, and below which the particles neither cracked nor fractured [64].

Moreover, the volume expansion behavior of two-dimension (2D) Si film anodes was observed as well. Song et al. had employed an *in situ* optical system to observe the surface morphology of the Si film, which revealed that the debonding induced by crack-face crushing was a critical factor of failure mechanism [66]. Some researchers also demonstrated that the lithiation process resulted in compressive stress on Si film and the delithiation process resulted in tensile stress, leading to film cracks generation and interface debonding during the long cycle

of battery [67–69]. Hence, it is necessary to develop efficient strategies to avoid or reduce the interface debonding between 2D Si film and current collector, such as designing the three-dimension (3D) structured electrode [70,71].

Unfortunately, extensive *in situ* visualization researches have been conducted for Li-based ASSBs, while that for Si-based ASSBs are still not enough [72]. Therefore, *in situ* or *operando* visualizing characterizations for the volume evolution of Si anode are urgently needed to further reveal the failure mechanism in Si-based ASSBs.

2.3. Dynamic SEI reconstruction of Si anode

The huge volume variations of Si anode during the lithiation/delithiation processes induce the degradation of structure and mechanics, further resulting in continuous fragmentation and reconstruction of the SEI layer [73]. Hence, it is critical to understand the interfacial instability of Si anode during the long-term cycling processes. This section focuses on the long-term impact at the interface brought by the electro-chemo-mechanical behavior of Si anode, such as dynamic SEI reconstruction.

Wang et al. had integrated advanced energy dispersive X-ray spectroscopy (EDS) tomography, cryogenic scanning transmission electron microscopy (cryo-STEM) and chemo-mechanical modeling to study the

progressive growth of SEI in Si nanowires-based battery [74]. They constructed a coin-cell composed of a Si nanowires electrode and a Li-metal electrode, where Li metal provided an excessive Li$^+$ source to eliminate the factor of low-content Li$^+$ [74]. A bare Si electrode was prepared by growing nanowires on stainless steel to ensure good mechanical contact and avoid the influence of additional binder and conductive materials [74]. The morphology evolution of Si nanowires at different cycles has been characterized (Fig. 5(a)) [74]. The diameter of Si nanowires ranged from 60 to 90 nm, and the nano-structure could maintain a conformal morphology during cycling [60]. However, the continuous volume variation during the lithiation/delithiation process

still makes Si nanowires rough and porous, further resulting in a degenerated and unstable SEI layer on the Si surface [74]. As shown in Fig. 5(a), SEI on the Si surface undergoes crumpling, regenerating and accumulative growing, and finally become more thicker [74]. It significantly decreases the Coulombic efficiency and capacity of Si-based battery [28,75,76]. In addition, the chemical compositions of SEI on Si anode include Li$_x$SiO$_y$, Li$_2$O, LiF, Li$_2$CO$_3$, *etc.*, which are revealed by X-ray photoelectron spectroscopy (XPS), secondary ion mass spectrometry, Auger electron spectroscopy, and X-ray neutron reflectometry [75–83]. In liquid-based system, some researches focus on adding electrolyte additives into liquid electrolytes to prolong the cycle life of
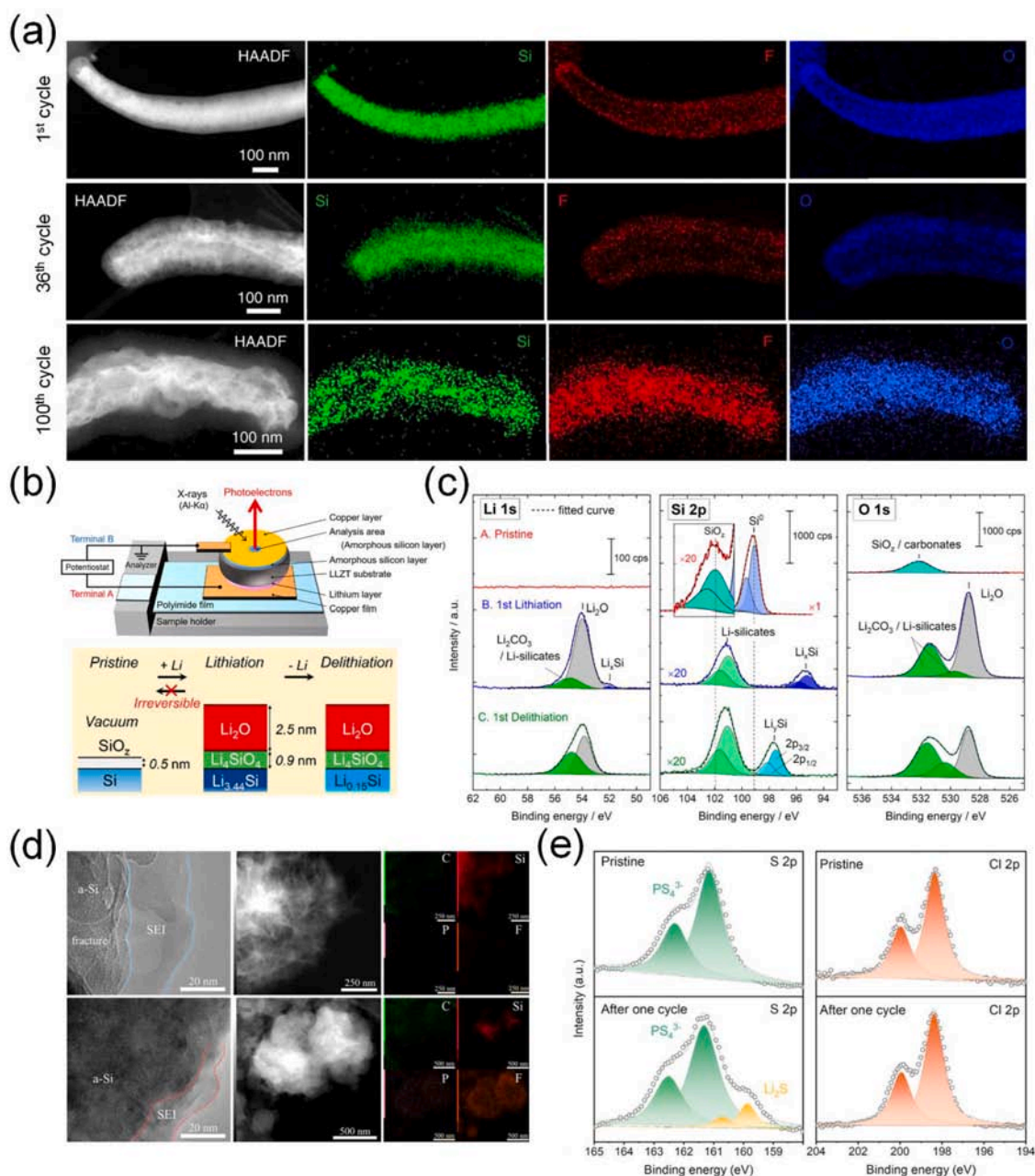

Fig. 5. (a) Cryo-STEM-HAADF images and EDS elemental composition mapping of Si nanowires at different cycles [74]. (b) Schematic illustration of Si‖LLZTO‖Li half-cell and the spectra of *in situ* electrochemical XPS measurements [87]. (c) Li 1 s, Si 2*p*, and O 1 s spectra of the Si electrode at different states: pristine state, after the first lithiation, and after the first delithiation process [87]. (d) TEM images, HADDF-STEM images, and the corresponding elemental distributions of Si@SiO$_2$@LPO@C composite anode after 200 cycles from the liquid battery and the ASSB, respectively [88]. (e) S 2*p* (upper) and Cl 2*p* (bottom) XPS spectra of Si composite anodes at the pristine state (left panel) and after the first cycle (right panel) [16]. (a) Reproduced with permission from ref. [74]. Copyright Nature Publishing Group, 2021. (b, c) Reproduced with permission from ref. [87]. Copyright American Chemical Society, 2020. (d) Reproduced with permission from ref. [88]. Copyright Elsevier, 2022. (e) Reproduced with permission from ref. [16]. Copyright WILEY-VCH, 2022.

Si-based anodes, such as adding fluoroethylene carbonate (FEC), vinylene carbonate (VC), *etc.* [75,84,85]. Notably, the surface chemistry of Si anode also plays an important role in determining electrochemical performance, especially when interacting with electrolytes, binders and conductive agents [86].

Different from liquid electrolytes, the new interfaces between ASSEs and Si anodes are more stable and compatible, which should be discussed separately for different types of ASSEs [16,22,87,88]. As shown in Fig. 5(b-c), Masuda et al. applied *in situ* XPS experiments to characterize the SEI formation process at the interface between Si electrode and $Li_{6.6}La_3Zr_{1.6}Ta_{0.4}O_{12}$ (LLZTO) electrolyte during the first cycle with Li metal as counter electrode [87]. The Li 1 s peaks in the XPS spectra demonstrate several lithiation product composed of Li_2O, Li_2CO_3, Li_4SiO_4, and Li_xSi [89,90]. The Si 2*p* and O 1 s spectra also demonstrate the same lithiation products. Notably, the existences of Li_2O and Li_2CO_3 suggest that a trace amount of oxygen species and carbon dioxide are probably from XPS chamber or reaction product from LLZTO with lithium-silicide surface. Then, they assembled a Si||LLZTO||Li half-cell for the galvanostatic charge/discharge test. The Coulombic efficiency of the half-cell is up to 94% at the first cycle and maintains almost 100% after the second cycle. In general, the few interfacial products and high Coulombic efficiencies of half-cells demonstrate a suppressed side reaction at the interface between Si anode and LLZTO electrolyte [87]. Han et al. proposed a Si@SiO_2@LPO@C composite anode, and applied it to liquid electrolyte and PEO/LATP ASSE, respectively [88]. TEM images in Fig. 5(d) show different structures of the cycled Si composite particles and SEI layers from the disassembled liquid-battery (upper panel) and ASSB (bottom panel) after 200 cycles, respectively [88]. Obviously, the cycled Si composite particles become porous and flake-like in the liquid battery, which results in the continuous generation of SEI and eventually forms a thick layer, mainly consisting of Li_2CO_3 and organic species [88]. Notably, a conformal particle and a uniform SEI layer are observed from the ASSB, and the lithium salt of LiTFSI in ASSE can contribute to forming an SEI layer with enriched LiF nanocrystals, which is mechanically robust and highly ionic conductive [88]. For the PEO-LiTFSI solid electrolyte, LiTFSI are reduced preferentially than PEO [91], thus the generation of LiF from the decomposition of LiTFSI is thermodynamically favorable [92,93]. Furthermore, the interfacial chemistry between Si anode and sulfide-type ASSE was investigated as well [16]. Fig. 5(e) displays the S 2*p* and Cl 2*p* XPS spectra of the Si@Li_6PS_5Cl (Si@ASSE) composite anodes disassembled from Si@ASSE||Li_6PS_5Cl||In-Li half-cells at the pristine state (left panel) and the state after the first cycle (right panel), respectively [16]. The peaks corresponding to the PS_4^{3-} unit and Cl^- ions of argyrodite-type Li_6PS_5Cl are stable no matter before or after the first cycle, suggesting the good chemical interfacial stability between Si and Li_6PS_5Cl ASSE. And the Li_2S product is observed in XPS S 2*p* spectrum, which is generated from a slight decomposition of the ASSE [16]. Furthermore, Huang et al. demonstrated that the initial Coulombic efficiencies (ICE) of Si-based ASSBs with various ASSEs were mostly higher than that of liquid batteries, further indicating the sluggish side reactions at the interfaces between Si anodes and ASSEs [12].

Although the side reaction is reduced at the interface between Si anode/ASSE when compared with Li anode/ASSE and Si anode/liquid electrolyte, the relevant studies for various ASSEs are still not sufficient and deep enough. Hence, more advanced characterization techniques are needed to further figure out the interfacial chemistry between Si anode and ASSEs [19].

2.4. Evolution and effect of stress in Si-based ASSBs

The volume expansion of Si anode during the lithiation process also causes the chemo-mechanical effect on stress evolution, structure fracture and delamination in Si-based batteries, which is critically responsible for the capacity decay of batteries [94–98]. This section clarifies the relevance between stack pressure evolution, chemo-mechanical

degradation, and structural transformation, as well as the relationship between stack pressure and electrochemical behavior in Si-based ASSBs [26,41,99-102]. As shown in Fig. 6(a), a custom-made Si-ASSE|| Li_6PS_5Cl||NCM solid-state cell with an integrated force sensor is designed to *in situ* characterize the stress evolution by McDowell *et al.* [100]. Fig. 6(b) presents the galvanostatic cycling of Si-based ASSBs with the measured uniaxial stress variations (left panel), as well as the corresponding differential capacity (dQ/dV) curves (right panel) [100]. The stress plots indicate that stress is increasing gradually during the lithiation process and reversely decreasing during the delithiation process [100]. Notably, the fully lithiated cell after the first lithiation process exhibits the highest stress, which is attributed to the huger volume expansion of c-Si than a-Si [100]. And the corresponding dQ/dV curves prove the same result, where the voltage of the first cycle is significantly different from that of the subsequent cycles [100]. A relatively large stress hysteresis is observed during the first cycle, and then decreased on subsequent cycles, which is originated from that the Si anode undergoes extensive bond breaking and structural transformation during the first lithiation process (Fig. 6(c)) [100]. The derivative of the stress with time is further investigated (Fig. 6(d)) [100]. The lower slope of the stress curve at the initial stage of charge is resulted by the particle rearrangement within the electrode and/or the expansion of active material into available space [100]. In contrast, the high slope of the stress curve near the end of charge is resulted by the fact that the accommodating space has already been used up and the electrode architecture featured the highest resistance to expansion [100]. In addition, the microparticle-electrode possesses higher stress variations than the nanoparticle-electrode, indicating the importance of size effect, which is agreed with the results of Fig. 4(e) [64].

The effect of internally-generated stress and externally-applied stress of Si-based ASSBs were investigated as well [41,101]. Lee et al. reported that externally-applied compressive stress had affected on the electrochemical performance of Si anodes [101]. Under the condition of free volume expansion (none or little compressive stress), Si particle is allowed to expand unrestricted and no energy is expended for the expansion (Fig. 6(e), upper panel) [101]. When the Si nanoparticle is under the condition of mechanical confinement (a large external pressure), energy is expended to counteract the volumetric strains generated by the expansion of Si, which is reflected on the overpotential of batteries (Fig. 6(e), bottom panel) [101]. As shown in Fig. 6(f), Si-based ASSB under a little compressive press of 3 MPa has a small polarization and could achieve full lithiation, whereas higher compressive press causes higher overpotential and lower capacity of batteries [101]. However, the capacity decreased rapidly under the condition of free volume expansion due to the decay of conductive environment during cycling in ASSBs (Fig. 6(g)) [101]. On the contrary, Si anode delivers a longer and more stable cycle performance under high compressive press, which indicates that the ASSE could inhibit the volume expansion of Si anode (Fig. 6(g)) [101]. Carter et al. also confirmed that constraint-induced stresses in ASSBs caused a voltage shift, further leading to a decreased capacity [41]. Thus, it is universally acceptable to sacrifice part of the capacity to maintain a long and stable cycle performance.

In summary, the volume expansion of Si anode causes the mechanical pulverization and cracks generation of active materials, further leading to dynamic SEI reconstruction and the decay of conductive environment. The issues above vastly decrease the electrochemical performance of Si-based liquid batteries, finally leading batteries failure during early cycling. However, the failure mechanisms of Si-based ASSBs are still not systematic and thorough for the existence of various electrolytes and lack of relevant studies. Hence, we will clarify the failure mechanism of Si-based ASSBs based on the above studies.

Notably, a new interfacial interaction is generated between Si anode and ASSE in Si-based ASSB, among which the chemical inertness interface and 'solid-solid' contact mode would generate new failure mechanism. Due to the reduced interfacial side reaction, the effect of "dynamic
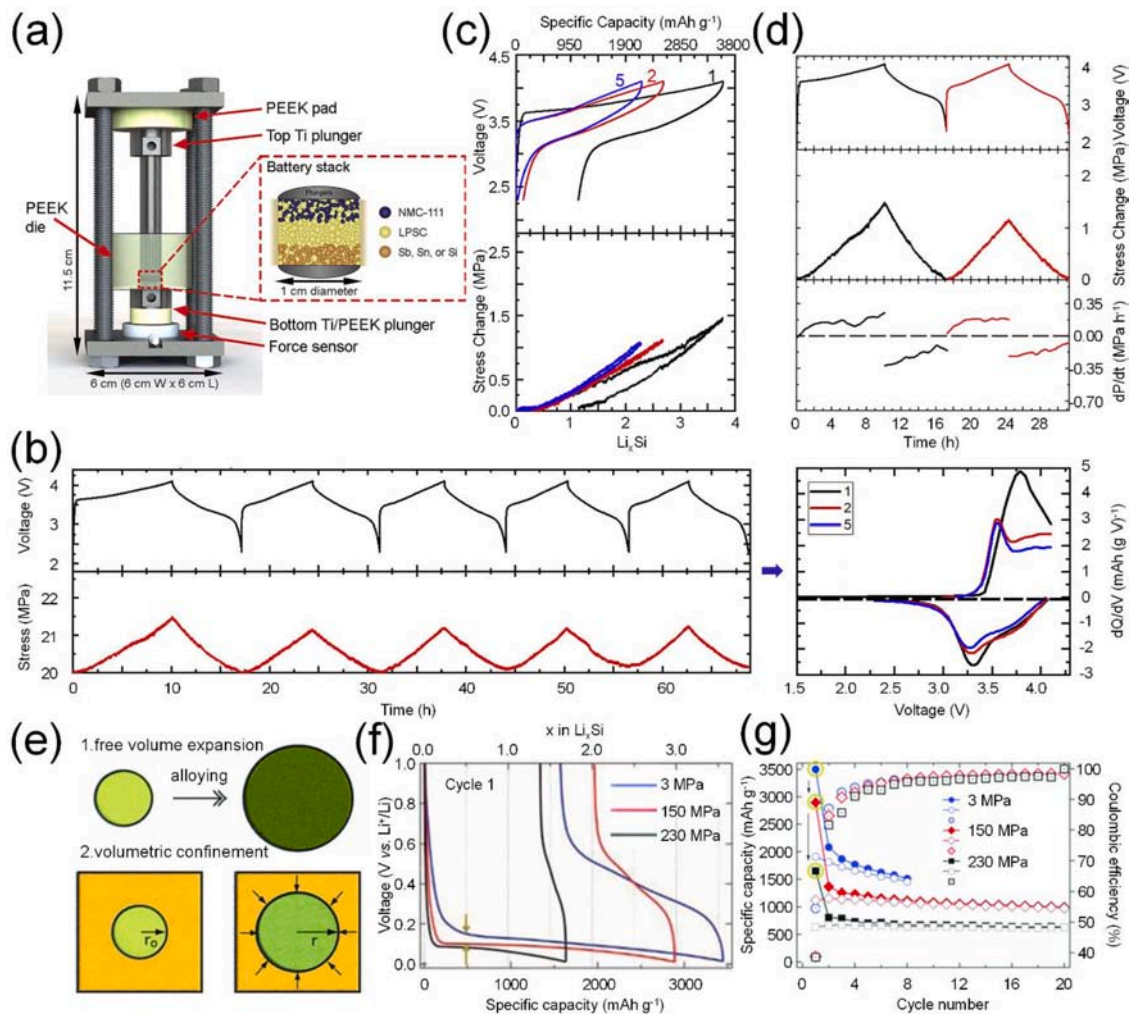
Fig. 6. (a) Schematic of cell stacked by Si-LPSC||LPSC||NCM with a force sensor [100]. (b) Galvanostatic charge/discharge profiles combined with pressure measurement (left panel) and the corresponding differential capacity curves (right panel) [100]. (c) Stress variation curves during cycling [100]. (d) Differential analysis of stress curves [100]. (e) Schematic illustrating of conditions of free volume expansion and volumetric confinement [101]. (f) Voltage profiles of the 1st cycle of Si anode under the compressive pressures of 3, 150 and 230 MPa, respectively [101]. (g) Cycle performance of Si anode under the compressive pressures of 3, 150 and 230 MPa, respectively [101]. (a-d) Reproduced with permission from ref. [100]. Copyright Elsevier, 2021. (e-g) Reproduced with permission from ref. [101]. Copyright The Electrochemical Society, 2012.
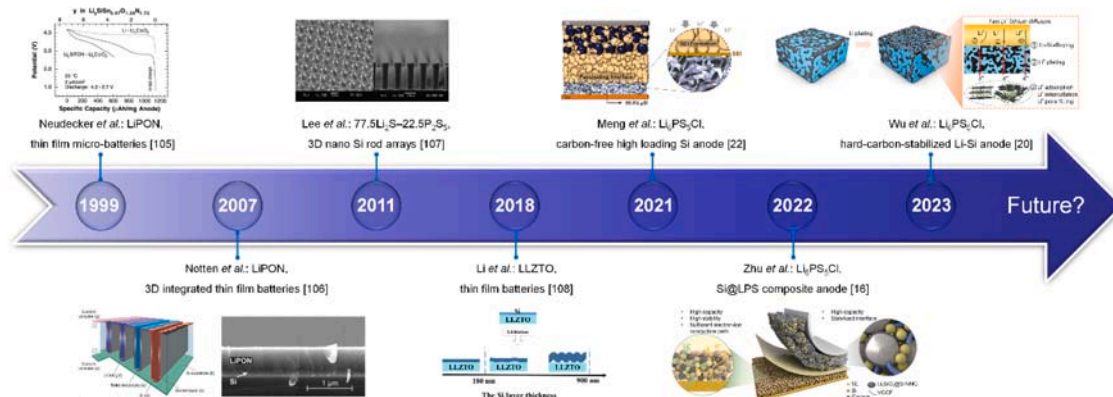

Fig. 7. The historical development of ASSEs in Si-based ASSBs [16,20,22,105-108]. Reproduced with permission from ref. [105]. Copyright Elsevier, 1999. Reproduced with permission from ref. [106]. Copyright WILEY-VCH, 2007. Reproduced with permission from ref. [107]. Copyright Elsevier, 2011. Reproduced with permission from ref. [108]. Copyright American Chemical Society, 2018. Reproduced with permission from ref. [22]. Copyright The American Association for the Advancement of Science, 2021. Reproduced with permission from ref. [16]. Copyright WILEY-VCH, 2022. Reproduced with permission from ref. [20]. Copyright Nature Publishing Group, 2023.

SEI reconstruction" could be weakened. Furthermore, ASSEs possess superior mechanical properties, which could mitigate the issues brought by volume expansion of Si anode [21,103]. However, the conductive environment of electrons and ions should be highly-regarded for huge volume expansion and 'solid-solid' contact at interface. And there exist many strategies to construct an intact interface between Si anode and ASSE, which are introduced in the following chapter.

In general, ASSEs provide a more stable environment for Si anode than liquid electrolyte, whereas the contact problem between Si anode and ASSE should be noticed. Therefore, the failure mechanisms of Si-based ASSBs should be further investigated and the *in situ* or *operando* technologies are also needed to further develop, which could provide guidance for optimization strategy of Si-based ASSBs.

3. Development of ASSEs in Si-based ASSBs

ASSBs have been regarded as the promising conversion and storage devices for their high energy density and reliable safety [9]. The development tendency of Si-based LIBs is from liquid batteries to ASSBs, due to the integrated merits of Si anode and ASSEs [21,104]. Fig. 7 displays the historical development of ASSEs in Si-based ASSBs. In 1999, Neudecker et al. firstly employed silicon tin oxynitride (SiTON) anode and lithium phosphorus oxynitride (LiPON) electrolyte into a thin-film battery, which maintained a high capacity [105]. And in 2007, Notten et al. proposed a 3D integrated structured ASSBs with Si thin-film anode and LiPON ASSE for the first time, which presented a high energy density of about 5 mWh μm^{-1} cm^{-2}, higher than that of planar solid-state thin-film batteries [29,106]. In order to improve the rate performance of batteries at room temperature, sulfide-type ASSEs are considered as one of the most appropriate candidates due to their high ionic conductivity, while LiPON only possesses a lower ionic conductivity of less than 10^{-5} S cm^{-1} at room temperature [10]. In 2011, Lee's group constructed a Si-based ASSB with sulfide-type ASSE of 77.5Li_2S-22.5$P_2$$S_5$, and a 3D nano-Si rods anode to accommodate the volume expansion, which delivered stable capacity with minimal decay for over 20 cycles [107]. Garnet-type LLZTO ASSEs with high ionic conductivity are also employed in Si-based ASSBs. The Li||LLZTO||Si cell based on a 180-nm Si layer exhibited an excellent cycling performance with a capacity retention over 85% after 100 cycles [108]. However, the thin-film electrodes or the LiPON thin-film ASSE are generally synthesized by the physicochemical-deposition method, which are complicated and hard for large-scale manufacture. Thus, simple electrode preparation technologies have been gradually developed to improve production efficiency and decrease production cost.

Nowadays, the Si electrodes are almost sheet-type prepared by wet process or dry process, which could achieve high mass loading and deliver high energy density [109]. Based on this, Meng et al. developed a carbon-free Si sheet anode to avoid the decomposition of sulfide-type ASSE [22]. The μm-Si||$Li_6$$PS_5$Cl||$LiNi_{0.8}$$Co_{0.1}$$Mn_{0.1}$$O_2$ (μ-Si||LiPSCl|| NCM811) full-cell could deliver a capacity retention of 80% after 500 cycles at 5 mA cm^{-2}, demonstrating the overall robustness of μ-Si enabled by ASSBs [22]. Zhu et al. mixed the Si particles and sulfide-type ASSE to improve the ionic conductivity of Si composite anode, and the assembled full battery based on sulfide-type ASSE delivered a high capacity of 145 mAh g^{-1} at C/3 and maintained stably for 1000 cycles, and achieved a cell-level energy density of 285 Wh kg^{-1} [16]. Recently, Wu's group fabricated a hard-carbon-stabilized Li-Si (lithiated Si-HC) anode to improve the electrode kinetics and mechanical stability, and the lithiated Si-HC||$Li_6$$PS_5$Cl|| $LiNi_{0.8}$$Co_{0.1}$$Mn_{0.1}$$O_2$ full-cell delivered an ultrahigh capacity retention of 61.5% even after 5000 cycles [20]. The full batteries are easily fabricated and integrated, endowing them a potential for large-scale commercial application [110].

Herein, current reported systems of Si-based ASSBs with various ASSEs and Si-based anodes are summarized exhaustively in Table 1. It can be discovered that these researches have been pursuing higher energy density, lower cost and larger-scale battery systems by developing

modified strategies. And these strategies generally focus on three aspects, *i.e.*, improving the ionic conductivity of ASSEs (from LiPON-type to sulfide-type ASSEs), increasing the mass loading of Si-based anodes (from thin-film electrode to thick composite electrode), and simplifying the processability of Si-based anodes (from high-cost Si thin-film anode produced by physicochemical deposition to low-cost Si particles anodes). In addition, the thin-film batteries are also applied to MEMS, and large-scale batteries (*e.g.*, pouch batteries, cylindrical batteries) are applied to high-energy and high-power systems, such as EVs, which face greater challenges at present. Hence, the future goal of Si-based ASSBs performance is to achieve higher energy density, higher power density, higher safety and longer life span.

Notably, ASSEs in Si-based batteries are also required towards high overall performance, which are described as follows. For instance, the thickness should be less than 20 μm; the electrochemical stability window should be higher than 5 V to be compatible with high voltage cathode; the ionic conductivity should be higher than 10^{-4} S cm^{-1} at room temperature; along with high ion selectivity (transference number of Li-ion), high chemical stability, thermal stability, robust mechanical property, low processing cost, effortless device integration, and low electronic area-specific resistance (Fig. 8) [9]. Unfortunately, it is difficult to find an ideal ASSE that could meet all of the performance requirements mentioned above, and even maintain these characteristics during long cycling. Up to now, LiPON-type, sulfide-type, oxide-type, and polymer-type ASSEs are verified to be compatible well with Si-based anodes. The following section will mainly discuss the development of the four types of ASSEs in Si-based ASSBs.

3.1. LiPON-type ASSEs

In 1990s, Oak Ridge National Laboratory had led the development of solid-state thin-film batteries [146–148]. Despite the low ionic conductivity of 2~3 μS cm^{-1} and high activation energy (E_a) of ~0.55 eV at room temperature, LiPON-type ASSEs are still endowed with good ionic conduction for their ultrathin properties (<1 μm), which could shorten the ion transport range. In addition, the high electronic resistivity (>10^{14} Ω cm) and wide electrochemical stability window (>5 V) of LiPON guarantee long-term durability in terms of the cycling performance of batteries [149–154]. Generally, glassy SSEs are advantageous with respect to crystalline SSEs due to the absence of grain boundaries, which lead to the electrostatic and structural inhomogeneities, as well as charge transfer impedance [155,156]. Beyond the RF magnetron sputtering, the preparation of LiPON film could be conducted on ion beam sputtering (IBS), metal-organic chemical vapor deposition (MOCVD), plasma-assisted directed vapor deposition, pulsed laser deposition (PLD), electronic beam evaporation and so on, of which the LiPON composition might vary with both the sputter power and the partial nitrogen pressure in the system [154,157-161]. In fact, LiPON-type ASSEs are mostly fabricated by physical and chemical vapor deposition technologies, which could obtain a thin and flat film, favorable interfacial contact as well. There also exist some drawbacks, including the high cost of devices, the difficulty of facilities maintenance, low production efficiency, *etc*.

The structure of thin-film battery is shown in Fig. 9(a), where the Si anode and cathode were both prepared by physical and chemical vapor deposition, and the small-scale manufacturing methods are appropriate for the micro-batteries fabrication [44]. Amorphous thin-films of LiPON are commonly prepared *via* sputtering $Li_3$$PO_4$ in nitrogen atmosphere, resulting in a wide stoichiometric range of $Li_x$$PO_y$$N_z$ (2.6 $\leq x \leq$ 3.5, 1.9 $\leq y \leq$ 3.8, 0.1 $\leq z \leq$ 1.3) [149,154]. And the nitrogen (N) doping improves the stability and ionic conductivity of materials, where the ionic conductivity increases from 7 × 10^{-8} S cm^{-1} (0 at% N) to 3.3 × 10^{-6} S cm^{-1} (6 at% N) at 25 °C [146,152,162].

Lacivita et al. adopted *ab* initio molecular dynamics (AIMD) simulation to generate the structure model of amorphous LiPON, demonstrating that the excess Li accompanying 1(N): 1(O) substitutions would

Table 1

Electrochemical performances of Si-based anodes in various ASSEs.

Si-based anode Type	Preparation method/Thickness	All-solid-state electrolyte Type	Process/Thickness	Ionic conductivity /Temperature	Counter electrode/ Voltage range	Current density/ Temperature	Cycling performance /Capacity retention	Initial CE	Refs.
Amorphous Si film	Sputtering on copper foil 150 nm	LiPON	RF magnetron sputtering 1 μm	2.2×10^{-6} S cm^{-1}	LiMn$_{1.5}$Ni$_{0.5}$O$_4$ 3.0–4.55 V	0.01 mA 25 °C	1st: 47 μAh cm^{-2}	/	[111]
Amorphous Si film	Sputtering 0.06 μm	LiPON	Sputtering 1.5 μm	/	VO-LiPO 0.5–3 V	0.3 μA	1st: 15.7 μAh cm^{-2}	/	[112]
Amorphous Si film	RF sputtering 50–200 nm	LiPON	Sputtering 1.4 μm	2×10^{-6} S cm^{-1} 20 °C	Li$_{1.2}$TiO$_{0.5}$S$_{2.1}$ 1.5–3.2 V	130 μA cm^{-2} 25 °C	capacity loss: −0.01% cycle^{-1} (200 cycles)	/	[44]
					Li 0.05–1 V	100 μA cm^{-2} 25 °C	capacity loss: −0.003% cycle^{-1} (250 cycles)	/	
Si$_{0.7}$V$_{0.3}$	RF sputter deposition 15 nm	LiSiPON 1.2 μm	RF sputter deposition	8.8×10^{-6} S cm^{-1} RT	LiCoO$_2$	2~3.9 V	1500th: ~50 μAh cm^{-2}	/	[113]
Si wafer	Physical vapor deposition (PVD) 500 μm	LiPONB	Cold pressing and sintering	/	Li 0.05–1 V	100 μAh cm^{-2} (2 C) RT	1st: 40 μAh cm^{-2} (571 μAh cm^{-2})	/	[29]
Nano Si @Li$_6$PS$_5$Cl	Ball milling & slurry casting 50 μm	Li$_6$PS$_5$Cl	Ball milling & heat treatment 47 μm	/	In-Li −0.6–0.9 V	0.1 mA cm^{-2}	1st: 2412 mAh g^{-1}	89.3%	[110]
Nano Si@LPSCl	Ball milling	Li$_{5.4}$PS$_{4.4}$Cl$_{1.6}$	Ball milling & annealing	$\sim 8 \times 10^{-3}$ S cm^{-1} RT	In-Li	0.2–0.5 mA cm^{-2} RT	1st: 2412 mAh g^{-1} 50th: 1136 mAh g^{-1}	86.4%	[114]
Li$_x$Si	Cold-pressing 67.4 μm	Li$_6$PS$_5$Cl	Cold-pressing 475 μm	/	Li-In	0.02 C 60 °C	1st: 1560 mAh g^{-1}	/	[115]
Columnar-Si	Physical vapor deposition	Li$_6$PS$_5$Cl	0.15 wt% PTFE ~750 μm	3 mS cm^{-1}	Li 0.01–1 V	0.05 mAcm^{-2}	1st: 2912 mAh g^{-1}	84%	[116]
Si37@C	Slurry-method	Li$_6$PS$_5$Cl	Cold-pressing ~ 750 μm	3 mS cm^{-1}	Li 0.01–2 V	0.07 mA cm^{-2}	1st: > 2570 mAh g^{-1}	72.7%	[117]
10 wt%Si-Graphite	Slurry-method	Li$_6$PS$_5$Cl	/	/	Li	0.2 C 60 °C	1st: 2.20 mAh cm^{-2}	/	[23]
Si/graphite	Roll-pressing	Li$_6$PS$_5$Cl	Cold-pressing	$\sim 3.0 \times 10^{-3}$ S cm^{-1}	Li 0.01–2 V	0.1 C 60 °C	1st: 5.83 mAh cm^{-2}	/	[118]
Si/CNTs/C/ Li$_6$PS$_5$Cl	Slurry casting	Li$_6$PS$_5$Cl	Cold-pressing	2.13×10^{-3} S cm^{-1}	Li 0.01–3 V	50 mA g^{-1} 200 mA g^{-1}	50th: 1226 mAh g^{-1} 200th: 395 mAh g^{-1}	59.7% /	[119]
Si/CNF@LPSCl	Electro-spinning & solution coating 22 μm	Li$_6$PS$_5$Cl	High-energy milling & heat treatment	/	In-Li −0.615–0.88 V	0.1 C 25 °C 0.5 C	1st: 1218 mAh g^{-1} 50th: 84.3%	/	[120]
99.9 wt% μ-Si	Slurry method 27 μm	Li$_6$PS$_5$Cl	30 μm	> 1 mS cm^{-1} RT	NCM811@B	5 mA cm^{-2} (1 C) RT	1st: 2 mAh cm^{-2} 500th: 80%	Average: > 99.9%	[22]
μ-Si/ graphite/ LPSI	Ball milling	LiI-Li$_3$PS$_4$ (LPSI)	Cold-pressing	1.2 mS cm^{-1} 25 °C	In-Li −0.61–1.0 V	C/20 RT	1st: > 1200 mAh g^{-1}	/	[121]
Nano Si@ Li$_7$P$_3$S$_{11}$	Wet chemical	Li$_6$PS$_5$Cl	Solid-state sintering < 50 μm	$\approx$ 2 mS cm^{-1}	In-Li 2.0–3.8 V	0.5 mA cm^{-2} RT	1st: 2067 mAh g^{-1} 200th: 1345 mAh g^{-1}	/	[16]
Si particle	Spray deposition	80Li$_2$S-20P$_2$S$_5$	Mechanical milling	3×10^{-4} S cm^{-1} RT	Li-In	0.06 mA cm^{-2}	1st: 2819 mAh g^{-1} 6th: 2776 mAh g^{-1}	/	[122]
Porous amorphous Si film	Magnetron sputtering 1.55 μm	80Li$_2$S-20P$_2$S$_5$	Cold-pressing ~ 1 mm	/	Li-In 0.01–2 V	10 mA cm^{-2}	1st: > 3000 mAh g^{-1}	/	[123]
Nano Si@ 77.5Li$_2$S-22.5P$_2$S$_5$	Slurry-coating	77.5Li$_2$S-22.5P$_2$S$_5$	Cold-pressing	1.27×10^{-3} S cm^{-1}	Li 0.005–1.5 V	210 mA g^{-1} RT	1st: 1367 mAh g^{-1}	/	[124]
Nano Si-PAN	Slurry-coating	77.5Li$_2$S-22.5P$_2$S$_5$	Cold-pressing	/	Li-In 0.005–0.2 V	C/10 60 °C	1st: 1606 mAh g^{-1}	~84%	[125]
Si nano rod arrays	spin coating & photo lithography & deep reactive ion etching 800 nm	77.5Li$_2$S-22.5P$_2$S$_5$	Ball milling	/	Li	C/2 RT	25th: 3500 mAh g^{-1}	/	[107]
Si/C fiber	Cold-pressing	77.5Li$_2$S-22.5P$_2$S$_5$	Cold-pressing	10^{-3} S cm^{-1} RT	Li-In 0.005–1.5 V	0.1 C 60 °C	50th: > 1000 mAh g^{-1} 70th: ~700 mAh g^{-1}	99.2%	[126]
Si-C-SE	pyrolysis of coal-tar-pitch	77.5Li$_2$S-22.5P$_2$S$_5$	ball milling	/	Li-In 0.005–1.5 V	1st: C/20, 2–49th: C/10, 50–100th: C/5 RT	1st: 1858.7 mAh g^{-1} 100th: 1089.2 mAh g^{-1}	83%	[127]

Table 1 (*continued*)

| Si-based anode Type	Preparation method/Thickness	All-solid-state electrolyte Type	Process/Thickness	Ionic conductivity /Temperature	Counter electrode/ Voltage range	Current density/ Temperature	Cycling performance /Capacity retention	Initial CE	Refs.
Nano-porous Si@LPS	Hand-milled	75Li$_2$S-25P$_2$S$_5$	Cold pressed	/	Li-In −0.58–0.88 V	0.127 mA cm^{-2} 30 °C	1st: 2300 mAh g^{-1}	71%	[128]
Nano-porous Si@Li$_3$PS$_4$	Cold-pressing	75Li$_2$S-25P$_2$S$_5$	Cold-pressing	/	Li-In −0.58–0.88 V	0.127 mA cm^{-2} 30 °C 0.3 mA cm^{-2} 30 °C	1st: 1394 mAh g^{-1} 1st: 1674 mAh g^{-1} 50th: 1494 mAh g^{-1}	59% /	[129]
Nano-porous Si	Cold-pressing	75Li$_2$S-25P$_2$S$_5$	Cold-pressing	/	Li-In −0.58–0.88 V	0.127 mA cm^{-2} 30 °C	1st: 1715 mAh g^{-1}	57%	[130]
u-Si@ LPS	Slurry coating	75Li$_2$S-25P$_2$S$_5$	Milling ∼ 50 μm	5 × 10^{-4} S cm^{-1}	Li-In −0.62–0.88 V	0.3 mA cm^{-2} 30 °C	1st: 3000 mAh g^{-1} 375th: > 1700 mAh g^{-1}	90%	[131]
Si@ Li$_6$PS$_5$Cl	Slurry coating	75Li$_2$S-25P$_2$S$_5$	Cold-pressing	1.4 × 10^{-3} S cm^{-1} 30 °C	Li-In 0.005–1.5 V	0.05 C 30 °C	1st: 3246 mAh g^{-1}	/	[132]
Li-Si	Cold-pressing 25 μm	75Li$_2$S-25P$_2$S$_5$	Cold-pressing 350 μm	5.11 × 10^{-4} S cm^{-1}	Sulfur@SSE 0.5–3.7 V	200 μA	1st: 1510 mAh g^{-1}	/	[133]
μ-Si@LPS	Slurry method	75Li$_2$S-25P$_2$S$_5$	Mechanical milling ∼75 μm	5 × 10^{-4} S cm^{-1} RT	Li-In	0.3 mAh cm^{-2} −0.58–0.88 V	1st: 3412 mAh g^{-1} 140th: 2184 mAh g^{-1} (64%)	/	[134]
Li$_{4.4}$Si	Ball milling	70Li$_2$S-30P$_2$S$_5$	Cold-pressing	∼3 × 10^{-5} S cm^{-1}	Li$_4$Ti$_5$O$_{12}$ 1–2.5 V	50 μA 100 μA	∼80 mAh g^{-1} ∼50 mAh g^{-1}	/	[135]
Amorphous Si	Magnetron sputtering, 300 nm	70Li$_2$S-30P$_2$S$_5$	Cold-pressing	1.5 × 10^{-3} S cm^{-1}	In-Li 0.01–1.2 V	0.1 mA cm^{-2}	1st: > 3000 mAh g^{-1}	/	[136]
Li$_2$SiS$_3$- 10 wt% FeS film	Pulsed laser deposition (PLD) 1 μm	70Li$_2$S-30P$_2$S$_5$	Cold-pressing	/	In-Li −0.615–2 V	0.01 C RT	1st: 1300 mAh g^{-1}	∼ 100%	[137]
Si@Li$_7$P$_3$S$_{11}$	Liquid phase reaction	70Li$_2$S-30P$_2$S$_5$	Cold-pressing	10^{-3} S cm^{-1}	Li	50 mA g^{-1} RT	1st: 1049.9 mAh g^{-1} 35th: 904.8 mAh g^{-1} (86.2%)	/	[138]
Si$_3$N$_4$	Pulsed laser deposition (PLD) 200 nm	70Li$_2$S-30P$_2$S$_5$	/	/	Li-In	0.1 C (charge) 0.2 C (discharge)	1st: 1800 mAh g^{-1} 100th: 1300 mAh g^{-1}	> 80%	[139]
Li$_{4.4}$Ge$_x$Si$_{1-x}$	High-energy ball-milling	60Li$_2$S-40SiS$_2$	Cold-pressing	1.8 × 10^{-4} S cm^{-1} RT	LiCo$_{0.3}$Ni$_{0.7}$O$_2$@SSE 2.3–4.1 V	64 μA cm^{-2}	190 mAh g^{-1}	/	[140]
Si film	Radio frequency sputtering 50 nm	LLZTO	Uniaxial compression & sintering ∼ 550 μm	0.3 mS cm^{-1} 25 °C 3 mS cm^{-1} 80 °C	Li 0.05–1.5 V	170 mA g^{-1} 80 °C	1st: 2702 mAh g^{-1} 100th: 1200 mAh g^{-1}	54%	[141]
thin Si layer	Direct current magnetron Sputtering 180 nm	LLZTO	1 mm	/	Li	8 μA cm^{-2} RT	1st: 3492 mA h g^{-1} 100th: 2968 mAh g^{-1} (85%)	/	[108]
Si layer	Plasma-enhanced chemical vapor deposition 1 um	LLZAO	Solid-state sintering	4 × 10^{-4} S cm^{-1} RT	Li-Sn	0.66 mAh cm^{-2} 0.001–1.5 V	1st: 2685 mA h g^{-1}	83.2%	[142]
Nano Si@ micro- MOF	Hydrothermal	PVDF/ PEO/ LLZTO	Solution casting 60 μm	8.1 × 10^{-5} S cm^{-1} 25 °C	Li 0.01–1.5 V	200 mA g^{-1} 60 °C	1st: 1416 mAh g^{-1}	72%	[143]
Si@ SiO$_2$@ LPO@ C	Slurry-coating	PEO/ LATP	∼ 50 μm	2.86 × 10^{-5} S cm^{-1} 50 °C	Li	0.2 A g^{-1} 50 °C 0.5 A g^{-1} 50 °C	1st: 2482.1 mAh g^{-1} 1st: 2279.3 mAh g^{-1} 200th: 1001.9 mAh g^{-1}	88.7% /	[88]
Si-N-MXene	Slurry coating	PEO@ LATP	∼50 μm	3.4 × 10^{-4} S cm^{-1} 50 °C	Li	1st-10th: 0.2 A g^{-1}, 11th-100th: 0.4 A g^{-1} 50 °C	1st: 2305 mAh g^{-1} 10th: 1362 mAh g^{-1} 100th: 881 mAh g^{-1}	/	[144]
Amorphous Si	Cold-pressing	15NaI-LiBH$_4$	Cold-pressing	5 × 10^{-6} S cm^{-1} RT	Li 0.1–1.5 V	2.5 μA cm^{-2} RT 12.7 μA cm^{-2} RT 12.7 μA cm^{-2} 60 °C	1st: 3000 mAh g^{-1} 1st: 1300 mAh g^{-1} 1st: 3000 mAh g^{-1}	/	[145]
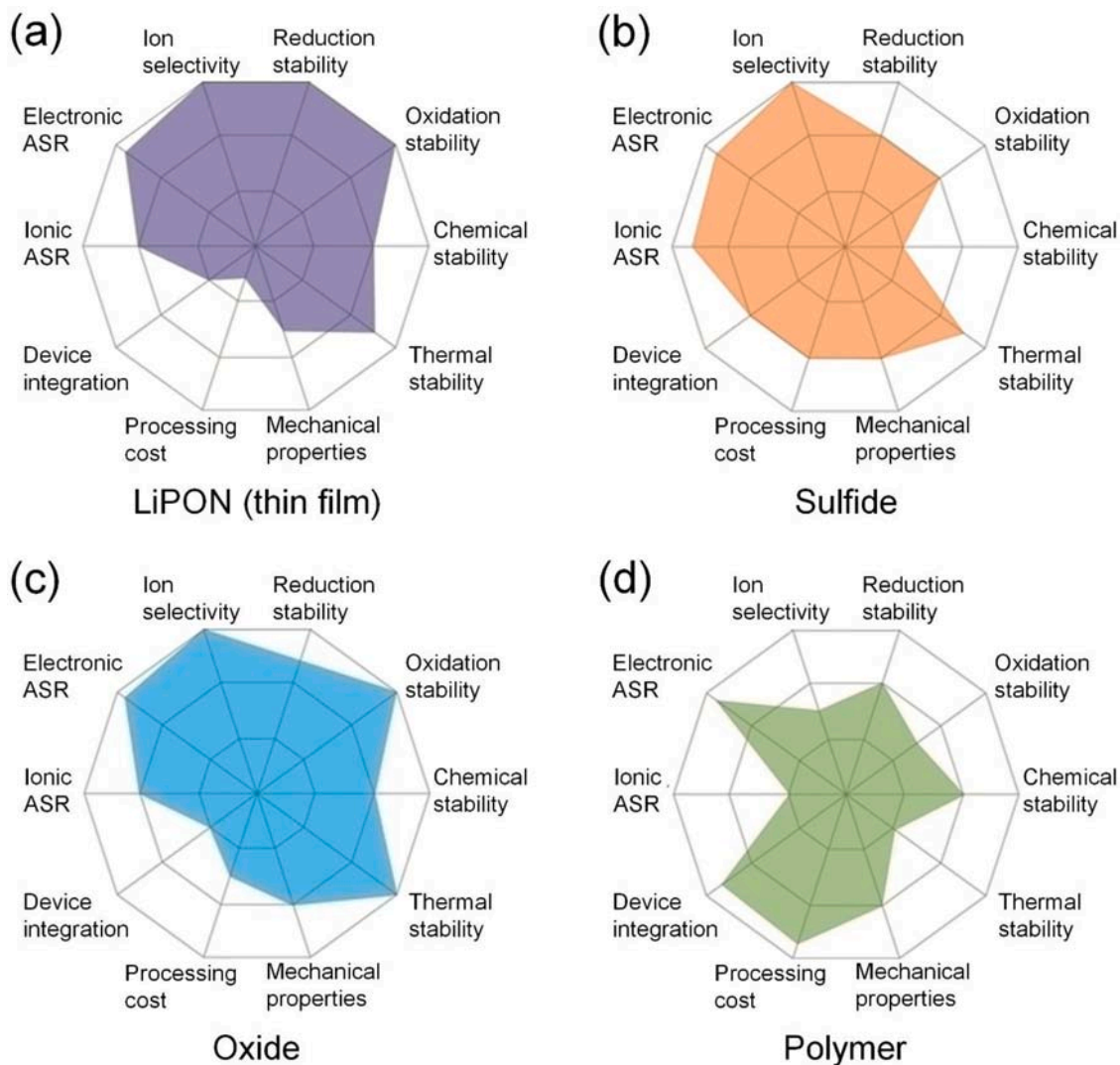
Fig. 8. Radar plots of the performance properties of different ASSEs [9]. (a) LiPON ASSEs (thin-film). (b) Sulfide ASSEs. (c) Oxide ASSEs. (d) Polymer ASSEs. ASR: area-specific resistance. Reproduced with permission from ref. [9]. Copyright Nature Publishing Group, 2017.

introduce extra carriers and the energetically-favored N-bridging substitutions could condense phosphate units and densify the structure [164]. And Meng et al. combined solid-state nuclear magnetic resonance (NMR) spectroscopy and AIMD simulation approach to study the structure of LiPON and mechanism of Li$^+$ transport in LiPON (Fig. 9 (b-c)) [163]. As shown in Fig. 9(b), the ^{31}P chemical shift for crystallized-LPO (c-LPO) exhibits a sharp peak at 9.6 ppm, corresponding to the orthophosphate tetrahedra structure with four non-bridging oxygens, Q^0 [163]. After amorphization, the amorphous-LPO (a-LPO) showed a broadening Q^0 peak, indicating the structural disorder [163]. The shoulder peak appearing at $\approx$ 0 ppm is attributed to dimeric P$_2$O$_7$ units, Q^1. And the chemical shift for Q^1 is slightly higher than that observed in a pyrophosphate crystal, indicating a result of a redistribution of the electron density with higher cation concentration [163]. The MAS ^{31}P spectrum of a LiPON film is similar to the a-LPO spectra with the predominant intensity at 9.1 ppm and a small tail around 3 ppm, comfortably assigned to Q$_0^0$ and Q$_0^1$ phosphate species, respectively [163]. There are additional shoulders of higher chemical shift that are presumed to be phosphorus (P) bonded to N, assigned to Q$_1^0$ and Q$_1^1$ phosphate species (Fig. 9(b)) [163]. Furthermore, they employ AIMD to generate an amorphous structure with a stoichiometry of Li$_{2.9}$PO$_{3.5}$N$_{0.31}$, and the relationship between bonding environment and electron shielding in the structure is calculated by the gage including

projector augmented wave (GIPAW) [163]. The result shows that incorporation of N resulted in an increased δ_{iso}(chemical shift of isolated PO$_4^{3-}$ tetrahedra), whereas the lowest $\delta_{iso}$is associated with bridging oxygen, consistent with results from the structural database (Fig. 9(c)) [163]. These results demonstrated the glassy structure as primarily isolated phosphate monomers with N incorporated in both apical and as bridging sites in phosphate dimers [163]. In addition, Meng et al. also investigated the SEI between Li metal and LiPON by cryo-EM and XPS depth profiling, identifying the SEI compositions to be Li$_2$O, Li$_3$N and Li$_3$PO$_4$ with a unique multilayer-mosaic distribution [165].

Limited by the high activity of Li metal, currently successful commercial Li-based thin-film batteries are manufactured in vacuum or inert gas-protecting atmosphere, which raise high-cost and safety issues. Hence, owing to the advantages of Si anode, LiPON-type ASSEs are also employed in Si-based ASSBs [105,106,140]. In order to increase the energy density and power density of micro-batteries, researches focus on the strategies including boron (B) or Si doping of LiPON, matching with high-voltage cathode, and 3D structure designing or intergradation of batteries [29,30,106,111-113,166]. The finite B addition could enhance the chemical and thermal stability of LiPON electrolyte. Pecquenard et al. used physical vapor deposition (PVD) techniques to prepare all-solid-state Li||LiPONB||Si cells, among which the electrochemical behavior of the sputtered Si anode is similar to that of Si anode based on
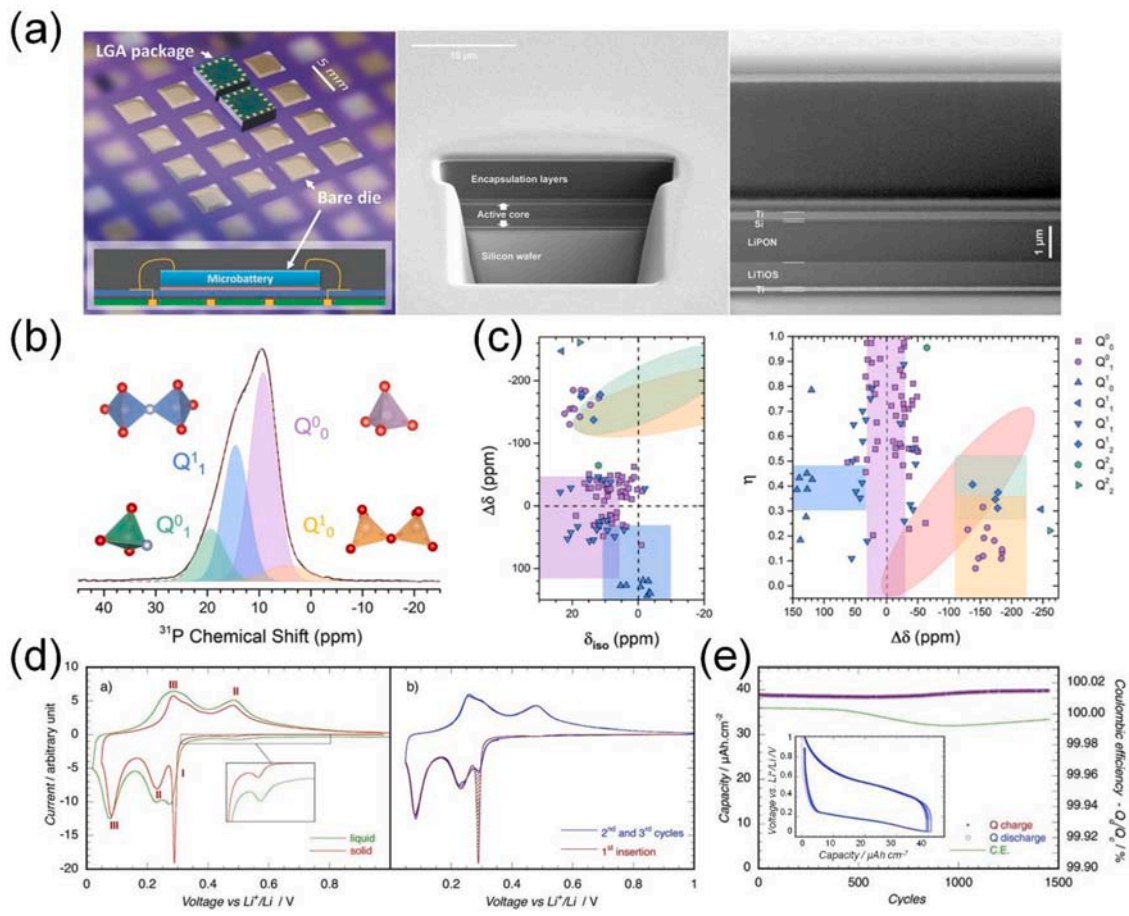
Fig. 9. (a) Schematic of micro-batteries package and focused ion beam (FIB) / scanning electron microscope (SEM) cross section of a thin-film encapsulated lithium-ion micro-battery [44]. (b) ^{31}P MAS NMR spectra of thin-film LiPON spinning at 25 kHz [163]. (c) Anisotropy-isotropic chemical shift and anisotropy-asymmetry correlation maps of the AIMD model grouped by Q_m^n speciation with distinct ranges, where Q_0^0, Q_1^0, Q_0^1, left triangle Q_1^1, inverted triangle Q_1^1, Q_2^2, regular hexagon Q_2^2, right triangular Q_2^2 represent isolated PO_4, isolated PO_3N, dimer PO_4, dimer PO_3N(BO, bridging oxygens), dimer PO_3N, dimer PO_2N_2 (BN, bridging nitrogen), trimer PO_2N_2(BN), and trimer PO_2N_2(BN, BO), respectively [163]. (d) Cyclic voltammetry profiles of Si thin-film anodes during the first lithiation/deliathiation cycle in liquid battery (left panel), and the first, second and third cycles in ASSBs (right panel) [29]. (e) Cycling performance of the Si||LiPONB||Li half-cell at room temperature. Inset: the corresponding voltage curves [29]. (a) Reproduced with permission from ref. [44]. Copyright WILEY-VCH, 2015. (b, c) Reproduced with permission from ref. [163]. Copyright WILEY-VCH, 2020. (d, e) Reproduced with permission from ref. [29]. Copyright WILEY-VCH, 2012.

liquid electrolyte except a very sharp peak observed at 290 mV in the voltage profiles (Fig. 9(d)) [29]. Specifically, the sharp peak indicates a low irreversible capacity (less than 5% *i.e.*, ≈ 1 µAh cm^{-2}) during the first lithiation process, attributing to the reaction products (containing oxidized Si) formed at the interface during the LiPON deposition process. Notably, the cell exhibits an excellent cycle performance and Coulombic efficiency with almost no loss during 1500 cycles (Fig. 9(e)) [29]. Lee's group sequentially deposited a LiCoO$_2$ cathode, a Li$_{1.9}$Si$_{0.28}$P$_{1.0}$O$_{1.1}$N$_{1.0}$ electrolyte (LiSiPON) and a Si$_{0.7}$V$_{0.3}$ anode to build a full cell. The LiSiPON thin-film showed better ionic conductivity of 8.8×10^{-6} S cm^{-1} at room temperature, and was electrochemical stable above 4.5 V [113]. In order to increase the energy density of batteries, Wang et al. constructed a high-voltage LiMn$_{1.5}$Ni$_{0.5}$O$_4$|| LiPON||Si all-solid-state full battery by sputter-deposition technique, which exhibited a high cut-off voltage of 4.55 V [111]. To further increase the energy density of batteries, 3D structure designs of thin-film batteries for accommodating high-loading electrode or easy-integration were developed [106]. Notten et al. fabricated a novel 3D integrated ASSB, among which surface enlargement has been accomplished by electrochemical or reactive ion etching (RIE) in a Si substrate, exhibiting an ultrahigh capacity of 3500 mAh g^{-1} over 60 cycles (Fig. 7, in 2007) [106]. Talin et al. fabricated a core-shell Si||LiPON||LiCoO$_2$ nanobattery and cycled it inside a TEM chamber, where the thinnest electrolyte ($\approx$ 110 nm) endowed the nanobattery with good rate performance and

maximized areal energy density [30]. And void formation at the electrode/electrolyte interface was observed through TEM techniques, indicating the electrical/chemical breakdown. Hence, Si-based ASSBs with LiPON-type ASSE should pay attention to eliminate the issues of decay of ionic conductive environment at the interface. Meng et al. found Li accumulation at the anode/current collector (Si/Cu) and cathode/electrolyte (LiCoO$_2$/LiPON) interfaces during cycling, which can be accounted for the irreversible capacity loss [167]. And Talin et al. also demonstrated the phenomena of Li enrichment/depletion at the interface [168]. Besides, a LiPON-SnO$_2$ composite thin-film has been confirmed to be used as an artificial SEI layer for Si anode in liquid batteries [169].

In summary, thin-film Si-based ASSBs had made great success over the past decades. However, in order to avoid the dramatic volume expansion of Si anode during lithiation and prolong a long-term cycle stability, some researches reduce the operating voltage range at low current density, which cannot provide high energy density and high power to batteries (Table 1). Simultaneously, the further commercial application of Si-based ASSB is limited by the complex fabrication process and high cost for production. Hence, the thin-film micro-batteries of Si-based ASSBs are only appropriate for MEMS, yet are not applied in large-scale electronic devices.

3.2. Sulfide-type ASSEs

Owing to the ultra-high conductivity ($10^{-3} \sim 10^{-2}$ S cm^{-1}) at room temperature, sulfide-type ASSEs are the most popular electrolyte materials for the application of ASSBs [170–172]. Simultaneously, sulfide-type ASSEs also possess favorable flexibility to plastic deformation, making them simple to prepare densely packed and achieve intact interfacial contact (Young's modulus = 18.5 GPa, hardness = 1.9 GPa, and fracture toughness = 0.23 MPa m$^{1/2}$) [173,174]. Nonetheless, the narrow electrochemical stability window, poor chemical compatibility with electrodes, moisture sensitivity and other issues of sulfide ASSEs still restrict their widespread application in ASSBs [170]. Hence, many studies focus on the interface between electrode and electrolyte [172, 175,176]. The sulfide-type ASSEs could be synthesized *via* solid-state reaction, ball milling route and wet chemistry, governed by the important parameters of synthesis condition [177–179].The synthetic processes also make a great influence on the structure of sulfide-type ASSEs, further influencing their electrochemical performance by the structure-property correlation [180–183]. Sulfide-type ASSEs are classified into three types according to the compositions: binary, ternary and quaternary sulfide systems. In particular, binary sulfide systems include Li$_2$S-P$_2$S$_5$ and Li$_2$S-MS$_2$ (M = Ge, Sn, Si); ternary sulfide systems include Li$_2$S-P$_2$S$_5$-MS$_2$ (M = Ge, Sn, Si, Al, *etc.*) and Li$_2$S-P$_2$S$_5$-LiX (X = Cl, Br, I); and quaternary sulfide systems include Li$_2$S-P$_2$S$_5$-MS$_2$-LiX (M = Ge, Sn, Si, Al, *etc.*; X = Cl, Br, I) [184]. Moreover, based on crystalline structures, those sulfide-type ASSEs are defined as thio-LISICON (derived from a LISICON-type γ-Li$_3$PO$_4$ ASSE by replacing oxygen with sulfur), tetragonal-type LGPS, and argyrodite Li$_6$PS$_5$X, respectively [24]. With the deepening of research, sulfide-type ASSEs are thrivingly developed towards polysystems for the increase of ionic conductivities [184]. In 2016, Kanno et al. reported a Li-ion superionic conductor (Li$_{9.54}$Si$_{1.74}$P$_{1.44}$S$_{11.7}$Cl$_{0.3}$) with an exceptionally high ionic conductivity of 25 mS cm^{-1} [185]. In 2019, a single crystal Li-ion conductor Li$_{10}$GeP$_2$S$_{12}$ was synthesized by the self-flux method, which revealed an ultra-high ionic conductivity up to 27 mS cm^{-1} at room temperature along the [001] direction [186]. The ionic conductivities of the state-of-the-art sulfide-type ASSEs are already equivalent to that of traditional liquid electrolytes [10].

Due to the complexity and diversity of sulfide systems, the structures of sulfide-type ASSEs are inconsonant, resulting in different ionic conductivities. For ternary Li$_3$PS$_4$ systems, β-Li$_3$PS$_4$ converted from γ-Li$_3$PS$_4$ after heating shows markedly increase of ionic conductivity [187]. Liang et al. reported a nano-porous β-Li$_3$PS$_4$ with high ionic conductivity of 1.6×10^{-4} S cm^{-1} at room temperature, which indicated that the high surface-to-bulk ratio of nano-porous Li$_3$PS$_4$ can promote surface conductivity [188]. For Li$_2$S-MS$_2$ (M = Ge, Sn, As) ternary systems, heterovalent or aliovalent substitutions are used to increase the ionic conductivity [189–191]. With regard to the ternary Li$_2$S-P$_2$S$_5$-MS$_2$ systems, Kanno et al. prepared a new thio-LISICON type by sintering Li$_2$S, GeS$_2$, and P$_2$S$_5$ in 700 °C in 2001 [192]. And they reported a Li-ion superionic conductor Li$_{10}$GeP$_2$S$_{12}$ (tetragonal-type LGPS) with an ionic conductivity of 1.2×10^{-2} S cm^{-1} at room temperature in 2011, whose structure was different from thio-LISICON-type sulfide, bringing about a higher ionic conductivity [193]. LGPS electrolyte has a 3D skeleton structure and 1D Li-ion conduction pathways along c-axis [194]. And the Li$^+$ hopping direction is nearly isotropic with a low activation energy of 0.22 eV [195]. For ternary Li$_2$S-P$_2$S$_5$-LiX systems, they are known as lithium argyrodites [196,197]. Deiseroth et al. demonstrated 3D Li-ion conduction pathways in lithium argyrodite electrolytes by molecular dynamics (MD) simulation, solid-state NMR, and electrochemical impedance spectroscopy (EIS) [198]. For quaternary sulfide systems, Kanno et al. reported a Li$_{9.54}$Si$_{1.74}$P$_{1.44}$S$_{11.7}$Cl$_{0.3}$ ion conductor, displaying 3D conduction pathways (1D along the c axis and 2D in the ab plane) [185]. Beyond the improved ionic conductivity, the substituting and doping strategies for sulfide ASSEs also bring about higher air stability [199–201]. In addition, the chemical instability is another

important issue of sulfide-type ASSEs [202,203], which could be improved by oxygen doping constructing [204,205] or core-shell structure [206]. Moreover, the carbon additives in electrodes could cause the decomposition of sulfide-type ASSE at the electrode/electrolyte interface [207–209].

The mechanisms of Li$^+$ transport in inorganic crystal framework have been already put forward, including interstitial diffusion, direct exchange and ring diffusion, vacancy diffusion mechanism as well [210, 211]. However, more in-depth understandings of the ionic-transport behavior in sulfide-type ASSEs are still needed. Ceder et al. applied a structure matching algorithm to map the sulfur positions to the three most common crystal lattices: body-centered cubic (bcc), face-centered cubic (fcc, existed in Li$_2$S) and hexagonal close-packed (hcp, existed in Li$_4$GeS$_4$, γ-Li$_3$PS$_4$, LGPS, and other thio-LISICONs) lattices [212]. Then, they further calculated the Li$^+$-migration barrier within the bcc, fcc and hcp S^{2-} anion lattices (Fig. 10(a-c)) [212]. In the bcc S^{2-} lattice (Fig. 10 (a)), Li-ion migrates with the lowest barrier of only 0.15 eV, along a path connecting two face-sharing tetrahedral sites (T1 and T2), denoted as T-T path. In the fcc S^{2-} lattice (Fig. 10(b)), the migration of Li-ion passes by T1, O1(intermediate octahedral site) and T2 (0.40 eV), subsequently, denoted as T-O-T path [212]. In the hcp S^{2-} lattice (Fig. 10(c)), both T-O-T and T-T (T1 to T3, 0.20 eV) paths are discovered, where Li$^+$ conduction preferably goes through an alternation of T-T and T-O-T hopping [212]. The probability density of Li-ions obtained from AIMD simulations for several sulfide-type ASSEs was employed to further confirm the diffusion mechanisms of Li-ion in bcc, fcc and hcp sulfur lattices [212]. As shown in Fig. 10(d), the distribution of Li-ions in Li$_{10}$GeP$_2$S$_{12}$ occurs predominantly *via* the channels connecting tetrahedrally-coordinated Li sites along the c axis, whereas a 3D Li-ion diffusion network is found in Li$_7$P$_3$S$_{11}$ [212]. On the contrary, Li-ions are almost exclusively found on the isolated tetrahedral sites in the fcc Li$_2$S, where the absence of a continuous diffusion network indicates that the Li-ions hop through these octahedral sites at a very low frequency [212]. In Li$_4$GeS$_4$, the probability densities of Li-ions are localized in pairs of face-sharing tetrahedral sites, corresponding to T-T hopping [212]. In general, the bcc sublattice possesses the lowest activation barrier and highest ionic conductivity, and the sulfur sublattices of both Li$_{10}$GeP$_2$S$_{12}$ and Li$_7$P$_3$S$_{11}$ closely match with a bcc lattice [212].

In 2004, Machida et al. firstly applied a sulfide-type ASSE of 60Li$_2$S·40SiS$_2$ in Li$_{4.4}$Ge$_x$Si$_{1-x}$-based battery, which possessed the ion conductivity of 1.8×10^{-4} S cm^{-1} at room temperature [140]. For Si-based ASSBs with sulfide-type ASSEs, the Si-based anodes are always fabricated as cold-pressing Si pellets and blade-casting sheet-type composite Si pieces, which are suitable for scale-up manufacturing due to the good matching with the current production process of LIBs when compared with thin-film batteries based on LiPON ASSEs [109]. The sheet-type Si composite anodes almost consist of Si particles, sulfide solid particles, conductive carbon and binder, through blade-casting the slurry on a current collector. Hence, by integrating the Si particles and sulfide particles as composite anodes, the new interface between Si anode/sulfide ASSE is more complicated for the 3D contact than the interfaces between Si anode/liquid electrolyte and Si anode/LiPON ASSE. And the incompatible 'solid-solid' contact between Si anode/sulfide ASSE would generate new issues.

In order to alleviate the issue of 'solid-solid' contact, there are tremendous strategies to construct a compact and intimate interface between Si anode and sulfide-type ASSEs. Jung et al. firstly prepared a conventional Si anode composed of μ-Si particles, a polymeric binder, and carbon additives (Super P), and then subsequently infiltrated the solution-processable Li$_6$PS$_5$Cl (dissolved in anhydrous ethyl alcohol). This strategy could not only avoid the side reactions between sulfide-type ASSEs and the high polarity solvent used for slurry preparation, but also enable an excellent contact and percolation between ASSEs and Si electrodes (Fig. 11(a)) [132]. As shown in Fig. 11(b), the pores in the Si electrode are filled well with Li$_6$PS$_5$Cl (LPSCl) electrolytes. Furthermore, the LPSCl-infiltrated Si electrodes show much higher reversible
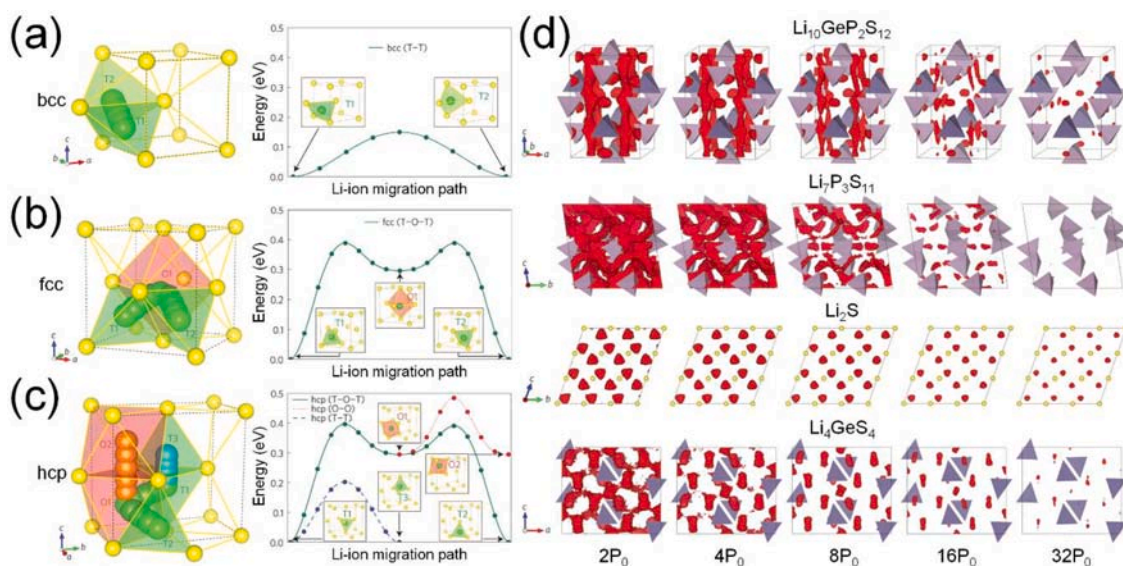
Fig. 10. Li-ion migration path (left panel) and the corresponding calculated migration energy (right panel) in bcc (a), fcc (b) and hcp (c) sulfur lattices [212]. The sulfur anions are colored yellow, and the Li ions are colored green, blue and red for different paths. LiS_4 tetrahedra and LiS_6 octahedra are colored green and red, respectively. (d) The probability densities of Li-ions are obtained from AIMD simulations at 900 K in $Li_{10}GeP_2S_{12}$, $Li_7P_3S_{11}$, Li_2S and Li_4GeS_4, respectively. Isosurfaces of the ionic probability densities are plotted at increasing isovalues ranging from $2P_0$ to $32P_0$, in which P_0 is defined as the mean value of the density for each structure. PS_4 tetrahedra and GeS_4 tetrahedra are colored purple and blue, respectively. The sulfur atoms are shown as small yellow circles for Li_2S [212]. (a-d) Reproduced with permission from ref. [212]. Copyright Nature Publishing Group, 2015.

capacities of over 3000 mAh g^{-1} at 30 °C and better rate performance than the conventional dry-mixed electrodes (Fig. 11(c)) [132]. Notably, the effect of stress on Si-based LIBs have been discussed above, where the high stress could retain a compact interface contact between anode and sulfide-type ASSE, thus ensuring a more stable long-term cycle performance of battery. The application of compress pressure could confine the volume expansion of Si particles, further ensuring a much more stable and long-term cycling performance with sacrificing a fraction of the overall capacity of Si-based ASSBs [101]. Low compression pressure of ASSBs causes a loose contact at the interface, resulting in serious capacity loss. Yamamoto et al. applied different compression presses on Si-based ASSBs based on Li_3PS_4 ASSEs, revealing that the compression pressure of 70 MPa could facilitate close contact at the interface *via* plastic deformation, and heal tiny cracks of Si anode during cycling [134]. The schematic illustration of the fabricated cell tightening by the cell holder is shown in Fig. 11(d) [134]. Fig. 11(e) (upper panel) illustrates that the voids and gaps at the interface between Si particles and ASSEs could be eliminated by the plastic deformation of sulfide-type ASSEs under external pressure during the long cycle [134]. And the cross-sectional SEM images of Si composite anodes (Fig. 11(e), bottom panel) demonstrate that a compressive pressure of 75 MPa applied in ASSBs heals the tiny cracks through the plastic deformation of ASSE compared with that of 50 MPa [134]. It could be found that higher pressure would improve the cell performance due to the maintenance of the ionic/electronic conductive pathways *via* particle contact, which exhibited a higher capacity retention of 64% (450 cycles) and a higher capacity than that of 50 MPa (Fig. 11(f)) [134].

It is well-known that electrodes are always mixed with ASSEs to construct a well-percolated ion conduction, which could fully utilize the capability of active material for minimizing the ionic resistance inside the electrodes [213–216]. And the interface with higher specific surface area between Si particles and ASSE generates a faster kinetic reaction, thus leading a better rate performance of batteries. Zhu's group prepared a Si composite anode (Si powder, Li_6PS_5Cl, and carbon black) through a simple ball-milling method, exhibiting an excellent rate performance than Li-metal anode [16]. The structure of full cell is illustrated in Fig. 12(a), where both Si anode and NCM811 cathode are well-composite with ASSEs, providing intimate ionic contact and

favorable ionic percolation [16]. Furthermore, they used a thin ASSE layer (50 μm) to assemble the Si-Li_6PS_5Cl||Li_6PS_5Cl||NCM811 full-cell with electrodes containing high mass loading of active material [16]. Notably, cell I (cathodic mass loading of 10 mg cm^{-2}) and cell II (cathodic mass loading of 20 mg cm^{-2}) exhibit good rate performance, among which cell I delivers average capacities of 184, 178, 163, 144, and 130 mAh g^{-1} at C/20, C/10, C/5, C/2, and 1 C, respectively, much higher than that with In-Li anode (Fig. 12(b)) [16]. And full-cells also demonstrate an excellent cycle performance and a high energy density, delivering a high capacity of 145 mAh g^{-1} at C/3 (1000 cycles, cell I) and a cell-level energy density of 285 Wh kg^{-1} (cell II) (Fig. 12(c)) [16]. Although the carbon additives would facilitate the decomposition of sulfide-type ASSE at the first cycle, the decomposition product is ionically conductive and stable in the following cycles, demonstrated by *operando* synchrotron X-ray absorption near-edge structure (XANES) [114]. Ci et al. designed a core-shell structure anode of $Li_7P_3S_{11}$(L-PS)-encapsulated nano-silicon (Si@LPS), which provided an intimate interfacial contact between Si particles and LPS ASSEs, promoting Li-ions diffusion during cycling due to the high room-temperature ionic conductivity of LPS ASSEs (Fig. 12(d)) [138]. And the high-resolution transmission electron microscope (HRTEM) images and EDS mappings prove that LPS ASSEs are homogeneously distributed throughout every particle and the LPS-coating thickness is about 5–10 nm (Fig. 12(e)) [138]. Compared with the bare Si anode (Fig. 12(f), left panel), the Si@LPS composite anode (Fig. 12(f), right panel) shows higher capacity and much better cycling stability (904.8 mAh g^{-1} with a capacity retention of 86.2% after 35 cycles at 50 mA g^{-1}) [138]. And the half-cell with Si@LPS anode also exhibits better electrochemical performances even at a higher current density (100 mA g^{-1}) with the specific capacity of 645.8 mAh g^{-1} after 35 cycles (Fig. 12(g)) [138].

In addition, the conductive carbon and binder in electrodes would bring about some issues, such as the decomposition of sulfide ASSEs and heterogeneity of Si composite anodes [208,217–219]. Hence, the strategies of binder-free and carbon-free have been put forward to address the issues above [22,124,218–220]. In 2018, Yamamoto et al. fabricated a binder-free sheet-type battery through heat treatment to remove the volatile binder of poly(propylene carbonate) (PPC) [218]. And the binder-free strategy brings benefits for the batteries, including enhanced
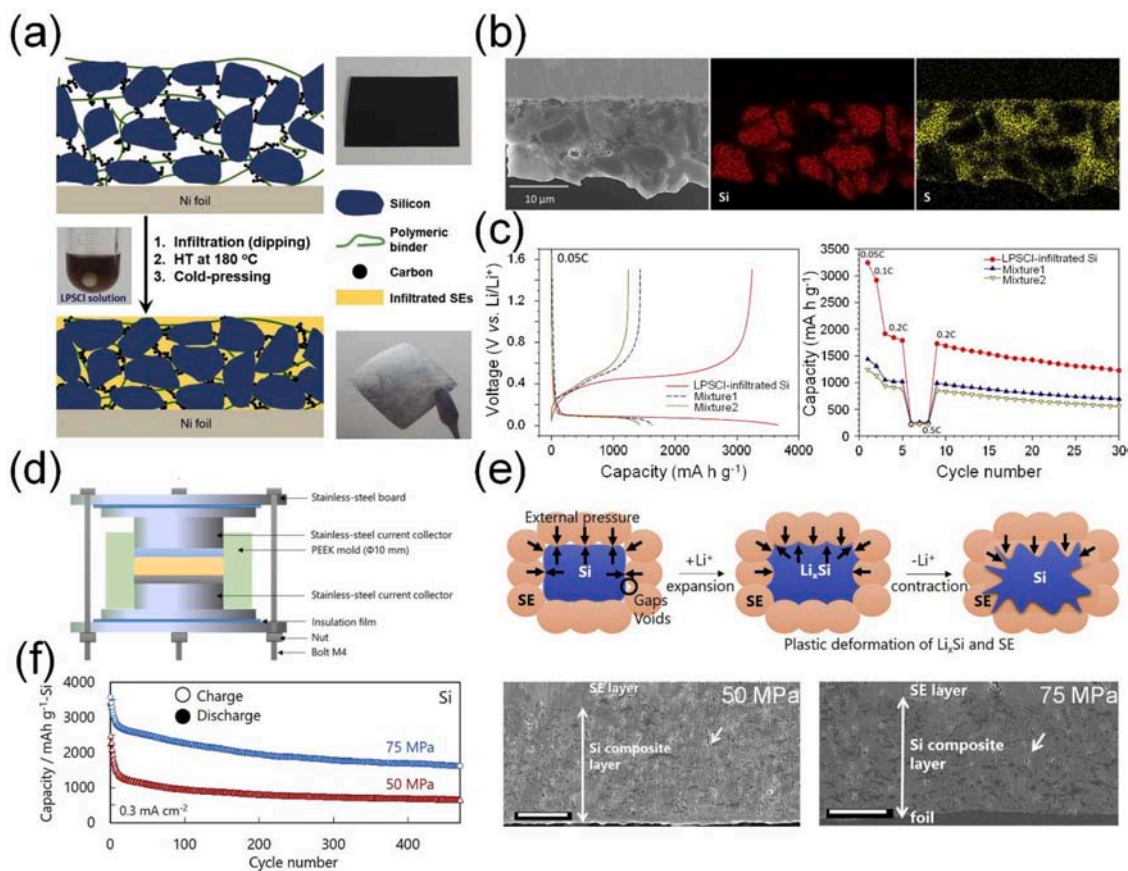
Fig. 11. (a) Schematic diagrams of Si electrodes before and after the infiltration of LPSCl ASSEs [132]. (b) Cross-sectional SEM images of the LPSCl-infiltrated Si electrode under different pressures and the corresponding EDS elemental mapping [132]. (c) Electrochemical performance of the all-solid-state Si/Li-In half-cell with the LPSCl-infiltrated Si anode, the conventional dry-mixed electrodes without and with polyvinylidene fluoride (PVDF) binder (referred to mixture1 and mixture2, respectively), which were prepared by manual mixing in dry conditions [132]. (d) Schematic illustration of a fabricated cell tightening by the cell holder using bolts and nuts at three points [134]. (e) Schematic diagram of the interface evolution between Si particles and Li$_3$PS$_4$ electrolytes (upper panel), and cross-sectional SEM images of Si composite anodes under different pressures (bottom panel) [134]. (f) Cycling performances of Si/Li-In half-cell measured under CC─CV charge and CC discharge (0.128 mA cm^{-2}, 0.03–0.05 C) [134]. (a-c) Reproduced with permission from ref. [132]. Copyright Elsevier, 2019. (d-f) Reproduced with permission from ref. [134]. Copyright Elsevier, 2020.

rate capability, excellent cycle stability, and a 2.6-fold increase of energy density when compared with the conventional pellet-type cells [218]. Subsequently, they employed the binder-free strategy into Si-based ASSBs, which exhibited a high initial Coulombic efficiencies of 95% and long-term cycling stability (specific capacity above 1700 mAh g^{-1} after 375 cycles) [131]. In 2019, Ohta et al. prepared a particulate Si anode without binder and carbon additives by spray deposition, resulting a thin and uniform layer of Si nanoparticles on the current collector, making a dense and intact interface. And the cell delivered a specific discharge of 2655 mAh g^{-1} even at a high current density of 5.48 mA cm^{-2} [122]. In 2021, Meng et al. developed a slurry-based approach to prepare a Si anode consisting of 99.9 wt% μ-Si and 0.1 wt% PVDF binder [22]. The carbon-free μ-Si anodes without the penetration of electrolyte provided a 2D-plane interfacial contact with sulfide-type ASSE, which prevented the generation of new interfaces and eliminated the detrimental effect on the stability of sulfide-type ASSEs brought about by carbon additives [22]. They employed two Si composite anodes (with and without 20 wt% carbon additives), a commercial Li$_6$PS$_5$Cl electrolyte, and an NCM811 cathode to assemble the full cell for evaluating the impact of carbon on the μ-Si-based ASSB system [22]. As shown in Fig. 13(a), the voltage profiles of μ-Si‖LPSCl‖ NCM811 cells with and without carbon additives during the first lithiation process display different shapes, indicating different electrochemical reactions [22]. Specifically, the cell without carbon additives shows a typical voltage plateau around 3.5 V, whereas the cell with

carbon additives shows a lower initial plateau at 2.5 V before reaching the lithiation potential above 3.5 V, indicating a serious decomposition of sulfide-type ASSEs [22]. And the XRD spectra of the pristine Si-ASSE, lithiated Si-ASSE, and lithiated Si-ASSE-carbon composites, demonstrated severe electrolyte decompositions, since most of the diffraction signals of pristine ASSE were no longer present and the peaks of nanocrystalline Li$_2$S appeared in the lithiated Si-ASSE-carbon composites (Fig. 13(a)) [22]. Furthermore, the corresponding XPS spectra in Fig. 13 (b) also confirm the conclusion that the presence of carbon results in a greater extent of ASSE decomposition. Notably, a greater decrease in peak intensities of the PS$_4^{3-}$ thiophosphate unit and a larger increase in peak intensities of the Li$_2$S are observed from the electrode with carbon additives (Fig. 13(b)) [22]. Therefore, the full cells achieve a high areal capacity of 12 mAh cm^{-2}, a stable capacity retention of 80% after 500 cycles and an average Coulombic efficiency of >99.9% (Fig. 13(c)) [22]. Recently, Wu et al. synthesized and investigated pristine Si anode, LiSi (lithiatied Si) anode and hard-carbon-stabilized Li-Si (LiSH) anode, respectively, and compared their electrode kinetics and mechanical stability [20]. The pristine Si anode after cycling shows vertical cracks throughout the anode and cracks at the Si/ASSE interface, which aggravates the mechanical instability and sluggish electrode kinetics (Fig. 13(d), upper panel) [20]. The LiSi anode after cycling shows fewer and narrower vertical/interfacial cracks, but is easy to form lithium dendrite growth after Li plating process (Fig. 13(d), middle panel) [20]. In contrast, the LiSH anode after cycling shows a densely continuous
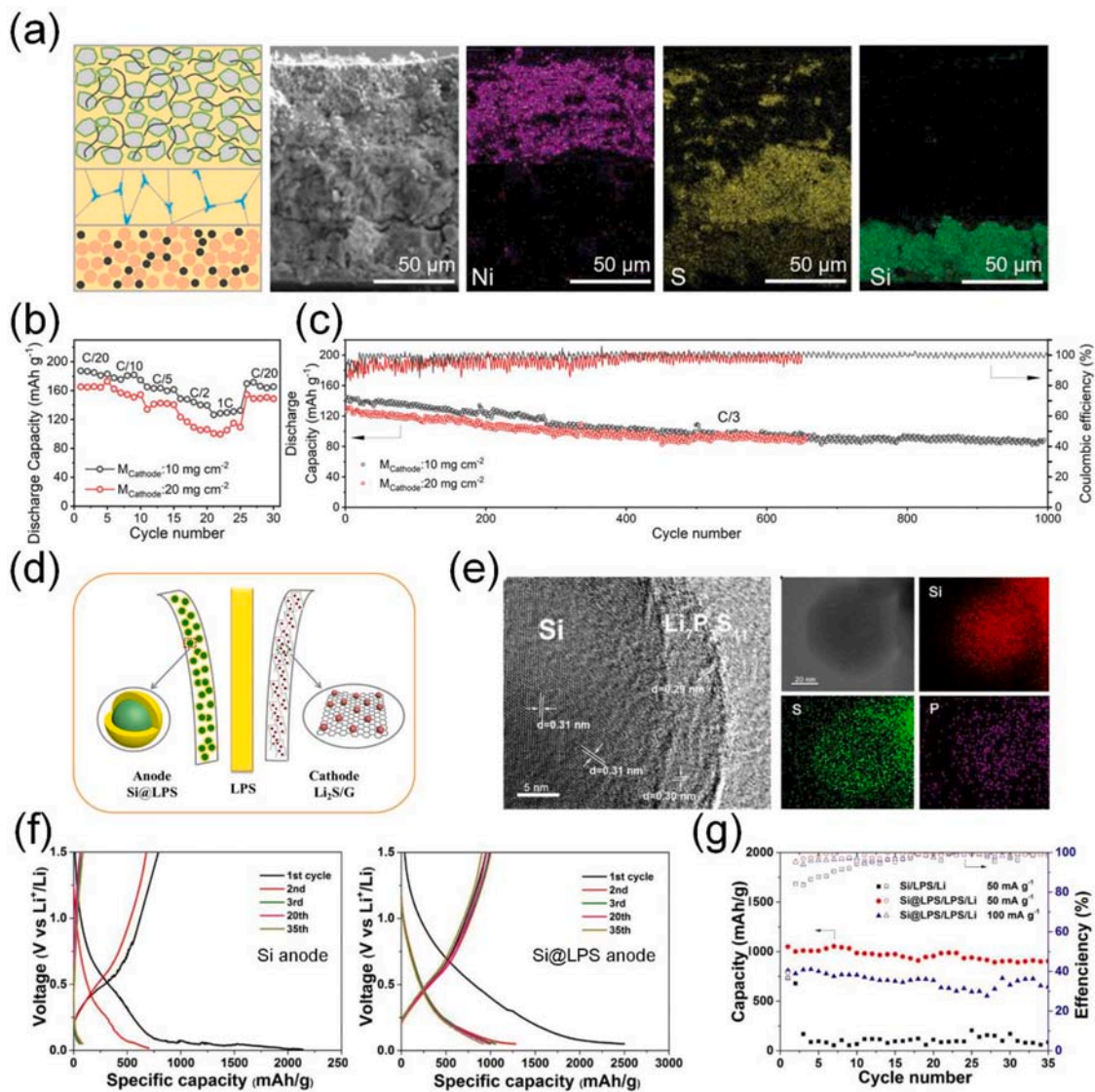
Fig. 12. (a) Schematic of the Si-ASSE||LPSCl||NCM811 full cell with ASSEs permeated into anode and cathode, and the corresponding EDS elemental mappings [16]. (b) Rate performance and (c) long-term cycling performance of the full cell with cathodic mass loadings of 10 and 20 mg cm^{-2}, respectively [16]. (d) Structure schematic of Si@LPS||LPS||Li$_2$S/Si full-cell [138]. (e) HRTEM, STEM images and EDS elemental mapping of Si@LPS [138]. (f) The charge/discharge voltage profiles of half-cells using bare Si anode (left panel) and Si@LPS anode (right panel) at 50 mA g^{-1} and room temperature [138]. (g) Cycling performance of half-cells using bare Si anode and Si@LPS anode at 50 mA g^{-1}, and Si@LPS at 100 mA g^{-1} and room temperature, respectively [138]. (a-c) Reproduced with permission from ref. [16]. Copyright WILEY-VCH, 2022. (d-g) Reproduced with permission from ref. [138]. Copyright Nature Publishing Group, 2020.

morphology with fast lithium diffusion, since plastically deformable Li-rich phases (Li$_{15}$Si$_4$ and LiC$_6$) could enlarge active area to suppress lithium dendrite growth and relieve stress concentration, leading to improved electrode kinetics and mechanical stability (Fig. 13(d), bottom panel) [20]. And the morphology evolutions of pristine Si, LiSi and LiSH anodes during cycling are investigated by SEM (Fig. 13(e)), which agree with the above conclusions as well [20]. Therefore, the Si-based anode with different weight ratios of Li, Si and HC (hard carbon) shows different electrochemical performance (Fig. 13(f)) [20]. The ASSB of LiHC anode without Si delivers a relatively low capacity, and the ASSB of LiSi anode without hard carbon quickly experiences a soft short circuit (Fig. 13(f)) [20]. Notably, the ASSBs with different LiSH anodes deliver stable cycle performances and high reversible capacities, among which LiSH46 anode exhibits the best cycle performance with little capacity decay even after 100 cycles for its improved lithium diffusion behavior, moderate thickness/porosity and superior mechanical stability (Fig. 13(f)) [20]. As a result, the LiCoO$_2$||Li$_6$PS$_5$Cl||LiSH46 ASSB demonstrates an ultrahigh capacity retention of 72.1% after 30,000

cycles at a current density of 20 C (14.64 mA cm^{-2}) and 55 °C (Fig. 13 (g)) [20].

3.3. Polymer-type and garnet-type ASSEs

Solid polymer electrolytes (SPEs) possess excellent flexibility among all-types ASSEs, which are beneficial to accommodate the volume variation of Si anode [174]. Moreover, SPEs also have many obvious advantages such as good interface compatibility, high chemical stability, excellent electronic resistance, light-weight, good ductility, and high processibility [9,221–224]. However, the low room-temperature ionic conductivities of $< 10^{-5}$ S cm^{-1} of polymer-type ASSEs severely hinder their practice applications [11]. Hence, many researches focus on the improvement of ionic conductivity at ambient temperature, such as the addition of plasticizers or fillers, and incorporating fast ionic conductors (inorganic ASSEs) [11,225,226]. The SPEs are divided into three types, including dry solid polymer electrolytes, gel/plasticized polymer electrolyte and composite polymer electrolytes, whereas gel/plasticized
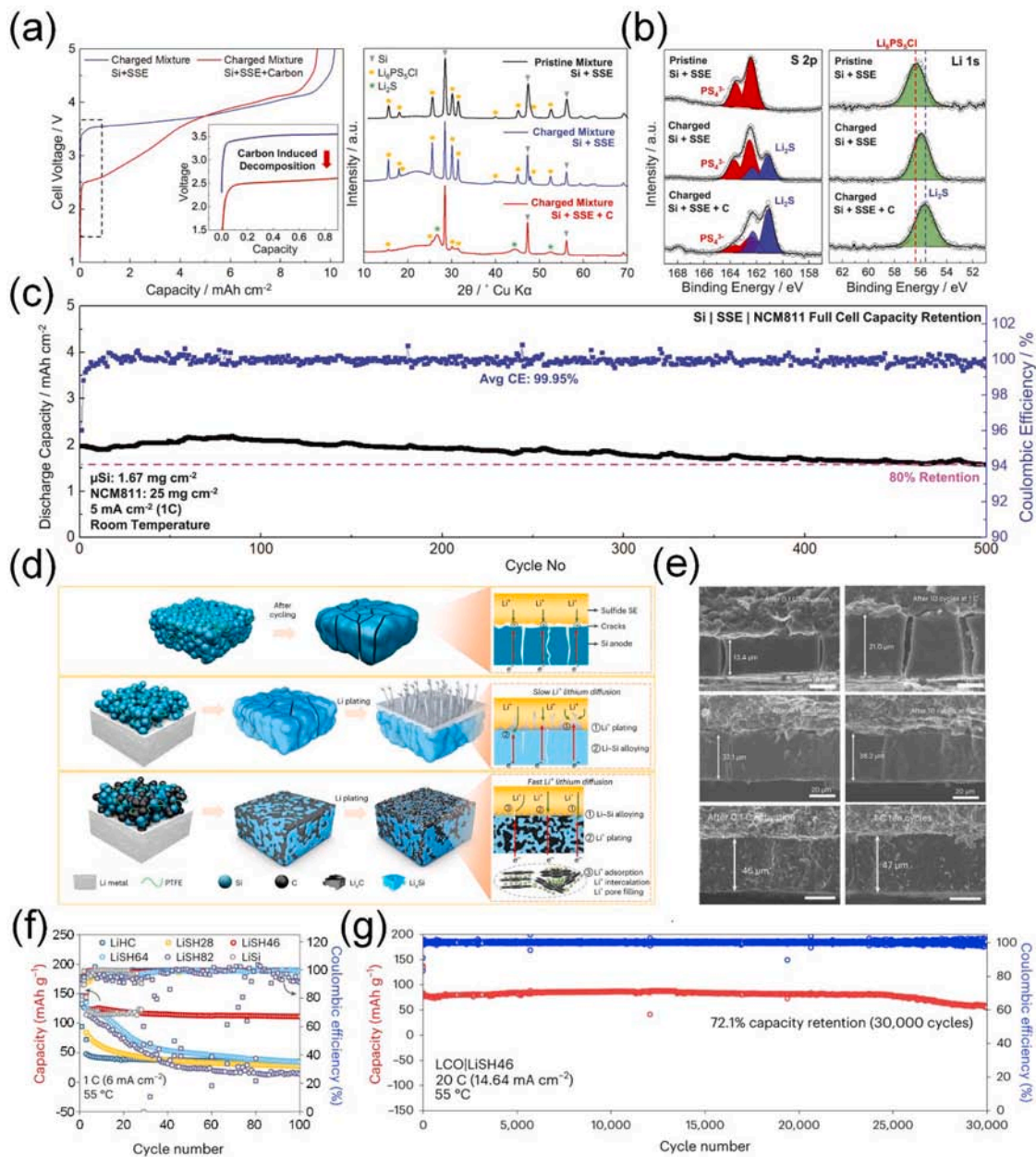
Fig. 13. (a) Voltage profiles of the μ-Si‖LPSCl‖NCM811 cells with and without carbon additives (left panel) and XRD patterns of the pristine Si-SSE, lithiated Si-SSE, and lithiated Si-SSE-carbon composites (right panel) [22]. (b) S 2*p* and Li 1 s XPS spectra of the pristine Si-ASSE, lithiated Si-ASSE, and lithiated Si-ASSE-carbon composites [22]. (c) Cycle performance of μ-Si‖LPSCl‖NCM811 cell at room temperature [22]. (d) Schematic illustration of mechanisms for pristine Si (upper panel), Li-Si (middle panel) and hard-carbon-stabilized Li-Si anodes (bottom panel) in ASSBs [20]. (e) Cross-section SEM images of Si (upper panel), Li-Si (middle panel) and hard-carbon-stabilized Li-Si anodes (bottom panel) at initial state after activation at 0.1 C for 2 cycles (left panel) and after 10 cycles at 1 C (right panel) [20]. (f) Cycle performance of Si-based anodes with different ratios of Si and HC at 1 C and 55 °C. LiSi, LiSH82, LiSH64, LiSH46, LiSH28, and LiHC mean different weight ratios of Li, Si and HC (41:56:0, 32:51:13, 30:40:27, 23:29:44, 16:16:64, 8:0:87, respectively) [20]. (g) The charge/discharge capacity and Coulombic efficiency as a function of cycle number at 20 C (14.64 mA cm^{-2}) and 55 °C for LCoO$_2$‖Li$_6$PS$_5$Cl‖LiSH46 ASSB [20]. (a-c) Reproduced with permission from ref. [22]. Copyright The American Association for the Advancement of Science, 2021. (d-g) Reproduced with permission from ref. [20]. Copyright Nature Publishing Group, 2023.

polymer electrolytes always contain liquid solvent, thus most of them cannot be defined as solvent-free ASSEs [9,227]. Among dry solid polymer electrolytes and composite polymer electrolytes, poly(ethylene oxide) (PEO) electrolytes have been mostly studied in ASSBs [228,229]. In 1978, Armand et al. proposed a PEO-Li SPE, whose ionic conductivity could achieve ~10^{-4} S cm^{-1} at high temperature of 40–60 °C [7]. In order to ensure the high ionic conductivity for SPE, PEO-based ASSBs are always operated at high temperature (60 °C) [230,231]. Zhao et al. prepared a PVDF fiber-supported PEO/garnet composite electrolyte (PPG), possessing an ionic conductivity of 8.1 × 10^{-5} S cm^{-1} at room

temperature and a thin thickness of 60 μm [143]. As shown in Fig. 14(a), a metal-organic framework hosted Si (Si@MOF) is used as an anode, and the micro-sized MOF-derived carbon hosts could provide sufficient conductive pathways and effectively buffer the repeated volume variation during cycling [143]. The Si@MOF‖PPG‖Li half-cell retained a high reversible capacity of 1442 mAh g^{-1} after 50 cycles (Fig. 14(b)) [143]. And the rate performance of Si@MOF symmetric cells is also investigated (Fig. 14(c-d)), which exhibited a long-term stable cycle performance of 1200 h at 0.2 mA cm^{-2} [143]. The full cell using LiFePO$_4$ (LFP) cathode could deliver a capacity of 135 mAh g^{-1} initially and
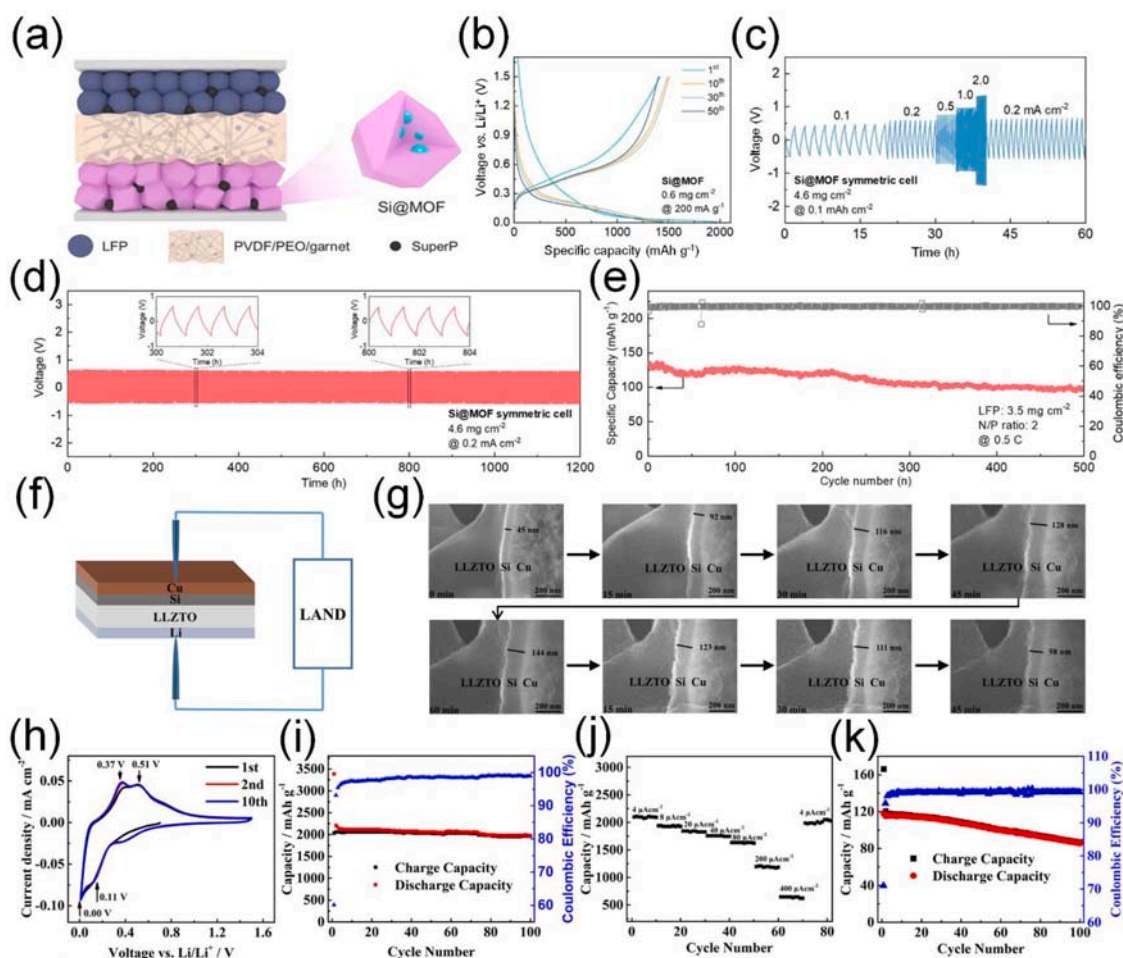
Fig. 14. (a) Schematic diagram of Si@MOF||PVDF/PEO/garnet||LFP ASSB [143]. (b) Voltage profiles of Si@MOF||PVDF/PEO/garnet||Li half-cell at 200 mA g^{-1} [143]. Voltage profiles of Si@MOF symmetric cell cycling at (c) different current densities, and (d) 0.2 mA cm^{-2} [143]. (e) Long-cycling of Si@MOF|| PVDF/PEO/garnet||LFP full cell at 0.5 C. All cells above are tested at 60 °C [143]. *In situ* SEM investigation during the polarization of the Si||LLZTO||Li cell with the 45-nm Si layer (f-g) [108]. (f) Schematic diagram of the Li||LLZTO||Si cell, and (g) SEM images during the lithiation/delithiation process. Electrochemical performance of Li||LLZTO||Si half-cell and Si||LLZTO||LFP full-cell (h-k) [108]. (h) Cyclic voltammogram curves at the 1st, 2nd, and 10th cycles measured at a scan rate of 0.1 mV s^{-1} within the potential ranging from 0.01 to 1.5 V *vs.* Li^{+}/Li. (i) Cycling performance of half-cell at 4 μA cm^{-2}. (j) Rate performance of half-cell at 4, 8, 20, 40, 80, 200, 400, and 4 μA cm^{-2}, respectively. (k) Cycling performance of full-cell at 8 μA cm^{-2}. The cells were tested at room temperature. (a-e) Reproduced with permission from ref. [143]. Copyright American Chemical Society, 2022. (f-k) Reproduced with permission from ref. [108]. Copyright American Chemical Society, 2018.

maintain a capacity retention of 73.1% after 500 cycles at 0.5 C (Fig. 14 (e)) [143]. Han et al. prepared a PEO-based composite ASSE by complexing PEO, lithium bis(trifluoromethane sulfonimide) (LiTFSI) and NASICON-type Li$_{1.3}$Al$_{0.3}$Ti$_{1.7}$(PO$_4$)$_3$, possessing the ionic conductivities of 5.3 × 10^{-5} S cm^{-1} at 50 °C and 2.86 × 10^{-5} S cm^{-1} at room temperature, respectively [88].

Garnet-type materials have the general formula A$_3$B$_2$Si$_3$O$_{12}$, in which the A and B cations have eight-fold and six-fold coordination, respectively [9]. Garnet-type ceramic ASSEs generally have a high room-temperature ionic conductivity of > 10^{-4} S cm^{-1} and high electrochemical/chemical stability, while the rigid nature of ceramic (Young's modulus = 149.8 GPa, shear modulus = 59.6 GPa, and bulk modulus = 102.8 GPa) would produce high interfacial impedance and poor mechanical properties with electrodes, thus hindering their large-scale manufacturing [10,232,233]. Hence, the poor contact between Si anode and garnet-type ASSE is a tough issue for Si-based ASSBs. Guo's group deposited the Si layer on a polished LLZTO ceramic pellet by direct current magnetron sputtering, and used the bulk Si (99.999%) as the target and pure Ar as the working gas [108]. The strategy of *in situ* deposition could solve the intrinsic contact issue between Si anode and garnet-type ASSEs, which is in accordance with that applied to

LiPON-based ASSBs. Figs. 14(f-g) show the *in situ* SEM images of Si layer during the lithiation/deliathiation process, and the Si/LLZTO interfaces are sustainable due to the thin-thickness of 45 nm Si layer [108]. Subsequently, the electrochemical performance of thin Si electrode are studied (Fig. 14(h-k)) [108]. The cyclic voltammogram curves show two reduction peaks at 0.11 and 0 V, corresponding to the initial lithiation of Si layer [108]. And two oxidation peaks at 0.37 and 0.51 V, corresponding to the transformation of amorphous Li$_x$Si to Si (Fig. 14(h)) [108]. And the curve shapes of the 2nd and 10th cycles are almost consistent, implying the high stability of the Si/LLZTO interface [108]. Figs. 14(i-j) demonstrate the excellent capacity retention and rate performance of Si||LLZTO||Li half-cell. The half-cell delivers a specific capacity of 1978 mAh g^{-1} and retains 97.3% after 100 cycles [108]. Guo's group also constructed a flexible interface between Si anode and a composite electrolyte consisting of PPCs and garnet-type ASSE, where the composite electrolytes showed a high ionic conductivity of 4.2 × 10^{-4} S cm^{-1} at room temperature [234]. Hu et al. prepared a garnet-type ASSE of LLZAO (Li$_7$La$_3$Zr$_2$O$_{12}$ with 3 wt% Al$_2$O$_3$) with a high ionic conductivity (4 × 10^{-4} S cm^{-1}), and subsequently deposited a 1-μm Si anode layer on the ASSE *via* plasma-enhanced chemical vapor deposition (PECVD) [142]. And the half-cell exhibited a high discharge

specific capacity of 2685 mAh g^{-1} and an excellent initial Coulombic efficiency of 83.2%, higher than that of the Si anodes with liquid electrolyte (77.1%), indicating the reduced irreversible reaction at the interfaces between Si anodes and ASSEs [142].

Overall, due to the ultra-high ionic conductivities at room temperature, sulfide-type ASSEs attract great interests from most researchers. Moreover, the good mechanical property provides a flexible interface between electrode and ASSE, and alleviates the volume expansion of Si particles. However, the poor air stability and narrow electrochemical window of sulfide-type ASSEs are unsatisfactory, which hinder their large-scale applications. Polymer-type ASSEs are flexible and stable, but they are extremely limited by the low ionic conductivity at room temperature. Garnet-type ASSEs possess high ionic conductivities at room temperature, whereas their mechanical properties and interfacial impedance with electrodes are undesirable. Although LiPON-type ASSEs have low ionic conductivity at room temperature, they are always deposited as thin-films, resulting in a low ionic conductive impedance of the whole electrolytes. However, limited by the current technology, LiPON-type ASSEs could be only applied to small-scale electronic products.

4. Structural design of Si-based anodes in ASSBs

The volume expansion of Si anode is the key issue for long-term cycling of battery, thus it is necessary to relieve or restrain the intrinsic problem on Si anode side, such as the strategy of effective structural design. There are two main structural designs on Si-based anode, including nano-structure (thin-films, nanoparticles, nanowires, nanotubes, nano-porous Si, *etc.*), and composite structure (compounding with carbon, metal, conductive polymer, binder, *etc.*) [123,235-251]. The strategies for addressing the issues of Si anodes have been greatly developed in Si-based liquid LIBs [32,39,40,252,253]. Obviously, these methods could effectively solve the issues of Si anode in ASSBs as well. Thus, this chapter focuses on the structural design of Si anode in ASSBs, including nano-structure and composite structure (Table 1).

Nanostructured Si anodes are advantageous for their ability to accommodate lithiation-induced strain, resulting in no or minor fracture during cycling and high rate performance [254]. For instance, thin-film Si anodes are generally applied into LiPON and garnet-based ASSBs to obtain a stable cycle performance [111,112,141]. As shown in Fig. 15 (a), Wang et al. deposited a 750-nm $LiMn_{1.5}Ni_{0.5}O_4$ (LMNO) cathode layer, a 1000-nm LiPON electrolyte layer and a 150-nm silicon anode layer step by step for full battery fabrication [111]. The XRD spectra demonstrate that the as-prepared Si anode deposited on the copper current collector is an amorphous thin-film, which possessed a more stable cycle performance than crystalline Si anode (Fig. 15(b)) [111]. And the Si||LiPON||LNMO full battery is cycled between 4.55 and 3 V under a rate of C/4 at 25 °C, which retains a capacity of ~37 µAh cm^{-2} after 40 cycles (Fig. 15(c)) [111]. Kanazawa et al. deposited a 60-nm Si anode layer onto the LiPON surface, exhibiting large unit area capacities of 32.8 and 15.7 µAh cm^{-2} at the first charge and discharge cycles [112]. Villevieille et al. deposited a 50-nm Si anode layer on LLZTO surface, and the Si||garnet||Li half-cell achieved an initial capacity of ~2700 mAh g^{-1} and stabilized a capacity above 1200 mAh g^{-1} for more than
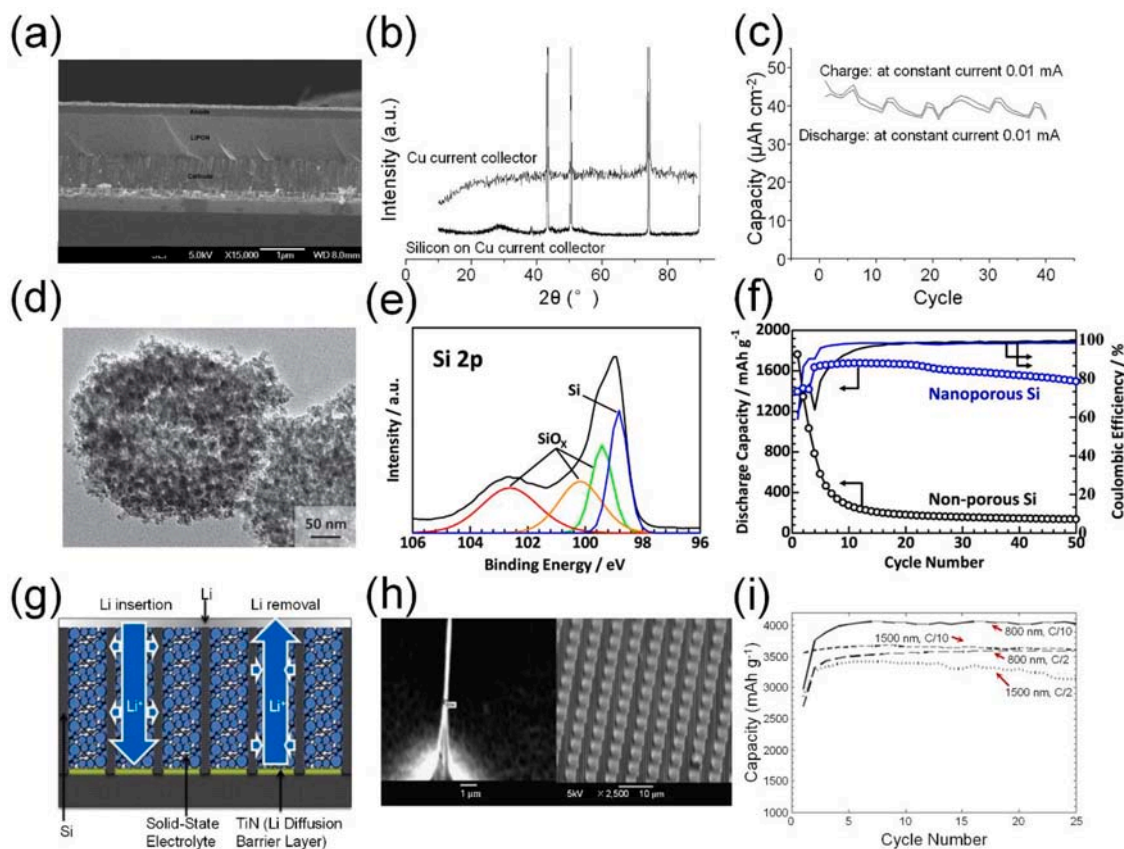

Fig. 15. (a) SEM cross-section image of the Si||LiPON||$LiNi_{1.5}Ni_{0.5}O_4$ full battery [111]. (b) X-ray diffractions of the thin Si layer deposited on copper (Cu) current collector and pristine Cu current collector [111]. (c) Cycle performance of Si||LiPON||$LiNi_{1.5}Ni_{0.5}O_4$ full cell [111]. (d) TEM images of nano-porous Si particles [129]. (e) Si $2p$ XPS spectra of nano-porous Si particles [129]. (f) Discharge capacity and CE of nano-porous and non-porous Li-In||Li_3PS_4||Si half-cells [129]. (g) Schematic of the cross-section view of a 3D integrated ASSB [107]. (h) SEM images of Si rods with the diameters of 300 and 750 nm, respectively [107]. (i) Capacity *vs.* cycle number for Si anodes with various rod diameter (800 and 1500 nm) and applied current density (C/2 and C/10) [107]. (a-c) Reproduced with permission from ref. [111]. Copyright Taylor & Francis, 2015. (d-f) Reproduced with permission from ref. [129]. Copyright The Electrochemical Society, 2022. (g-i) Reproduced with permission from ref. [107]. Copyright Elsevier, 2011.

100 cycles at 80 °C [141]. Guo et al. deposited thin Si layer with various thicknesses on LLZTO ASSEs and studied their electrochemical performance, demonstrating that the thinner Si anode possesses a more stable cycle performance than that of thick anode [108].

Okuno's group fabricated nano-porous Si particles by high-temperature reaction and acid-pickling step, and the particles were spherical in shape with a diameter of approximately 250–300 nm (Fig. 15(d)) [129]. Fig. 15(e) shows the XPS spectrum of Si 2p electrons, among which the peak at 98.8 eV is attributed to Si cores, and the peaks at 102.8 eV, 100.5 eV, and 99.5 eV are corresponding to silicon oxides [129]. The assembled Li-In||Li$_3$PS$_4$||nano-porous Si half-cell exhibits an excellent capacity retention of 89% after 50 cycles than that of non-porous Si anode (Fig. 15(f)) [129]. Furthermore, they used the mechanical-milling method to highly disperse the Si composite anodes, and the assembled half-cell achieved a high capacity retention of 80% up to 150 cycles [128]. Lee et al. used Si nanoparticles (50–100 nm) as anode materials in sulfide-based ASSBs, which exhibited a capacity retention of 66.9% after 40 cycles [124]. Additionally, the structures of Si nanotube were also studied in Si-based ASSBs [107,116]. In 2011, Lee et al. investigated the fabrication of structured Si rod electrodes to assemble the 3D integrated ASSBs with 77.5Li$_2$S-22.5P$_2$S$_5$ ASSEs (Fig. 15(g)) [107]. And the diameter of Si rods is fabricated within the range of 300–8000 nm (Fig. 15(h)) [107]. The half-cell with 800-nm Si

rods anode shows better cycle life and higher capacity than that of 1500 nm Si rods anode (Fig. 15(i)) [107]. In 2020, Kaskel' group fabricated a compact columnar-Si anode (col-Si) by the PVD method, which could provide a 2D contact interface to ASSEs, thus weakening the side reaction at the interface for its low specific surface area [116]. Ultimately, the col-Si||Li$_6$PS$_5$Cl||LiNi$_{0.9}$Co$_{0.05}$Mn$_{0.05}$O$_2$ full-cell demonstrated a highly stable cycling performance for more than 100 cycles with a high CE of 99.7–99.9%, and an industrially relevant areal loading of 3.5 mAh cm^{-2} [116].

To improve the mechanical stability and electronic/ionic conductivity of Si anode, several composite structures in ASSBs have been put forward, such as Si-carbon, Si-ASSEs, Si-metal and so on [117,120,124, 255-259]. In 2009, Lee et al. employed a nano-Si anode with glass-ceramic Li$_2$S-P$_2$S$_5$ electrolytes into ASSBs, and the assembled half-cell showed a slow decrease of specific capacity from 1420 to 950 mAh g^{-1} when up to the 40th cycle [124]. Paik et al. fabricated a Si/CNF@LPSCl composite anode by embedding the Si-nanoparticles in the carbon nanofiber (CNF) and subsequently sheathing them with LPSCl, and the assembled ASSB achieved a high energy density and stable cyclability (Fig. 16(a-d)) [120]. As shown in Fig. 16(a), the CNF matrix not only improves the mechanical stability to prevent from the huge volume expansion of Si particles during cycling but also provides good electronic conductivity in the electrode [120]. Furthermore, with
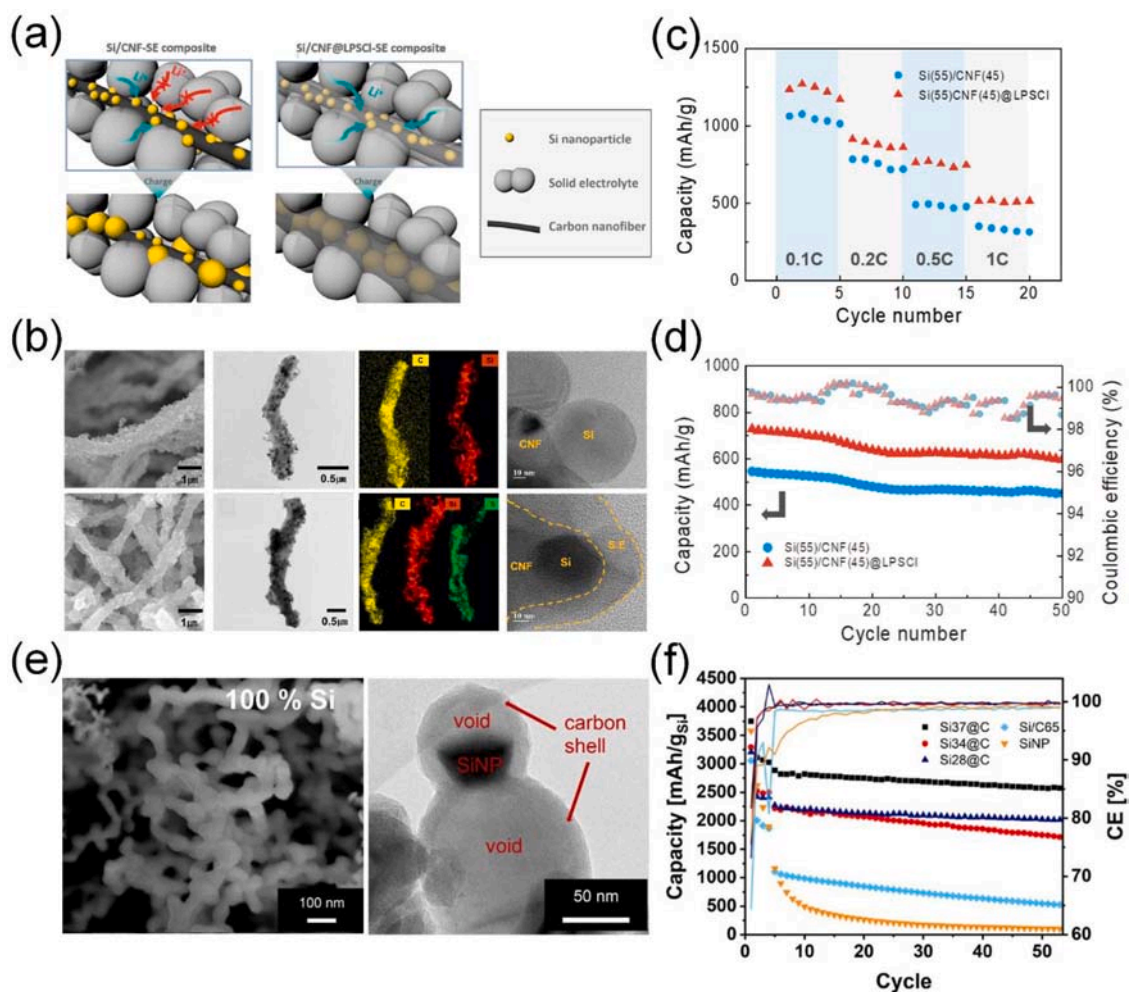

Fig. 16. (a) Schematic illustrating the lithiation processes of Si/CNF-SE (left panel) and Si/CNF@LPSCl (right panel) composite anodes, respectively [120]. (b) The images from left to right are SEM images, TEM images, EDS mappings and HR-TEM images of Si/CNF (upper panel) and Si/CNF@LPSCl composite (bottom panel) anodes, respectively [120]. (c) Rate capability of the Si/CNF and Si/CNF@LPSCl composite anodes, respectively [120]. (d) Cycle performance of Si/CNF and Si/CNF@LPSCl composite anodes at 0.5 C, respectively [120]. (e) SEM image of bare Si nanoparticles (left) and TEM image of silicon-carbon void structure (right) [117]. (f) Cycle performance of half-cells with Si-C composite and bare-Si anodes at 0.2 mA cm^{-2}, respectively [117]. (a-d) Reproduced with permission from ref. [120]. Copyright Elsevier, 2011. (e-f) Reproduced with permission from ref. [117]. Copyright Elsevier, 2021.

the addition of LPSCl-ASSE into Si/CNF composite anode, a more favorable strain could be released and robust electronic/ionic pathways are available. Fig. 16(b) shows SEM images, TEM images and corresponding EDS mappings of Si/CNF and Si/CNF@LPSCl composite anodes, respectively. Specially, Si nanoparticles with 60 nm diameter are embedded in the CNF fibers (~ 500 nm diameter) and 20 nm LPSCl layer is conformally coated on the surface of Si/CNF composite [120]. Compared with Si/CNF composite anode, Si/CNF@LPSCl composite anode possesses intimate contacts between the active material and ASSE due to the LPSCl coating [120]. Thus, the Si/CNF@LPSCl||LPSCl||Li-In half-cell exhibits a better rate performance and a more stable cycle capacity, delivering an initial capacity of 728 mAh g^{-1} and a stable cycle retention of 83.4% for 50 cycles at a current density of 0.5 C at 25 °C (Fig. 16(c-d)) [120]. Poetke et al. fabricated a silicon-carbon(C)-void structure of Si composite anode, among which the void structure could accommodate the volume expansion of Si anode during cycling (Fig. 16(e)) [117]. Therefore, the half-cell using Si-C composite anode shows more stable cycle performance compared with the bare Si anode (Fig. 16(f)) [117]. The Si@C||LiPSCl||Li half-cells with various Si contents in Si composite anode deliver different specific capacities, among which the Si37@C composite anode exhibits the highest lithiation capacity of >2570 mAh g^{-1} after 50 cycles for its appropriate volume ratio between Si core and C shell [117]. Lee et al. used polyacrylonitrile (PAN) as both a binder and a conductive additive for Si-nanoparticle anode, and the assembled half-cell attained large reversible capacities of ~1500 mAh g^{-1} at 1 C rate (>3 mA cm^{-2}) [125]. Navarra et al. prepared a Si composite anode within micro-Si, graphite, LiI-Li$_3$PS$_4$ ASSE, and CNF, which exhibited a capacity above 1200 mAh g^{-1} over 50 cycles [121]. Lee et al. also prepared a Si-C composite anode, among which the carbon came from the pyrolysis of coal-tar-pitch, delivering a stable specific capacity of 653.5 mAh g^{-1} after 100 cycles [127]. Huang's group put forward a "reinforced concrete" structure of Si composite anode within Si, carbon-nanotubes, and carbon, and the half-cell exhibited a reversible capacity of 1226 mAh g^{-1} after 50 cycles at 50 mA g^{-1} [119]. Kim's group reported a diffusion-dependent electrode that is comprised mostly of active materials without permeation of ASSEs, which could also deliver high energy density [23,118,260]. They thought that a seamless interface between each active material particles could form an efficient and continuous route for Li$^+$ transport in the electrode [23,261]. Therefore, they prepared a diffusion-dependent graphite-silicon electrode with short-range Li$^+$ diffusion paths for a rapid charge/discharge process. As a result, the content of Si in graphite-silicon composite anode could increase the capacity of battery, and the compliant graphite could accommodate the volume variation of Si particles and continuously provide abundant electrons transport for long-term cycling [23].

Although the structural-design strategies of Si anode play an effective role in the improvement of the electrochemical performance, there still exist some limitations. When the size of Si particles is reduced to nano-scale, the agglomeration effect is generally unavoidable between the particles, and the high specific surface area and surface energy would increase the reactivity of Si particles, which accelerate the capacity decay of batteries. Furthermore, the synthetic process of nanostructure is always complicated and inefficient, which goes against large-scale production. The same problem also occurs in the composite structure of Si anode. And the low Si content in Si composite anode results in low mass loading and further leads to the low energy density of Si-based ASSBs, which could be alleviated by increasing the tap/compaction density of Si anode [262]. Hence, in order to be commercially available, researches should not only focus on solving the key issues within Si-based ASSBs, but also further develop the modified strategies towards economic and technological feasibilities.

5. Construction and application of Si-based all-solid-state full batteries

Due to the good compatibility between Si anodes and ASSEs, the assembled half-cells have exhibited excellent electrochemical performances. However, the half-cells using Li or Li-In as counter electrodes deliver a relatively low voltage, which couldn't meet the high-voltage requirement of current electronic products. Hence, it is necessary to match Si anode with a high-voltage cathode and assemble them into the all-solid-state full batteries for further practical commercializing. This chapter reviews researches of Si-based all-solid-state full batteries and searches for their potential high-energy-density systems (Table 2).

In 2003, Lee et al. deposited a 170-nm LiCoO$_2$ layer as a positive electrode through RF magnetron sputtering, and the Si$_{0.7}$V$_{0.3}$||LiSiPON|| LiCoO$_2$ full-cell could cycle stably when operated between 2.0 and 3.9 V [113]. In 2004, Machida' group prepared a cathode composed of crystalline LiCo$_{0.3}$Ni$_{0.7}$O$_2$ (59 wt%), ASSE (39 wt%) and acetylene black (2 wt%) powders, and the assembled full cell could deliver a specific capacity of 190 mAh g^{-1} with a cutoff voltage from 4.1 to 2.3 V [140]. The previous researches demonstrated the availability of Si-based all-solid-state full batteries. In 2018, Guo et al. used LFP with carbon-coating as a cathode to construct a Si||LLZTO||LFP@C full battery, which exhibited a reversible capacity of 120 mAh g^{-1} and a capacity retention of 72% after 100 cycles [108]. Zhao et al. used the LFP material as a cathode, PEO/LLZTO ASSE as an electrolyte and Si@MOF material as an anode, and the assembled Si@MOF||PEO/LLZTO||LFP pouch cell could stably cycle for 50 cycles under 0.2 C at 60 °C [143]. To achieve a higher energy density of batteries, layered transition metal oxides of cathodes with high Ni-content have been developed (*e.g.*, LiNi$_{0.8}$Co$_{0.1}$Mn$_{0.1}$O$_2$ or LiNi$_{0.9}$Co$_{0.05}$Mn$_{0.05}$O$_2$, denoted as NCM), which possess high specific energy capacity (200–250 mAh g^{-1}) and relatively high operating voltage (~4.3 V *vs.* Li$^+$/Li) [263]. However, these cathodes are instable at high-voltage, which could also cause the oxidative decomposition of ASSEs [263]. Hence, the strategies of surface coating are widely used in high-voltage cathodes to improve their electrochemical stability [264]. In 2022, Zhu et al. used wet-chemical methods to fabricate the Li$_2$SiO$_x$ coating on NCM811, which could stabilize the interface between the cathode and the ASSE [16]. Furthermore, the full cell composed of nano-Si composite anode, thin ASSE, and the Li$_2$SiO$_x$@S-NCM cathode, could achieve a cell-level energy density of 285 Wh kg^{-1} with a high cathode mass loading of 20 mg cm^{-2} [16]. And they also employed the similar strategy to construct bipolar stacked ASSBs, which delivered a high voltage of 8.2 V and a cell-level energy density of 204 Wh kg^{-1}, higher than the 189 Wh kg^{-1} of mono cell [110]. Poetke's group prepared a LiNi$_{0.9}$Co$_{0.05}$Mn$_{0.05}$O$_2$ cathode with Li$_2$O-ZrO$_2$ coating by sol-gel method, and the full cell with a negative/positive (N/P) ratio of 1.1 led to ultra-high energy densities (375 Wh kg^{-1} and 1178 Wh L^{-1}) [117]. In addition, the boron-coating and LiNbO$_3$-coating are also investigated and employed in Si-based ASSBs [22,131,132].

Notably, the energy density of full battery is affected by many factors, such as the mass loading of active materials, N/P ratios, the types of ASSEs (such as light-weight SPE), the thickness of cathode, ASSE and anode, the applied stack pressure, and the weight (or volume) of all components (active materials, binders, carbon additives, ASSE, current collectors, packaging materials, *etc.*). Actually, thick-film ASSEs (*e.g.*, sulfide-type ASSE [265] and garnet-type ASSE [266]) decrease the battery's gravimetric/volumetric energy density and their rate performance. In order to study the relationship between the energy density of full batteries and thickness of ASSEs, Janek et al. calculated the specific energy density of Si||ASSE||NCM811 full batteries based on various ASSEs with different thicknesses [109]. They found that when the thickness of the LPSCl electrolyte was reduced from 100 to 30 μm, the specific energy density of Si||LPSCl||NCM811 cells would increase from 270.3 to 350.8 Wh kg^{-1}. And when the target of the energy density of Si||ASSE||NCM full-cells was set as 300 Wh kg^{-1}, the corresponding thickness of LLZO, LPSCl, and PEO ASSEs should be less than 23, 74, and

Table 2
Electrochemical performance of Si-based all-solid-state full batteries with various cathodes.

Si-based anode Type	All-solid-state electrolyte Type/thickness	Ionic conductivity/ Temperature	Cathode /Voltage range	Stack pressure	Current density/ Temperature	Cycling performance/ Capacity retention	Refs.
Nano Si @$Li_7P_3S_{11}$	$Li_6PS_5Cl < 50\ \mu m$	~2 mS cm^{-1} RT	Li_2SiO_x@S-NCM811 2.4–4.2 V	50 MPa	0.3 C RT 0.158 mA cm^{-2} RT	1st: 145 mAh g^{-1} 1000th: 91 mAh g^{-1} (62.9%) 285 Wh kg^{-1}	[16]
Si_{37}@C	Li_6PS_5Cl ~ 750 μm	3 mS cm^{-1} RT	$LiNi_{0.9}Co_{0.05}Mn_{0.05}O_2$@LZO 1.5–4.25V	3.5 Nm	0.07 mA cm^{-2} RT 1.47 mA cm^{-2} RT	1st: 187 mAh g^{-1} 1st: 125 mAh g^{-1}	[117]
Nano Si@ Li_6PS_5Cl	Li_6PS_5Cl 47 μm	> 1 mS cm^{-1} RT	Li_2SiO_x@S-NCM 2.25–4.1V	50 MPa	0.1 C	1st: 145 mAh g^{-1} 1st: 189 Wh kg^{-1} (mono cell) 1st: 204 Wh kg^{-1} (bipolar stack)	[110]
Si@LPSCl	$Li_{5.4}PS_{4.4}Cl_{1.6}$	~8 × 10^{-3} S cm^{-1} RT	NCM@Li_2SiO_x-SE	150 MPa	Cycled at C/20, C/10, C/5, C/2, and 1 C, respectively, RT	1st: 134, 117, 98, 68, and 45 mAh g^{-1}, respectively	[114]
Li_xSi	Li_6PS_5Cl 475 μm	/	S	~50 MPa	1 C 60 °C 0.3 C 25 °C	1st: 1301 mAh g^{-1} 1st: 980 mAh g^{-1} 500th: 748 mAh g^{-1} (76.3%)	[115]
Columnar-Si	Li_6PS_5Cl ~750 μm	3 mS cm^{-1} RT	$LiNi_{0.9}Co_{0.05}Mn_{0.05}O_2$ 2.0–4.25 V	3.0 Nm	0.07 mA cm^{-2} 25 °C	1st: 210 mAh g^{-1}	[116]
$Li_7P_3S_{11}$ coated Si	$Li_7P_3S_{11}$	10^{-3} S cm^{-1} RT	Li_2S/graphene 1–3 V	/	50 mA g^{-1} RT	1st: 316.9 mAh g^{-1} 20th: 179.4 mAh g^{-1}	[138]
99.9 wt%μ-Si 27 μm	Li_6PS_5Cl 30 μm	> 1 mS cm^{-1} RT	NCM811@B	50 MPa	5 mA cm^{-2} (1 C) RT	1st: 2 mAh cm^{-2} 500th: 1.6 mAh cm^{-2} (80%)	[22]
u-Si@LPS	75Li_2S-25P_2S_5 ~ 50 μm	5 × 10^{-4} S cm^{-1} RT	NCM@$LiNbO_3$ 2.5–4.2 V	75 MPa	0.064 mA cm^{-2} 30 °C	1st: 132 mAh g^{-1} 1st: 212 Wh kg^{-1}	[131]
Si@Li_6PS_5Cl	Li_3PS_4	1.4 × 10^{-3} S cm^{-1} 30 °C	$LiCoO_2$@$LiNbO_3$ 2.8–4.2 V	140 and 20 MPa	0.1 C (0.14 mA cm^{-2}) 30 °C	1st: 104 mAh g^{-1} 1st: 338 Wh kg^{-1}	[132]
$Li_{4.4}Ge_xSi_{1-x}$	60Li_2S-40SiS_2	1.8 × 10^{-4} S cm^{-1} RT	$LiCo_{0.3}Ni_{0.7}O_2$@SSE 2.3–4.1 V	/	64 μA cm^{-2}	1st: 190 mAh g^{-1}	[140]
μ-Si@LPS	Li_3PS_4 ~ 75 μm	5 × 10^{-4} S cm^{-1} RT	NCM@$LiNbO_3$-SE 2.5–4.2 V	75 MPa	0.15 (0.06–0.07 C)- 6 mA cm^{-2} (2.5–2.9 C)	1st: 146 mAh g^{-1} 38th: 98 mAh g^{-1} (67%)	[134]
10 wt%Si -graphite	Li_6PS_5Cl	/	$LiCoO_2$-Li_3InCl_6 3 ~ 4.2 V	60 MPa	0.5 C 25 °C	1st: 1.75 mAh cm^{-2}	[23]
Amorphous Si	LiPON 1.5 μm	/	VO-LiPO 0.5–3 V	/	0.3 μA RT	1st: 15.7 μAh cm^{-2}	[112]
thin Si layer, 180 nm	LLZTO 1 mm	/	LiFePO$_4$@C	/	8 μA cm^{-2} RT	1st: 120 mAh g^{-1} 100th: 86 mAh g^{-1} (72%)	[108]
$Si_{0.7}V_{0.3}$ 15 nm	$Li_{1.9}Si_{0.28}P_{1.0}O_{1.1}N_{1.0}$ 1.2 μm	8.8 × 10^{-6} S cm^{-1} RT	$LiCoO_2$ 2–3.9 V	/	RT	1500th: ~50 μAh cm^{-2}	[113]
Amorphous Si	LiPON 1 μm	2.2 × 10^{-6} S cm^{-1} RT	$LiMn_{1.5}Ni_{0.5}O_4$ 3.0–4.55V	/	0.01 mA 25 °C	1st: 47 μAh cm^{-2}	[111]
Nano Si@ Micro-MOF	PVDF/PEO/ $Li_{6.5}La_3Zr_{1.5}Ta_{0.5}O_{12}$ (LLZTO) 60 μm	8.1 × 10^{-5} S cm^{-1} 25 °C	LiFePO$_4$ 2.0–4.0 V	/	0.2 C 60 °C 0.5 C 60 °C	1st: 148 mAh g^{-1} 100th: 136 mAh g^{-1} (91.9%) 500th: 73.1%	[143]

92 μm, respectively. Therefore, decreasing the thickness of ASSEs is confirmed to be an effective method to further improve the energy density of full batteries. The garnet-type ASSEs are usually thick up to ~1 mm, meanwhile, the densities of garnet-type ASSEs are higher than other classes of ASSEs (sulfides and polymers), which greatly limit the overall gravimetric/volumetric energy density of battery [266]. However, processing a thin but robust garnet-type ASSEs is challenging for the brittle nature of ceramic [267]. Rupp et al. thought that the processing of thin-film garnet-type ASSE could start from wet-chemical scalable routes or low-temperature ceramic processing rather than conventional ceramic sintering, and requires alternative strategies to manufacture Li stoichiometries with a certain precision to ensure phase stability and high performance of the ASSE [267]. In addition, the external stack pressure applied for ASSBs also has an effect on the electrochemical performance, since the external stack pressure during the operation of ASSBs could maintain the ionic and electronic conduction network (Fig. 6(e-g)). Yamamoto et al. studied the effect of different external stack pressure on performance and microstructure of

Si-based all-solid-state full batteries [134]. And the Si||Li_3PS_4||NMC full cells under compressive pressures of 75 MPa showed higher initial discharge capacity and lower resistance than that of 50 MPa, and pressure facilitates plastic deformation of Li_xSi and ASSE, resulting in their improved contact [134].

Generally speaking, achieving a higher energy density (*e.g.*, > 300 Wh kg^{-1}) of Si-based all-solid-state full battery is still a challenge under the practical condition, since there are many sticky issues within the batteries, such as the low loading of active materials in the electrode (*e. g.*, Si-C composite anode), the undesirable interfacial impedance between electrode and ASSE, high difficulty in reducing the thickness of ASSEs, instability of high-voltage cathode, *etc.* Furthermore, the volume variation of Si anode also harms the cycle performance of batteries. Although there exist some challenges, great progresses have been made in Si-based ASSBs with outstanding electrochemical performance, which could provide guidance for constructing high-energy-density Si-based all-solid-state full battery. And the nano-structure of Si anode and decreasing the thickness of ASSEs are proven as effective methods for

improving the cycle stability and energy density of full batteries. In addition, Si-based ASSBs with thin-film electrolytes have been already applied in MEMS (Fig. 1(b)) in the past few decades. Hence, the large-scale Si-based ASSBs could probably be applied in 3C products, even EVs in the near future.

6. Conclusion and future perspectives

In this review, we describe in detail the electro-chemo-mechanical behavior of Si anode, including the lithiation mechanism, dynamic SEI reconstruction, evolution and effect of stress in Si-based LIBs, *etc.* Furthermore, failure mechanisms of Si-based liquid batteries are widely studied, whereas the relevant researches of ASSBs are still inadequate. Hence, to reveal the failure mechanism of Si-based ASSBs, further characterization techniques should be vigorously developed, such as *in situ* visualization tests on the dynamic evolution of Si anode and interface during long-term cycling processes. Subsequently, we also systematically summarize the development of different ASSEs and Si anodes in Si-based ASSBs in recent years. ASSEs used for Si-based ASSBs at present include LiPON-type, sulfide-type, garnet-type and polymer-type ASSEs, among which sulfide-type ASSEs are the most popular materials for ductile mechanical properties and high ionic conductivities at room temperature. However, the undesirable electrochemical window, poor stability in air or polar solvent, and unstable interface with electrodes of sulfide-type ASSEs limit their broad application. Thus, the available modified strategies for sulfide-type ASSEs are put forward to address the above issues, including doping and coating. Beyond the ASSEs, the structure of Si anode could be optimized to further improve the electrochemical performance of ASSBs. And many structural-design strategies in Si-based liquid batteries are guidable for ASSBs as well, *i.e.*, nano-structure and composite structure. However, these strategies are perhaps not suitable for constructing high-mass-loading anodes and applying them to large-scale production. In order to meet the demands of practical application, high-voltage cathodes are used by many researches to match Si-based anodes for constructing high-energy Si-based ASSBs. Benefiting from the numerous merits of Si-based ASSBs, they are the most promising candidates for next-generation energy storage systems.

Nevertheless, several challenges still hinder further practical applications of Si-based ASSBs. In this regard, we proposed some suggestions for the development of next-generation Si-based ASSBs.

a) Further fundamental understanding of failure mechanisms in Si-based ASSBs. The failure mechanisms of Si-based liquid batteries are scientifically investigated by many advanced characterizations, which could provide guidance for the optimization of Si-based anode in liquid batteries. However, the failure mechanisms in Si-based ASSBs are unsystematic for the insufficient relevant studies, which hinder the development of the optimal strategies for Si-based anode in ASSBs. Hence, the *in situ* visualization of Si anode and SEI analysis at the interface in ASSB should be further developed, such as cryo-EM, *in situ* X-ray computed tomography, *in situ* TEM, *in situ* XPS, *in situ* atomic force microscopy (AFM) and time-of-flight secondary ion mass spectrometry (TOF-SIMS) [60,87,95,268-270].

b) Further enhancing the room-temperature ionic conductivity and electrochemical/chemical stability of ASSEs. The ideal ASSEs should possess a wide electrochemical stability window, high ionic conductivity at room temperature, low electronic conductivity, good mechanical properties, high chemical stability, low cost, and simple processability. Unfortunately, the present ASSEs couldn't meet all the requirements. Thereinto, sulfide-type ASSEs possess ultra-high ionic conductivity and good ductility, yet have their limitations (*e. g.*, unstable electrochemical window and instability to moisture or polar solvent), which should be solved by coating or doping methods. Although polymer-type ASSEs have high stability and flexibility, they are limited by the high impedance of Li+ transfer at

room temperature. Accordingly, increasing the ionic conductivity of polymer-type ASSEs is a possible approach for the further application of Si-based ASSBs. More importantly, reducing the thickness of polymer-type ASSEs is another good strategy for their decreased bulk resistance on ionic conduction of whole electrolytes. Furthermore, reducing the thickness of ASSEs is effective for increasing the energy density of full batteries as well.

c) Promoting economic and technological feasibilities for large-scale applications. Although the nano-structure and composite structure of Si anodes are helpful to improve the electrochemical performance of batteries, the fabrication process is always complicated and inefficient, which is not applicable for practical productions. Hence, the synthetic technique of nano-structure and composite structure should be further developed towards low cost and high efficiency, such as μSi-graphite composite anode. In addition, the silicon oxide (SiO) materials derived from pure Si possess lower volume expansion and higher cycle performance than Si anode, which have realized commercial applications in liquid batteries [271]. Therefore, SiO could be an alternative material as anode for Si-based ASSBs [272].

In conclusion, Si-based ASSBs are the promising alternative for the next-generation energy storage system owing to their high energy density and reliable safety. Fortunately, even though there exist some challenges before the practical application of Si-based ASSBs, the relevant researches in liquid batteries are numerous, which are available for reference to Si-based ASSBs. Furthermore, advanced researches of Si-based ASSBs have shown their great potential for practical applications. Therefore, it is worthwhile to further investigate the failure mechanisms and advanced strategies to gain a deeper understanding and improve electrochemical performance of Si-based ASSBs. And we hope that this review provides in-depth understandings of failure mechanisms and advanced optimization strategies of Si-based ASSBs to guide their further development.

Data availability

No data was used for the research described in the article.

Declaration of Competing Interest

The authors declare that they have no known competing financial interests or personal relationships that could have appeared to influence the work reported in this paper.

Acknowledgements

References

[1] H. Zhang, C. Li, G.G. Eshetu, S. Laruelle, S. Grugeon, K. Zaghib, C. Julien, A. Mauger, D. Guyomard, T. Rojo, N. Gisbert-Trejo, S. Passerini, X. Huang, Z. Zhou, P. Johansson, M. Forsyth, From solid-solution electrodes and the

rocking-chair concept to today's batteries, Angew. Chem. Int. Ed. 59 (2020) 534–538.

[2] M. Armand, J.M. Tarascon, Building better batteries, Nature 451 (2008) 652–657.

[3] S. Chae, S.H. Choi, N. Kim, J. Sung, J. Cho, Integration of graphite and silicon anodes for the commercialization of high-energy lithium-ion batteries, Angew. Chem. Int. Ed. 59 (2020) 110–135.

[4] T. Krauskopf, F.H. Richter, W.G. Zeier, J. Janek, Physicochemical concepts of the lithium metal anode in solid-state batteries, Chem. Rev. 120 (2020) 7745–7794.

[5] X.B. Cheng, R. Zhang, C.Z. Zhao, Q. Zhang, Toward safe lithium metal anode in rechargeable batteries: A review, Chem. Rev. 117 (2017) 10403–10473.

[6] X. Feng, M. Ouyang, X. Liu, L. Lu, Y. Xia, X. He, Thermal runaway mechanism of lithium ion battery for electric vehicles: A review, Energy Storage Mater. 10 (2018) 246–267.

[7] M. Armand, M. Duclot, J. Chabagno, in: proceedings of the second international meeting on solid state electrolytes, St Andrews, Scotland, 1978.

[8] J.M. Tarascon, M. Armand, Issues and challenges facing rechargeable lithium batteries, Nature 414 (2001) 359–367.

[9] A. Manthiram, X. Yu, S. Wang, Lithium battery chemistries enabled by solid-state electrolytes, Nat. Rev. Mater. 2 (2017) 16103–16118.

[10] J.C. Bachman, S. Muy, A. Grimaud, H.H. Chang, N. Pour, S.F. Lux, O. Paschos, F. Maglia, S. Lupart, P. Lamp, L. Giordano, Y. Shao-Horn, Inorganic solid-state electrolytes for lithium batteries: Mechanisms and properties governing ion conduction, Chem. Rev. 116 (2016) 140–162.

[11] D. Zhou, D. Shanmukaraj, A. Tkacheva, M. Armand, G. Wang, Polymer electrolytes for lithium-based batteries: Advances and prospects, Chem 5 (2019) 2326–2352.

[12] Y. Huang, B. Shao, Y. Wang, F. Han, Solid-state silicon anode with extremely high initial coulombic efficiency, Energy Environ. Sci. (2023) 1569–1580.

[13] Z. Zhao, F. Chen, J. Han, D. Kong, S. Pan, J. Xiao, S. Wu, Q.H. Yang, Revival of microparticular silicon for superior lithium storage, Adv. Energy Mater. (2023), 2300367.

[14] J.B. Goodenough, Y. Kim, Challenges for rechargeable Li batteries, Chem. Mater. 22 (2009) 587–603.

[15] K. Yoon, S. Lee, K. Oh, K. Kang, Challenges and strategies towards practically feasible solid-state lithium metal batteries, Adv. Mater. 34 (2022), e2104666.

[16] D. Cao, X. Sun, Y. Li, A. Anderson, W. Lu, H. Zhu, Long-cycling sulfide-based all-solid-state batteries enabled by electrochemo-mechanically stable electrodes, Adv. Mater. 34 (2022), e2200401.

[17] L. Ji, Z. Lin, M. Alcoutlabi, X. Zhang, Recent developments in nanostructured anode materials for rechargeable lithium-ion batteries, Energy Environ. Sci. 4 (2011) 2682–2699.

[18] Y. Sun, N. Liu, Y. Cui, Promises and challenges of nanomaterials for lithium-based rechargeable batteries, Nat. Energy 1 (2016) 16071–16082.

[19] J. Janek, W.G. Zeier, Challenges in speeding up solid-state battery development, Nat. Energy 8 (2023) 230–240.

[20] W. Yan, Z. Mu, Z. Wang, Y. Huang, D. Wu, P. Lu, J. Lu, J. Xu, Y. Wu, T. Ma, M. Yang, X. Zhu, Y. Xia, S. Shi, L. Chen, H. Li, F. Wu, Hard-carbon-stabilized Li-Si anodes for high-performance all-solid-state Li-ion batteries, Nat. Energy (2023).

[21] J.A. Lewis, K.A. Cavallaro, Y. Liu, M.T. McDowell, The promise of alloy anodes for solid-state batteries, Joule 6 (2022) 1418–1430.

[22] D.H.S. Tan, Y.T. Chen, H. Yang, W. Bao, B. Sreenarayanan, J.M. Doux, W. Li, B. Lu, S.Y. Ham, B. Sayahpour, J. Scharf, E.A. Wu, G. Deysher, H.E. Han, H. J. Hah, H. Jeong, J.B. Lee, Z. Chen, Y.S. Meng, Carbon-free high-loading silicon anodes enabled by sulfide solid electrolytes, Science 373 (2021) 1494–1499.

[23] J.Y. Kim, S. Jung, S.H. Kang, J. Park, M.J. Lee, D. Jin, D.O. Shin, Y.G. Lee, Y. M. Lee, Graphite–silicon diffusion-dependent electrode with short effective diffusion length for high-performance all-solid-state batteries, Adv. Energy Mater. 12 (2021), 2103108.

[24] J. Wu, S. Liu, F. Han, X. Yao, C. Wang, Lithium/sulfide all-solid-state batteries using sulfide electrolytes, Adv. Mater. 33 (2021), e2000751.

[25] Y. Wang, T. Liu, J. Kumar, Effect of pressure on lithium metal deposition and stripping against sulfide-based solid electrolytes, ACS Appl. Mater. Interfaces 12 (2020) 34771–34776.

[26] J.M. Doux, H. Nguyen, D.H.S. Tan, A. Banerjee, X. Wang, E.A. Wu, C. Jo, H. Yang, Y.S. Meng, Stack pressure considerations for room-temperature all-solid-state lithium metal batteries, Adv. Energy Mater. 10 (2019) 1903253–1903258.

[27] M.A. Hopcroft, W.D. Nix, T.W. Kenny, What is the young's modulus of silicon? J. Microelectromech. Syst. 19 (2010) 229–238.

[28] J.W. Choi, D. Aurbach, Promise and reality of post-lithium-ion batteries with high energy densities, Nat. Rev. Mater. 1 (2016) 16013–16028.

[29] V.P. Phan, B. Pecquenard, F.Le Cras, High-performance all-solid-state cells fabricated with silicon electrodes, Adv. Funct. Mater. 22 (2012) 2580–2584.

[30] D. Ruzmetov, V.P. Oleshko, P.M. Haney, H.J. Lezec, K. Karki, K.H. Baloch, A. K. Agrawal, A.V. Davydov, S. Krylyuk, Y. Liu, J. Huang, M. Tanase, J. Cumings, A. A. Talin, Electrolyte stability determines scaling limits for solid-state 3D Li ion batteries, Nano Lett 12 (2012) 505–511.

[31] Y. Li, X. Cheng, Y. Zhang, K. Zhao, Recent advance in understanding the electro-chemo-mechanical behavior of lithium-ion batteries by electron microscopy, Mater. Today Nano 7 (2019) 100040–100057.

[32] M.T. McDowell, S.W. Lee, W.D. Nix, Y. Cui, 25th anniversary article: Understanding the lithiation of silicon and other alloying anodes for lithium-ion batteries, Adv. Mater. 25 (2013) 4966–4985.

[33] L.Y. Beaulieu, K.W. Eberman, R.L. Turner, L.J. Krause, J.R. Dahn, Colossal reversible volume changes in lithium alloys, Electrochem. Solid-State Lett. 4 (2001) A137–A140.

[34] C.M. Park, J.H. Kim, H. Kim, H.J. Sohn, Li-alloy based anode materials for Li secondary batteries, Chem. Soc. Rev. 39 (2010) 3115–3141.

[35] W.J. Zhang, A review of the electrochemical performance of alloy anodes for lithium-ion batteries, J. Power Sources 196 (2011) 13–24.

[36] H. Wu, Y. Cui, Designing nanostructured Si anodes for high energy lithium ion batteries, Nano Today 7 (2012) 414–429.

[37] G.K. Simon, T. Goswami, Improving anodes for lithium ion batteries, Metall. Mater. Trans. A 42 (2010) 231–238.

[38] G. Ji, Y. Ma, J.Y. Lee, Mitigating the initial capacity loss (ICL) problem in high-capacity lithium ion battery anode materials, J. Mater. Chem. 21 (2011) 9819–9824.

[39] C.K. Chan, H. Peng, G. Liu, K. McIlwrath, X.F. Zhang, R.A. Huggins, Y. Cui, High-performance lithium battery anodes using silicon nanowires, Nat. Nanotechnol. 3 (2008) 31–35.

[40] T. Song, J. Xia, J.H. Lee, D.H. Lee, M.S. Kwon, J.M. Choi, J. Wu, S.K. Doo, H. Chang, W.I. Park, D.S. Zang, H. Kim, Y. Huang, K.C. Hwang, J.A. Rogers, U. Paik, Arrays of sealed silicon nanotubes as anodes for lithium ion batteries, Nano Lett 10 (2010) 1710–1716.

[41] G. Bucci, T. Swamy, S. Bishop, B.W. Sheldon, Y.M. Chiang, W.C. Carter, The effect of stress on battery-electrode capacity, J. Electrochem. Soc. 164 (2017) A645–A654.

[42] X. Wang, Y. Chen, O.G. Schmidt, C. Yan, Engineered nanomembranes for smart energy storage devices, Chem. Soc. Rev. 45 (2016) 1308–1330.

[43] L. Liu, Q. Weng, X. Lu, X. Sun, L. Zhang, O.G. Schmidt, Advances on microsized on-chip lithium-ion batteries, Small 13 (2017) 1701847–1701858.

[44] F.L. Cras, B. Pecquenard, V. Dubois, V.P. Phan, D. Guy-Bouyssou, All-solid-state lithium-ion microbatteries using silicon nanofilm anodes: High performance and memory effect, Adv. Energy Mater. 5 (2015) 1501061–1501070.

[45] S. Pan, J. Han, Y. Wang, Z. Li, F. Chen, Y. Guo, Z. Han, K. Xiao, Z. Yu, M. Yu, S. Wu, D.W. Wang, Q.H. Yang, Integrating SEI into layered conductive polymer coatings for ultrastable silicon anodes, Adv. Mater. 34 (2022), e2203617.

[46] S.C. Lai, Solid lithium-silicon electrode, J. Electrochem. Soc. 123 (2019) 1196–1197.

[47] C.J. Wen, R.A. Huggins, Chemical diffusion in intermediate phases in the lithium-silicon system, J. Solid State Chem. 37 (1981) 271–278.

[48] Y. Zhao, P. Stein, Y. Bai, M. Al-Siraj, Y. Yang, B.X. Xu, A review on modeling of electro-chemo-mechanics in lithium-ion batteries, J. Power Sources 413 (2019) 259–283.

[49] H. Li, X.J. Huang, L.Q. Chen, Z.G. Wu, Y. Liang, A high capacity nano-Si composite anode material for lithium rechargeable batteries, Electrochem. Solid-State Lett. 2 (1999) 547–549.

[50] S.J. Lee, J.K. Lee, S.H. Chung, H.Y. Lee, S.M. Lee, H.K. Baik, Stress effect on cycle properties of the silicon thin-film anode, J. Power Sources 97-98 (2001) 191–193.

[51] P. Limthongkul, Y.I. Jang, N.J. Dudney, Y.M. Chiang, Electrochemically-driven solid-state amorphization in lithium-silicon alloys and implications for lithium storage, Acta Mater 51 (2003) 1103–1113.

[52] M.N. Obrovac, L. Christensen, Structural changes in silicon anodes during lithium insertion/extraction, Electrochem. Solid-State Lett. 7 (2004) A93–A96.

[53] A. Netz, Amorphous silicon formed *in situ* as negative electrode reactant in lithium cells, Solid State Ionics 175 (2004) 215–219.

[54] J. Li, J.R. Dahn, An *in situ* X-ray diffraction study of the reaction of Li with crystalline Si, J. Electrochem. Soc. 154 (2007) A156–A161.

[55] T.D. Hatchard, J.R. Dahn, *In situ* XRD and electrochemical study of the reaction of lithium with amorphous silicon, J. Electrochem. Soc. 151 (2004) A838–A842.

[56] J. Graetz, C.C. Ahn, R. Yazami, B. Fultz, Highly reversible lithium storage in nanostructured silicon, Electrochem. Solid-State Lett. 6 (2003) A194–A197.

[57] L.Y. Beaulieu, T.D. Hatchard, A. Bonakdarpour, M.D. Fleischauer, J.R. Dahn, Reaction of Li with alloy thin films studied by *in situ* AFM, J. Electrochem. Soc. 150 (2003) A1457–A1464.

[58] J. Lu, Z. Chen, F. Pan, Y. Cui, K. Amine, High-performance anode materials for rechargeable lithium-ion batteries, Electrochem. Energy Rev. 1 (2018) 35–53.

[59] P. Oh, J. Yun, J.H. Choi, K.S. Saqib, T.J. Embleton, S. Park, C. Lee, J. Ali, K. Ko, J. Cho, Development of high-energy anodes for all-solid-state lithium batteries based on sulfide electrolytes, Angew. Chem. Int. Ed. 61 (2022), e202201249.

[60] X.H. Liu, J.Y. Huang, *In situ* TEM electrochemistry of anode materials in lithium ion batteries, Energy Environ. Sci. 4 (2011) 3844–3860.

[61] X. Wang, F. Fan, J. Wang, H. Wang, S. Tao, A. Yang, Y. Liu, H. Beng Chew, S. X. Mao, T. Zhu, S. Xia, High damage tolerance of electrochemically lithiated silicon, Nat. Commun. 6 (2015) 8417–8423.

[62] X.H. Liu, L.Q. Zhang, L. Zhong, Y. Liu, H. Zheng, J.W. Wang, J.H. Cho, S. A. Dayeh, S.T. Picraux, J.P. Sullivan, S.X. Mao, Z.Z. Ye, J.Y. Huang, Ultrafast electrochemical lithiation of individual Si nanowire anodes, Nano Lett 11 (2011) 2251–2258.

[63] M. Chen, Q. Zhou, J. Zai, A. Iqbal, T. Tsega, B. Dong, X. Liu, Y. Zhang, C. Yan, L. Zhao, A. Nazakat, S. E, C. Low, X. Qian, High power and stable P-doped yolk-shell structured Si@C anode simultaneously enhancing conductivity and Li$^+$ diffusion kinetics, Nano Res 14 (2020) 1004–1011.

[64] H. Kim, M. Seo, M.H. Park, J. Cho, A critical size of silicon nano-anodes for lithium rechargeable batteries, Angew. Chem. Int. Ed. 49 (2010) 2192–2195.

[65] H. Kim, B. Han, J. Choo, J. Cho, Three-dimensional porous silicon particles for use in high-performance lithium secondary batteries, Angew. Chem. Int. Ed. 120 (2008) 10305–10308.

[66] L. Yang, H.S. Chen, H. Jiang, Y.J. Wei, W.L. Song, D.N. Fang, Failure mechanisms of 2D silicon film anodes: *In situ* observations and simulations on crack evolution, Chem. Commun (Camb) 54 (2018) 3997–4000.

[67] M. Pharr, Z. Suo, J.J. Vlassak, Measurements of the fracture energy of lithiated silicon electrodes of Li-ion batteries, Nano Lett 13 (2013) 5570–5577.

[68] V.A. Sethuraman, M.J. Chon, M. Shimshak, N. Van Winkle, P.R. Guduru, In situ measurement of biaxial modulus of Si anode for Li-ion batteries, Electrochem. Commun. 12 (2010) 1614–1617.

[69] F. Yang, Criterion for insertion-induced microcracking and debonding of thin films, J. Power Sources 196 (2011) 465–469.

[70] A. Mukanova, A. Jetybayeva, S.T. Myung, S.S. Kim, Z. Bakenov, A mini-review on the development of Si-based thin film anodes for Li-ion batteries, Mater. Today Energy 9 (2018) 49–66.

[71] J.W. Long, B. Dunn, D.R. Rolison, H.S. White, Three-dimensional battery architectures, Chem. Rev. 104 (2004) 4463–4492.

[72] J. Wan, H.J. Yan, R. Wen, L.J. Wan, *In situ* visualization of electrochemical processes in solid-state lithium batteries, ACS Energy Lett 7 (2022) 2988–3002.

[73] H. Wu, G. Chan, J.W. Choi, I. Ryu, Y. Yao, M.T. McDowell, S.W. Lee, A. Jackson, Y. Yang, L. Hu, Y. Cui, Stable cycling of double-walled silicon nanotube battery anodes through solid-electrolyte interphase control, Nat. Nanotechnol. 7 (2012) 310–315.

[74] Y. He, L. Jiang, T. Chen, Y. Xu, H. Jia, R. Yi, D. Xue, M. Song, A. Genc, C. Bouchet-Marquis, L. Pullan, T. Tessner, J. Yoo, X. Li, J.G. Zhang, S. Zhang, C. Wang, Progressive growth of the solid-electrolyte interphase towards the Si anode interior causes capacity fading, Nat. Nanotechnol. 16 (2021) 1113–1120.

[75] K. Schroder, J. Alvarado, T.A. Yersak, J. Li, N. Dudney, L.J. Webb, Y.S. Meng, K. J. Stevenson, The effect of fluoroethylene carbonate as an additive on the solid electrolyte interphase on silicon lithium-ion electrodes, Chem. Mater. 27 (2015) 5531–5542.

[76] K.W. Schroder, A.G. Dylla, S.J. Harris, L.J. Webb, K.J. Stevenson, Role of surface oxides in the formation of solid-electrolyte interphases at silicon electrodes for lithium-ion batteries, ACS Appl. Mater. Interfaces 6 (2014) 21510–21524.

[77] C. Cao, I.I. Abate, E. Sivonxay, B. Shyam, C. Jia, B. Moritz, T.P. Devereaux, K. A. Persson, H.G. Steinrück, M.F. Toney, Solid electrolyte interphase on native oxide-terminated silicon anodes for Li-ion batteries, Joule 3 (2019) 762–781.

[78] E. Radvanyi, E. De Vito, W. Porcher, S. Jouanneau Si Larbi, An XPS/AES comparative study of the surface behaviour of nano-silicon anodes for Li-ion batteries, J. Anal. At. Spectrom. 29 (2014) 1120–1131.

[79] B. Philippe, R. Dedryvère, M. Gorgoi, H. Rensmo, D. Gonbeau, K. Edström, Role of the LiPF$_6$ salt for the long-term stability of silicon electrodes in Li-ion batteries – a photoelectron spectroscopy study, Chem. Mater. 25 (2013) 394–404.

[80] C.K. Chan, R. Ruffo, S.S. Hong, Y. Cui, Surface chemistry and morphology of the solid electrolyte interphase on silicon nanowire lithium-ion battery anodes, J. Power Sources 189 (2009) 1132–1140.

[81] G.M. Veith, M. Doucet, R.L. Sacci, B. Vacaliuc, J.K. Baldwin, J.F. Browning, Determination of the solid electrolyte interphase structure grown on a silicon electrode using a fluoroethylene carbonate additive, Sci. Rep. 7 (2017) 6326–6340.

[82] B. Philippe, R. Dedryvère, J. Allouche, F. Lindgren, M. Gorgoi, H. Rensmo, D. Gonbeau, K. Edström, Nanosilicon electrodes for lithium-ion batteries: Interfacial mechanisms studied by hard and soft X-ray photoelectron spectroscopy, Chem. Mater. 24 (2012) 1107–1115.

[83] C. Cao, H.G. Steinrück, B. Shyam, M.F. Toney, The atomic scale electrochemical lithiation and delithiation process of silicon, Adv. Mater. Interfaces 4 (2017) 1700771–1700777.

[84] W. Huang, J. Wang, M.R. Braun, Z. Zhang, Y. Li, D.T. Boyle, P.C. McIntyre, Y. Cui, Dynamic structure and chemistry of the silicon solid-electrolyte interphase visualized by cryogenic electron microscopy, Matter 1 (2019) 1232–1245.

[85] X. Zhang, S. Weng, G. Yang, Y. Li, H. Li, D. Su, L. Gu, Z. Wang, X. Wang, L. Chen, Interplay between solid-electrolyte interphase and (in)active Li$_x$Si in silicon anode, Cell Rep. Phys. Sci. 2 (2021) 100668–100679.

[86] Z. Chen, A. Soltani, Y. Chen, Q. Zhang, A. Davoodi, S. Hosseinpour, W. Peukert, W. Liu, Emerging organic surface chemistry for Si anodes in lithium-ion batteries: Advances, prospects, and beyond, Adv. Energy Mater. 12 (2022) 2200924.

[87] R. Endo, T. Ohnishi, K. Takada, T. Masuda, In situ observation of lithiation and delithiation reactions of a silicon thin film electrode for all-solid-state lithium-ion batteries by X-ray photoelectron spectroscopy, J. Phys. Chem. Lett. 11 (2020) 6649–6654.

[88] L. Gu, J. Han, M. Chen, W. Zhou, X. Wang, M. Xu, H. Lin, H. Liu, H. Chen, J. Chen, Q. Zhang, X. Han, Enabling robust structural and interfacial stability of micron-Si anode toward high-performance liquid and solid-state lithium-ion batteries, Energy Storage Mater. 52 (2022) 547–561.

[89] C. Shen, R. Fu, Y. Xia, Z. Liu, New perspective to understand the effect of electrochemical prelithiation behaviors on silicon monoxide, RSC Adv 8 (2018) 14473–14478.

[90] K. Kanamura, H. Takezawa, S. Shiraishi, Z.i. Takehara, Chemical reaction of lithium surface during immersion in LiClO$_4$ or LiPF$_6$ / DEC electrolyte, J. Electrochem. Soc. 144 (2019) 1900–1906.

[91] K. Yamada, H. Tsutsumi, Y. Katayama, Electro)chemical processes of poly (ethylene oxide)-based electrolyte on Cu surface during lithium secondary battery operation, Energy Technol 11 (2023) 2201286.

[92] Y. Zhang, W. Feng, Y. Zhen, P. Zhao, X. Wang, L. Li, Effects of lithium salts on PEO-based solid polymer electrolytes and their all-solid-state lithium-ion batteries, Ionics 28 (2022) 2751–2758.

[93] C. Xu, B. Sun, T. Gustafsson, K. Edström, D. Brandell, M. Hahlin, Interface layer formation in solid polymer electrolyte lithium batteries: An XPS study, J. Mater. Chem. A 2 (2014) 7256–7264.

[94] F.P. McGrogan, T. Swamy, S.R. Bishop, E. Eggleton, L. Porz, X.W. Chen, Y. M. Chiang, K.J. Van Vliet, Compliant yet brittle mechanical behavior of Li$_2$S-P$_2$S$_5$

[95] lithium-ion-conducting solid electrolyte, Adv. Energy Mater. 7 (2017) 1602011–1602015.

[95] J. Tippens, J.C. Miers, A. Afshar, J.A. Lewis, F.J.Q. Cortes, H. Qiao, T.S. Marchese, C.V. Di Leo, C. Saldana, M.T. McDowell, Visualizing chemomechanical degradation of a solid-state battery electrolyte, ACS Energy Lett 4 (2019) 1475–1483.

[96] W. Zhang, D. Schröder, T. Arlt, I. Manke, R. Koerver, R. Pinedo, D.A. Weber, J. Sann, W.G. Zeier, J. Janek, Electro)chemical expansion during cycling: Monitoring the pressure changes in operating solid-state lithium batteries, J. Mater. Chem. A 5 (2017) 9929–9936.

[97] S. Jun, Y.J. Nam, H. Kwak, K.T. Kim, D.Y. Oh, Y.S. Jung, Operando differential electrochemical pressiometry for probing electrochemo-mechanics in all-solid-state batteries, Adv. Funct. Mater. 30 (2020) 2138–2158.

[98] M.B. Dixit, N. Singh, J.P. Horwath, P.D. Shevchenko, M. Jones, E.A. Stach, T. S. Arthur, K.B. Hatzell, In situ investigation of chemomechanical effects in thiophosphate solid electrolytes, Matter 3 (2020) 2138–2159.

[99] A. Verma, H. Kawakami, H. Wada, A. Hirowatari, N. Ikeda, Y. Mizuno, T. Kotaka, K. Aotani, Y. Tabuchi, P.P. Mukherjee, Microstructure and pressure-driven electrodeposition stability in solid-state batteries, Cell Rep. Phys. Sci. 2 (2021) 100301–100322.

[100] S.Y. Han, C. Lee, J.A. Lewis, D. Yeh, Y. Liu, H.W. Lee, M.T. McDowell, Stress evolution during cycling of alloy-anode solid-state batteries, Joule 5 (2021) 2450–2465.

[101] D.M. Piper, T.A. Yersak, S.H. Lee, Effect of compressive stress on electrochemical performance of silicon anodes, J. Electrochem. Soc. 160 (2012) A77–A81.

[102] S.B. Son, J.E. Trevey, H. Roh, S.H. Kim, K.B. Kim, J.S. Cho, J.T. Moon, C. M. DeLuca, K.K. Maute, M.L. Dunn, H.N. Han, K.H. Oh, S.H. Lee, Microstructure study of electrochemically driven Li$_x$Si, Adv. Energy Mater. 1 (2011) 1199–1204.

[103] R. Koerver, W. Zhang, L. de Biasi, S. Schweidler, A.O. Kondrakov, S. Kolling, T. Brezesinski, P. Hartmann, W.G. Zeier, J. Janek, Chemo-mechanical expansion of lithium electrode materials – on the route to mechanically optimized all-solid-state batteries, Energy Environ. Sci. 11 (2018) 2142–2158.

[104] H. Liu, Q. Sun, H. Zhang, J. Cheng, Y. Li, Z. Zeng, S. Zhang, X. Xu, F. Ji, D. Li, J. Lu, L. Ci, The application road of silicon-based anode in lithium-ion batteries: From liquid electrolyte to solid-state electrolyte, Energy Storage Mater. 55 (2023) 244–263.

[105] B.J. Neudecker, R.A. Zuhr, J.B. Bates, Lithium silicon tin oxynitride (Li$_y$SiTON): High-performance anode in thin-film lithium-ion batteries for microelectronics, J. Power Sources 81-82 (1999) 27–32.

[106] P.H.L. Notten, F. Roozeboom, R.A.H. Niessen, L. Baggetto, 3-D integrated all-solid-state rechargeable batteries, Adv. Mater. 19 (2007) 4564–4567.

[107] J.E. Trevey, J. Wang, C.M. DeLuca, K.K. Maute, M.L. Dunn, S.H. Lee, V.M. Bright, Nanostructured silicon electrodes for solid-state 3-D rechargeable lithium batteries, Sens. Actuators A Phys 167 (2011) 139–145.

[108] C. Chen, Q. Li, Y. Li, Z. Cui, X. Guo, H. Li, Sustainable interfaces between Si anodes and garnet electrolytes for room-temperature solid-state batteries, ACS Appl. Mater. Interfaces 10 (2018) 2185–2190.

[109] H. Huo, J. Janek, Silicon as emerging anode in solid-state batteries, ACS Energy Lett 7 (2022) 4005–4016.

[110] D. Cao, X. Sun, Y. Wang, H. Zhu, Bipolar stackings high voltage and high cell level energy density sulfide based all-solid-state batteries, Energy Storage Mater. 48 (2022) 458–465.

[111] Y. Chen, Z. Tang, S. Yang, Y. Wang, D. Chua, A high-voltage all-solid-state lithium-ion battery with Li-Mn-Ni-O and silicon thin-film electrodes, Mater. Technol. 30 (2015) A58–A63.

[112] S. Kanazawa, T. Baba, K. Yoneda, M. Mizuhata, I. Kanno, Deposition and performance of all solid-state thin-film lithium-ion batteries composed of amorphous Si/LiPON/VO-LiPO multilayers, Thin Solid Films 697 (2020) 137840–137843.

[113] S.J. Lee, H.K. Baik, S.M. Lee, An all-solid-state thin film battery using LiSiPON electrolyte and Si–V negative electrode films, Electrochem. Commun. 5 (2003) 32–35.

[114] D. Cao, T. Ji, A. Singh, S. Bak, Y. Du, X. Xiao, H. Xu, J. Zhu, H. Zhu, Unveiling the mechanical and electrochemical evolution of nanosilicon composite anodes in sulfide-based all-solid-state batteries, Adv. Energy Mater. (2023) 2203969–2203981.

[115] W. Ji, X. Zhang, M. Liu, T. Ding, H. Qu, D. Qiu, D. Zheng, D. Qu, High-performance all-solid-state Li-S batteries enabled by an all-electrochem-active prelithiated Si anode, Energy Storage Mater. 53 (2022) 613–620.

[116] S. Cangaz, F. Hippauf, F.S. Reuter, S. Doerfler, T. Abendroth, H. Althues, S. Kaskel, Enabling high-energy solid-state batteries with stable anode interphase by the use of columnar silicon anodes, Adv. Energy Mater. 10 (2020) 2001320–2001329.

[117] S. Poetke, F. Hippauf, A. Baasner, S. Dörfler, H. Althues, S. Kaskel, Nanostructured Si-C composites as high-capacity anode material for all-solid-state lithium-ion batteries**, Batteries Supercaps 4 (2021) 1323–1334.

[118] J.Y. Kim, S. Jung, S.H. Kang, M.J. Lee, D. Jin, D.O. Shin, Y.G. Lee, Y.M. Lee, All-solid-state hybrid electrode configuration for high-performance all-solid-state batteries: Comparative study with composite electrode and diffusion-dependent electrode, J. Power Sources 518 (2022) 230736–230743.

[119] L. Hu, X. Yan, Z. Fu, J. Zhang, Y. Xia, W. Zhang, Y. Gan, X. He, H. Huang, A "reinforced concrete" structure of silicon embedded into an in situ grown carbon nanotube scaffold as a high-performance anode for sulfide-based all-solid-state batteries, ACS Appl. Energy Mater. 5 (2022) 14353–14360.

[120] J. Kim, C. Kim, I. Jang, J. Park, J. Kim, U. Paik, T. Song, Si nanoparticles embedded in carbon nanofiber sheathed with Li6PS5Cl as an anode material for all-solid-state batteries, J. Power Sources 510 (2021) 230425–230432.

[121] M. Branchi, G. Maresca, A. Tsurumaki, N. Suzuki, F. Croce, S. Panero, J. Voje, Y. Aihara, M.A. Navarra, Silicon-based composite anodes for all-solid-state lithium-ion batteries conceived by a mixture design approach, ChemSusChem 16 (2022), e202202235.

[122] N. Ohta, S. Kimura, J. Sakabe, K. Mitsuishi, T. Ohnishi, K. Takada, Anode properties of Si nanoparticles in all-solid-state Li batteries, ACS Appl. Energy Mater. 2 (2019) 7005–7008.

[123] J. Sakabe, N. Ohta, T. Ohnishi, K. Mitsuishi, K. Takada, Porous amorphous silicon film anodes for high-capacity and stable all-solid-state lithium batteries, Commun. Chem. 1 (2018) 24–32.

[124] J. Trevey, J.S. Jang, Y.S. Jung, C.R. Stoldt, S.H. Lee, Glass-ceramic Li2S-P2S5 electrolytes prepared by a single step ball billing process and their application for all-solid-state lithium-ion batteries, Electrochem. Commun. 11 (2009) 1830–1833.

[125] N.A. Dunlap, J. Kim, H. Guthery, C.S. Jiang, I. Morrissey, C.R. Stoldt, K.H. Oh, M. Al-Jassim, S.H. Lee, Towards the commercialization of the all-solid-state Li-ion battery: Local bonding structure and the reversibility of sheet-style Si-PAN anodes, J. Electrochem. Soc. 167 (2020) 060522–060529.

[126] K.B. Kim, N.A. Dunlap, S.S. Han, J.J. Jeong, S.C. Kim, K.H. Oh, S.H. Lee, Nanostructured Si/C fibers as a highly reversible anode material for all-solid-state lithium-ion batteries, J. Electrochem. Soc. 165 (2018) A1903–A1908.

[127] N.A. Dunlap, S. Kim, J.J. Jeong, K.H. Oh, S.H. Lee, Simple and inexpensive coal-tar-pitch derived Si-C anode composite for all-solid-state Li-ion batteries, Solid State Ionics 324 (2018) 207–217.

[128] R. Okuno, M. Yamamoto, A. Kato, M. Takahashi, Stable cyclability caused by highly dispersed nanoporous Si composite anodes with sulfide-based solid electrolyte, J. Electrochem. Soc. 167 (2020) 140522–140529.

[129] R. Okuno, M. Yamamoto, A. Kato, M. Takahashi, High cycle stability of nanoporous Si composites in all-solid-state lithium-ion batteries, J. Electrochem. Soc. 169 (2022) 080502–080509.

[130] R. Okuno, M. Yamamoto, A. Kato, M. Takahashi, Performance improvement of nanoporous Si composite anodes in all-solid-state lithium-ion batteries by using acetylene black as a conductive additive, Electrochem. Commun. 138 (2022) 107288–107293.

[131] M. Yamamoto, Y. Terauchi, A. Sakuda, M. Takahashi, Slurry mixing for fabricating silicon-composite electrodes in all-solid-state batteries with high areal capacity and cycling stability, J. Power Sources 402 (2018) 506–512.

[132] D.H. Kim, H.A. Lee, Y.B. Song, J.W. Park, S.M. Lee, Y.S. Jung, Sheet-type Li6PS5Cl-infiltrated Si anodes fabricated by solution process for all-solid-state lithium-ion batteries, J. Power Sources 426 (2019) 143–150.

[133] Y.S. Oh, M. Kim, S. Kang, J.Y. Park, H.T. Lim, Redox activity of Li2S-P2S5 electrolyte inducing chemo-mechanical failure in all-solid-state batteries comprising sulfur composite cathode and Li-Si alloy anode, Chem. Eng. J. 442 (2022) 136229–136239.

[134] M. Yamamoto, Y. Terauchi, A. Sakuda, A. Kato, M. Takahashi, Effects of volume variations under different compressive pressures on the performance and microstructure of all-solid-state batteries, J. Power Sources 473 (2020) 228595–228604.

[135] H.W. Park, J.H. Song, H. Choi, J.S. Jin, H.T. Lim, Anode performance of lithium-silicon alloy prepared by mechanical alloying for use in all-solid-state lithium secondary batteries, Jap. J. Appl. Phys. 53 (2014) 08NK02.

[136] R. Miyazaki, N. Ohta, T. Ohnishi, I. Sakaguchi, K. Takada, An amorphous Si film anode for all-solid-state lithium batteries, J. Power Sources 272 (2014) 541–545.

[137] B.T. Hang, T. Ohnishi, M. Osada, X. Xu, K. Takada, T. Sasaki, Lithium silicon sulfide as an anode material in all-solid-state lithium batteries, J. Power Sources 195 (2010) 3323–3327.

[138] X. Xu, J. Cheng, Y. Li, X. Nie, L. Dai, L. Ci, Li metal-free rechargeable all-solid-state Li2S/Si battery based on Li7P3S11 electrolyte, J. Solid State Electr. 23 (2019) 3145–3151.

[139] N. Suzuki, R.B. Cervera, T. Ohnishi, K. Takada, Silicon nitride thin film electrode for lithium-ion batteries, J. Power Sources 231 (2013) 186–189.

[140] Y. Hashimoto, N. Machida, T. Shigematsu, Preparation of Li4.4GexSi1-x alloys by mechanical milling process and their properties as anode materials in all-solid-state lithium batteries, Solid State Ionics 175 (2004) 177–180.

[141] G. Ferraresi, M. El Kazzi, L. Czornomaz, C.L. Tsai, S. Uhlenbruck, C. Villevieille, Electrochemical performance of all-solid-state Li-ion batteries based on garnet electrolyte using silicon as a model electrode, ACS Energy Lett 3 (2018) 1006–1012.

[142] W. Ping, C. Yang, Y. Bao, C. Wang, H. Xie, E. Hitz, J. Cheng, T. Li, L. Hu, A silicon anode for garnet-based all-solid-state batteries: Interfaces and nanomechanics, Energy Storage Mater. 21 (2019) 246–252.

[143] L. Zhang, Y. Lin, X. Peng, M. Wu, T. Zhao, A high-capacity polyethylene oxide-based all-solid-state battery using a metal-organic framework hosted silicon anode, ACS Appl. Mater. Interfaces 14 (2022) 24798–24805.

[144] X. Han, W. Zhou, M. Chen, J. Chen, G. Wang, B. Liu, L. Luo, S. Chen, Q. Zhang, S. Shi, C.P. Wong, Interfacial nitrogen engineering of robust silicon/MXene anode toward high energy solid-state lithium-ion batteries, J. Energy Chem. 67 (2022) 727–735.

[145] R. Miyazaki, T. Hihara, All-solid-state half-cell of Li/a-Si film using guest Li+ conductor 15NaI•LiBH4 as a solid electrolyte, J. Solid State Electr. 24 (2020) 1687–1693.

[146] J.B. Bates, N.J. Dudney, G.R. Gruzalski, R.A. Zuhr, A. Choudhury, C.F. Luck, J. D. Robertson, Fabrication and characterization of amorphous lithium electrolyte

[147] thin films and rechargeable thin-film batteries, J. Power Sources 43 (1993) 103–110.

[147] J. Bates, Thin-film lithium and lithium-ion batteries, Solid State Ionics 135 (2000) 33–45.

[148] J.B. Bates, N.J. Dudney, B.J. Neudecker, F.X. Hart, H.P. Jun, S.A. Hackney, Preferred orientation of polycrystalline LiCoO2 films, J. Electrochem. Soc. 147 (2000) 59–71.

[149] J.B. Bates, N.J. Dudney, G.R. Gruzalski, R.A. Zuhr, A. Choudhury, C.F. Luck, J. D. Robertson, Electrical properties of amorphous lithium electrolyte thin films, Solid State Ionics 53 (1992) 647–654.

[150] J.B. Bates, D. Lubben, N.J. Dudney, F.X. Hart, 5 volt plateau in LiMn2O4 thin films, J. Electrochem. Soc. 142 (2019) L149–L151.

[151] B. Wang, J.B. Bates, F.X. Hart, B.C. Sales, R.A. Zuhr, J.D. Robertson, Characterization of thin-film rechargeable lithium batteries with lithium cobalt oxide cathodes, J. Electrochem. Soc. 143 (1996) 3203–3213.

[152] X.H. Yu, J.B. Bates, G.E. Jellison, F.X. Hart, A stable thin-film lithium electrolyte: Lithium phosphorus oxynitride, J. Electrochem. Soc. 144 (1997) 524–532.

[153] N.J. Dudney, Solid-state thin-film rechargeable batteries, Mater. Sci. Eng. B 116 (2005) 245–249.

[154] S. Nowak, F. Berkemeier, G. Schmitz, Ultra-thin LiPON films - fundamental properties and application in solid state thin film model batteries, J. Power Sources 275 (2015) 144–150.

[155] C. Ma, K. Chen, C. Liang, C.W. Nan, R. Ishikawa, K. More, M. Chi, Atomic-scale origin of the large grain-boundary resistance in perovskite Li-ion-conducting solid electrolytes, Energy Environ. Sci. 7 (2014) 1638–1642.

[156] L. Porz, T. Swamy, B.W. Sheldon, D. Rettenwander, T. Frömling, H.L. Thaman, S. Berendts, R. Uecker, W.C. Carter, Y.M. Chiang, Mechanism of lithium metal penetration through inorganic solid electrolytes, Adv. Energy Mater. 7 (2017) 1701003–1701014.

[157] S. Zhao, Z. Fu, Q. Qin, A solid-state electrolyte lithium phosphorus oxynitride film prepared by pulsed laser deposition, Thin Solid Films 415 (2002) 108–113.

[158] H.T. Kim, T. Mun, C. Park, S.W. Jin, H.Y. Park, Characteristics of lithium phosphorous oxynitride thin films deposited by metal-organic chemical vapor deposition technique, J. Power Sources 244 (2013) 641–645.

[159] Y.G. Kim, H.N.G. Wadley, Lithium phosphorous oxynitride films synthesized by a plasma-assisted directed vapor deposition approach, J. Vac. Sci. Technol. A 26 (2008) 174–183.

[160] W.Y. Liu, Z.W. Fu, C.L. Li, Q.Z. Qin, Lithium phosphorus oxynitride thin film fabricated by a nitrogen plasma-assisted deposition of E-beam reaction evaporation, Electrochem. Solid-State Lett. 7 (2004) J36–J40.

[161] C.H. Choi, W.I. Cho, B.W. Cho, H.S. Kim, Y.S. Yoon, Y.S. Tak, Radio-frequency magnetron sputtering power effect on the ionic conductivities of LiPON films, Electrochem. Solid-State Lett. 5 (2002) A14–A17.

[162] B. Wang, B.S. Kwak, B.C. Sales, J.B. Bates, Ionic conductivities and structure of lithium phosphorus oxynitride glasses, J. Non-Cryst. Solids 183 (1995) 297–306.

[163] M.A.T. Marple, T.A. Wynn, D. Cheng, R. Shimizu, H.E. Mason, Y.S. Meng, Local structure of glassy lithium phosphorus oxynitride thin films: A combined experimental and ab initio approach, Angew. Chem. Int. Ed. 59 (2020) 22185–22193.

[164] V. Lacivita, N. Artrith, G. Ceder, Structural and compositional factors that control the Li-ion conductivity in LiPON electrolytes, Chem. Mater. 30 (2018) 7077–7090.

[165] D. Cheng, T.A. Wynn, X. Wang, S. Wang, M. Zhang, R. Shimizu, S. Bai, H. Nguyen, C. Fang, M.-c. Kim, W. Li, B. Lu, S.J. Kim, Y.S. Meng, Unveiling the stable nature of the solid electrolyte interphase between lithium metal and LiPON via cryogenic electron microscopy, Joule 4 (2020) 2484–2500.

[166] A.A. Talin, D. Ruzmetov, A. Kolmakov, K. McKelvey, N. Ware, F. El Gabaly, B. Dunn, H.S. White, Fabrication, testing, and simulation of all-solid-state three-dimensional Li-ion batteries, ACS Appl. Mater. Interfaces 8 (2016) 32385–32391.

[167] D. Santhanagopalan, D. Qian, T. McGilvray, Z. Wang, F. Wang, F. Camino, J. Graetz, N. Dudney, Y.S. Meng, Interface limited lithium transport in solid-state batteries, J. Phys. Chem. Lett. 5 (2014) 298–303.

[168] E.J. Fuller, E. Strelcov, J.L. Weaver, M.W. Swift, J.D. Sugar, A. Kolmakov, N. Zhitenev, J.J. McClelland, Y. Qi, J.A. Dura, A.A. Talin, Spatially resolved potential and Li-ion distributions reveal performance-limiting regions in solid-state batteries, ACS Energy Lett 6 (2021) 3944–3951.

[169] J. Lin, J. Guo, C. Liu, H. Guo, Artificial solid electrolyte interphase with in-situ formed porosity for enhancing lithiation of silicon wafer, J. Power Sources 336 (2016) 401–407.

[170] R. Chen, Q. Li, X. Yu, L. Chen, H. Li, Approaching practically accessible solid-state batteries: Stability issues related to solid electrolytes and interfaces, Chem. Rev. 120 (2020) 6820–6877.

[171] X. Wang, K. He, S. Li, J. Zhang, Y. Lu, Realizing high-performance all-solid-state batteries with sulfide solid electrolyte and silicon anode: A review, Nano Res 16 (2022) 3741–3765.

[172] J. Lau, R.H. DeBlock, D.M. Butts, D.S. Ashby, C.S. Choi, B.S. Dunn, Sulfide solid electrolytes for lithium battery applications, Adv. Energy Mater. 8 (2018), 1800933.

[173] F.P. McGrogan, T. Swamy, S.R. Bishop, E. Eggleton, L. Porz, X. Chen, Y.M. Chiang, K.J. Van Vliet, Compliant yet brittle mechanical behavior of Li2S-P2S5 lithium-ion-conducting solid electrolyte, Adv. Energy Mater. 7 (2017) 1602011–1602015.

[174] A. Sakuda, A. Hayashi, M. Tatsumisago, Sulfide solid electrolyte with favorable mechanical property for all-solid-state lithium battery, Sci. Rep. 3 (2013) 2261–2265.

[175] Q. Zhang, D. Cao, Y. Ma, A. Natan, P. Aurora, H. Zhu, Sulfide-based solid-state electrolytes: Synthesis, stability, and potential for all-solid-state batteries, Adv. Mater. 31 (2019), e1901131.

[176] S.P. Culver, R. Koerver, W.G. Zeier, J. Janek, On the functionality of coatings for cathode active materials in thiophosphate-based all-solid-state batteries, Adv. Energy Mater. 9 (2019), 1900626.

[177] Ö.U. Kudu, T. Famprikis, B. Fleutot, M.D. Braida, T.Le Mercier, M.S. Islam, C. Masquelier, A review of structural properties and synthesis methods of solid electrolyte materials in the $Li_2S-P_2S_5$ binary system, J. Power Sources 407 (2018) 31–43.

[178] S. Shiotani, K. Ohara, H. Tsukasaki, S. Mori, R. Kanno, Pair distribution function analysis of sulfide glassy electrolytes for all-solid-state batteries: Understanding the improvement of ionic conductivity under annealing condition, Sci. Rep. 7 (2017) 6972–6978.

[179] S. Chen, D. Xie, G. Liu, J.P. Mwizerwa, Q. Zhang, Y. Zhao, X. Xu, X. Yao, Sulfide solid electrolytes for all-solid-state lithium batteries: Structure, conductivity, stability and application, Energy Storage Mater. 14 (2018) 58–74.

[180] A. Miura, N.C. Rosero-Navarro, A. Sakuda, K. Tadanaga, N.H.H. Phuc, A. Matsuda, N. Machida, A. Hayashi, M. Tatsumisago, Liquid-phase syntheses of sulfide electrolytes for all-solid-state lithium battery, Nat. Rev. Chem. 3 (2019) 189–198.

[181] Y. Kato, S. Hori, R. Kanno, $Li_{10}GeP_2S_{12}$-type superionic conductors: Synthesis, structure, and ionic transportation, Adv. Energy Mater. 10 (2020), 2002153.

[182] T. Minami, A. Hayashi, M. Tatsumisago, Recent progress of glass and glass-ceramics as solid electrolytes for lithium secondary batteries, Solid State Ionics 177 (2006) 2715–2720.

[183] K.H. Park, Q. Bai, D.H. Kim, D.Y. Oh, Y. Zhu, Y. Mo, Y.S. Jung, Design strategies, practical considerations, and new solution processes of sulfide solid electrolytes for all-solid-state batteries, Adv. Energy Mater. 8 (2018) 1800035–1800058.

[184] C. Wang, J. Liang, Y. Zhao, M. Zheng, X. Li, X. Sun, All-solid-state lithium batteries enabled by sulfide electrolytes: From fundamental research to practical engineering design, Energy Environ. Sci. 14 (2021) 2577–2619.

[185] Y. Kato, S. Hori, T. Saito, K. Suzuki, M. Hirayama, A. Mitsui, M. Yonemura, H. Iba, R. Kanno, High-power all-solid-state batteries using sulfide superionic conductors, Nat. Energy 1 (2016) 16030–16036.

[186] R. Iwasaki, S. Hori, R. Kanno, T. Yajima, D. Hirai, Y. Kato, Z. Hiroi, Weak anisotropic lithium-ion conductivity in single crystals of $Li_{10}GeP_2S_{12}$, Chem. Mater. 31 (2019) 3694–3699.

[187] K. Kaup, L. Zhou, A. Huq, L.F. Nazar, Impact of the Li substructure on the diffusion pathways in alpha and beta Li_3PS_4: An *in situ* high temperature neutron diffraction study, J. Mater. Chem. A 8 (2020) 12446–12456.

[188] Z. Liu, W. Fu, E.A. Payzant, X. Yu, Z. Wu, N.J. Dudney, J. Kiggans, K. Hong, A. J. Rondinone, C. Liang, Anomalous high ionic conductivity of nanoporous beta-Li_3PS_4, J. Am. Chem. Soc. 135 (2013) 975–978.

[189] T. Kaib, S. Haddadpour, M. Kapitein, P. Bron, C. Schröder, H. Eckert, B. Roling, S. Dehnen, New lithium chalcogenidotetrelates, LiCht: Synthesis and characterization of the Li$^+$-conducting tetralithium ortho-sulfidostannate Li_4SnS_4, Chem. Mater. 24 (2012) 2211–2219.

[190] G. Sahu, Z. Lin, J. Li, Z. Liu, N. Dudney, C. Liang, Air-stable, high-conduction solid electrolytes of arsenic-substituted Li_4SnS_4, Energy Environ. Sci. 7 (2014) 1053–1058.

[191] G. Sahu, E. Rangasamy, J. Li, Y. Chen, K. An, N. Dudney, C. Liang, A high-conduction Ge substituted Li_3AsS_4 solid electrolyte with exceptional low activation energy, J. Mater. Chem. A 2 (2014) 10396–10403.

[192] R. Kanno, M. Murayama, Lithium ionic conductor thio-Lisicon: The Li_2S-GeS_2-P_2S_5 system, J. Electrochem. Soc. 148 (2001) A742–A746.

[193] N. Kamaya, K. Homma, Y. Yamakawa, M. Hirayama, R. Kanno, M. Yonemura, T. Kamiyama, Y. Kato, S. Hama, K. Kawamoto, A. Mitsui, A lithium superionic conductor, Nat. Mater. 10 (2011) 682–686.

[194] O. Kwon, M. Hirayama, K. Suzuki, Y. Kato, T. Saito, M. Yonemura, T. Kamiyama, R. Kanno, Synthesis, structure, and conduction mechanism of the lithium superionic conductor $Li_{10+\delta}M_{1+\delta}P_{2-\delta}S_{12}$, J. Mater. Chem. A 3 (2015) 438–446.

[195] A. Kuhn, V. Duppel, B.V. Lotsch, Tetragonal $Li_{10}GeP_2S_{12}$ and Li_7GePS_8 - exploring the Li ion dynamics in LGPS Li electrolytes, Energy Environ. Sci. 6 (2013) 3548–3552.

[196] R.B. Beeken, J.J. Garbe, J.M. Gillis, N.R. Petersen, B.W. Podoll, M.R. Stoneman, Electrical conductivities of the Ag_6PS_5K and the Cu_6PSe_5X (X=Br, I) argyrodites, J. Phys. Chem. Solids 66 (2005) 882–886.

[197] H.M. Chen, C. Maohua, S. Adams, Stability and ionic mobility in argyrodite-related lithium-ion solid electrolytes, Phys Chem Chem Phys 17 (2015) 16494–16506.

[198] O. Pecher, S.T. Kong, T. Goebel, V. Nickel, K. Weichert, C. Reiner, H.J. Deiseroth, J. Maier, F. Haarmann, D. Zahn, Atomistic characterisation of Li+ mobility and conductivity in $Li_{7-x}PS_{6-x}I_x$ argyrodites from molecular dynamics simulations, solid-state NMR, and impedance spectroscopy, Chem. Eur. J. 16 (2010) 8347–8354.

[199] J. Liang, N. Chen, X. Li, X. Li, K.R. Adair, J. Li, C. Wang, C. Yu, M. Norouzi Banis, L. Zhang, S. Zhao, S. Lu, H. Huang, R. Li, Y. Huang, X. Sun, $Li_{10}Ge(P_{1-x}Sb_x)_2S_{12}$ lithium-ion conductors with enhanced atmospheric stability, Chem. Mater. 32 (2020) 2664–2672.

[200] F. Zhao, J. Liang, C. Yu, Q. Sun, X. Li, K. Adair, C. Wang, Y. Zhao, S. Zhang, W. Li, S. Deng, R. Li, Y. Huang, H. Huang, L. Zhang, S. Zhao, S. Lu, X. Sun, A versatile Sn-substituted argyrodite sulfide electrolyte for all-solid-state Li metal batteries, Adv. Energy Mater. 10 (2020) 1903422–1903431.

[201] H. Liu, Q. Zhu, C. Wang, G. Wang, Y. Liang, D. Li, L. Gao, L.Z. Fan, High air stability and excellent Li metal compatibility of argyrodite-based electrolyte enabling superior all-solid-state Li metal batteries, Adv. Funct. Mater. 32 (2022), 2203858.

[202] W.D. Richards, L.J. Miara, Y. Wang, J.C. Kim, G. Ceder, Interface stability in solid-state batteries, Chem. Mater. 28 (2015) 266–273.

[203] Y. Zhu, X. He, Y. Mo, Origin of outstanding stability in the lithium solid electrolyte materials: Insights from thermodynamic analyses based on first-principles calculations, ACS Appl. Mater. Interfaces 7 (2015) 23685–23693.

[204] Z. Zhang, L. Zhang, X. Yan, H. Wang, Y. Liu, C. Yu, X. Cao, L. van Eijck, B. Wen, All-in-one improvement toward Li_6PS_5Br-based solid electrolytes triggered by compositional tune, J. Power Sources 410-411 (2019) 162–170.

[205] S. Hori, K. Suzuki, M. Hirayama, Y. Kato, R. Kanno, Lithium superionic conductor $Li_{9.42}Si_{1.02}P_{2.1}S_{9.96}O_{2.04}$ with $Li_{10}GeP_2S_{12}$-type structure in the $Li_2S-P_2S_5-SiO_2$ pseudoternary system: Synthesis, electrochemical properties, and structure–composition relationships, Front. Energy Res. 4 (2016) 38–46.

[206] F. Wu, W. Fitzhugh, L. Ye, J. Ning, X. Li, Advanced sulfide solid electrolyte by core-shell structural design, Nat. Commun. 9 (2018) 4037–4047.

[207] W. Zhang, T. Leichtweiss, S.P. Culver, R. Koerver, D. Das, D.A. Weber, W.G. Zeier, J. Janek, The detrimental effects of carbon additives in $Li_{10}GeP_2S_{12}$-based solid-state batteries, ACS Appl. Mater. Interfaces 9 (2017) 35888–35896.

[208] D.H.S. Tan, E.A. Wu, H. Nguyen, Z. Chen, M.A.T. Marple, J.M. Doux, X. Wang, H. Yang, A. Banerjee, Y.S. Meng, Elucidating reversible electrochemical redox of Li_6PS_5Cl solid electrolyte, ACS Energy Lett 4 (2019) 2418–2427.

[209] G. Oh, M. Hirayama, O. Kwon, K. Suzuki, R. Kanno, Bulk-type all solid-state batteries with 5 V class $LiNi_{0.5}Mn_{1.5}O_4$ cathode and $Li_{10}GeP_2S_{12}$ solid electrolyte, Chem. Mater. 28 (2016) 2634–2640.

[210] M. Wu, B. Xu, C. Ouyang, Physics of electron and lithium-ion transport in electrode materials for Li-ion batteries, Chin. Phys. B 25 (2016) 018206–018216.

[211] B. Zhang, R. Tan, L. Yang, J. Zheng, K. Zhang, S. Mo, Z. Lin, F. Pan, Mechanisms and properties of ion-transport in inorganic solid electrolytes, Energy Storage Mater. 10 (2018) 139–159.

[212] Y. Wang, W.D. Richards, S.P. Ong, L.J. Miara, J.C. Kim, Y. Mo, G. Ceder, Design principles for solid-state lithium superionic conductors, Nat. Mater. 14 (2015) 1026–1031.

[213] D.H. Kim, D.Y. Oh, K.H. Park, Y.E. Choi, Y.J. Nam, H.A. Lee, S.M. Lee, Y.S. Jung, Infiltration of solution-processable solid electrolytes into conventional Li-ion-battery electrodes for all-solid-state Li-ion batteries, Nano Lett 17 (2017) 3013–3020.

[214] F. Hippauf, B. Schumm, S. Doerfler, H. Althues, S. Fujiki, T. Shiratsuchi, T. Tsujimura, Y. Aihara, S. Kaskel, Overcoming binder limitations of sheet-type solid-state cathodes using a solvent-free dry-film approach, Energy Storage Mater. 21 (2019) 390–398.

[215] T. Shi, Q. Tu, Y. Tian, Y. Xiao, L.J. Miara, O. Kononova, G. Ceder, High active material loading in all-solid-state battery electrode *via* particle size optimization, Adv. Energy Mater. 10 (2019), 1902881.

[216] Y. Xiao, K. Turcheniuk, A. Narla, A.Y. Song, X. Ren, A. Magasinski, A. Jain, S. Huang, H. Lee, G. Yushin, Electrolyte melt infiltration for scalable manufacturing of inorganic all-solid-state lithium-ion batteries, Nat. Mater. 20 (2021) 984–990.

[217] J. Ruhl, L.M. Riegger, M. Ghidiu, W.G. Zeier, Impact of solvent treatment of the superionic argyrodite Li_6PS_5Cl on solid-state battery performance, Adv. Energy Sustainability Res. 2 (2021) 2000077–2000086.

[218] M. Yamamoto, Y. Terauchi, A. Sakuda, M. Takahashi, Binder-free sheet-type all-solid-state batteries with enhanced rate capabilities and high energy densities, Sci. Rep. 8 (2018) 1212–1221.

[219] K. Yoon, J.J. Kim, W.M. Seong, M.H. Lee, K. Kang, Investigation on the interface between $Li_{10}GeP_2S_{12}$ electrolyte and carbon conductive agents in all-solid-state lithium battery, Sci. Rep. 8 (2018) 8066–8072.

[220] I. Na, H. Kim, S. Kunze, C. Nam, S. Jo, H. Choi, S. Oh, E. Choi, Y.B. Song, Y. S. Jung, Y.S. Lee, J. Lim, Monolithic 100% silicon wafer anode for all-solid-state batteries achieving high areal capacity at room temperature, ACS Energy Lett 8 (2023) 1936–1943.

[221] K.S. Ngai, S. Ramesh, K. Ramesh, J.C. Juan, A review of polymer electrolytes: Fundamental, approaches and applications, Ionics 22 (2016) 1259–1279.

[222] S. Rajendran, O. Mahendran, R. Kannan, Ionic conductivity studies in composite solid polymer electrolytes based on methylmethacrylate, J. Phys. Chem. Solids 63 (2002) 303–307.

[223] Q. Lu, Y.B. He, Q. Yu, B. Li, Y.V. Kaneti, Y. Yao, F. Kang, Q.H. Yang, Dendrite-free, high-rate, long-life lithium metal batteries with a 3D cross-linked network polymer electrolyte, Adv. Mater. 29 (2017) 19218–19253.

[224] Q. Zhang, K. Liu, F. Ding, X. Liu, Recent advances in solid polymer electrolytes for lithium batteries, Nano Res 10 (2017) 4139–4174.

[225] Z. Xue, D. He, X. Xie, Poly(ethylene oxide)-based electrolytes for lithium-ion batteries, J. Mater. Chem. A 3 (2015) 19218–19253.

[226] S. Zhao, Q. Wu, W. Ma, L. Yang, Polyethylene oxide-based composites as solid-state polymer electrolytes for lithium metal batteries: A mini review, Front Chem 8 (2020) 640–646.

[227] K. Nie, Y. Hong, J. Qiu, Q. Li, X. Yu, H. Li, L. Chen, Interfaces between cathode and electrolyte in solid state lithium batteries: Challenges and perspectives, Front Chem 6 (2018) 616–634.

[228] F. Croce, G.B. Appetecchi, L. Persi, B. Scrosati, Nanocomposite polymer electrolytes for lithium batteries, Nature 394 (1998) 456–458.

[229] L. Chen, Y. Li, S.P. Li, L.Z. Fan, C.W. Nan, J.B. Goodenough, PEO/garnet composite electrolytes for solid-state lithium batteries: From "ceramic-in-polymer" to "polymer-in-ceramic, Nano Energy 46 (2018) 176–184.

[230] K.B. Hueso, M. Armand, T. Rojo, High temperature sodium batteries: Status, challenges and future trends, Energy Environ. Sci. 6 (2013) 734–749.

[231] X.L. Wu, Y.H. Li, N. Wu, S. Xin, J.H. Kim, Y. Yan, J.S. Lee, Y.G. Guo, Enhanced working temperature of PEO-based polymer electrolyte *via* porous PTFE film as an efficient heat resister, Solid State Ionics 245-246 (2013) 1–7.

[232] S. Yu, R.D. Schmidt, R. Garcia-Mendez, E. Herbert, N.J. Dudney, J.B. Wolfenstine, J. Sakamoto, D.J. Siegel, Elastic properties of the solid electrolyte $Li_7La_3Zr_2O_{12}$ (LLZO), Chem. Mater. 28 (2015) 197–206.

[233] S. Kundu, A. Kraytsberg, Y. Ein-Eli, Recent development in the field of ceramics solid-state electrolytes: I—Oxide ceramic solid-state electrolytes, J. Solid State Electr. 26 (2022) 1809–1838.

[234] H. Huo, J. Sun, C. chen, X. Meng, M. He, N. Zhao, X. Guo, Flexible interfaces between Si anodes and composite electrolytes consisting of poly(propylene carbonates) and garnets for solid-state batteries, J. Power Sources 383 (2018) 150–156.

[235] J.P. Maranchi, A.F. Hepp, P.N. Kumta, High capacity, reversible silicon thin-film anodes for lithium-ion batteries, Electrochem. Solid-State Lett. 6 (2003).

[236] Z. Zhang, F. Xi, Q. Ma, X. Wan, S. Li, W. Ma, X. Chen, Z. Chen, R. Deng, J. Ji, H. J. Fan, C.M. Chong, A nanosilver-actuated high-performance porous silicon anode from recycling of silicon waste, Mater. Today Nano 17 (2022) 100162–100171.

[237] T.M. Higgins, S.H. Park, P.J. King, C.J. Zhang, N. McEvoy, N.C. Berner, D. Daly, A. Shmeliov, U. Khan, G. Duesberg, V. Nicolosi, J.N. Coleman, A commercial conducting polymer as both binder and conductive additive for silicon nanoparticle-based lithium-ion battery negative electrodes, ACS Nano 10 (2016) 3702–3713.

[238] M. Ge, J. Rong, X. Fang, A. Zhang, Y. Lu, C. Zhou, Scalable preparation of porous silicon nanoparticles and their application for lithium-ion battery anodes, Nano Res 6 (2013) 174–181.

[239] C. Wang, C. Yang, Z. Zheng, Toward practical high-energy and high-power lithium battery anodes: Present and future, Adv. Sci. (Weinh) 9 (2022), e2105213.

[240] L. Sun, Y. Liu, R. Shao, J. Wu, R. Jiang, Z. Jin, Recent progress and future perspective on practical silicon anode-based lithium ion batteries, Energy Storage Mater. 46 (2022) 482–502.

[241] A. Kohandehghan, K. Cui, M. Kupsta, E. Memarzadeh, P. Kalisvaart, D. Mitlin, Nanometer-scale Sn coatings improve the performance of silicon nanowire LIB anodes, J. Mater. Chem. A 2 (2014) 11261–11279.

[242] T. Shen, Z. Yao, X. Xia, X. Wang, C. Gu, J. Tu, Rationally designed silicon nanostructures as anode material for lithium-ion batteries, Adv. Eng. Mater. 20 (2018) 1700591–1700605.

[243] A.P. Yuda, P.Y.E. Koraag, F. Iskandar, H.S. Wasisto, A. Sumboja, Advances of the top-down synthesis approach for high-performance silicon anodes in Li-ion batteries, J. Mater. Chem. A 9 (2021) 18906–18926.

[244] W.S. Kim, Y. Hwa, J.H. Shin, M. Yang, H.J. Sohn, S.H. Hong, Scalable synthesis of silicon nanosheets from sand as an anode for Li-ion batteries, Nanoscale 6 (2014) 4297–4302.

[245] Q. Zhang, J. Liu, Z.Y. Wu, J.T. Li, L. Huang, S.G. Sun, 3D nanostructured multilayer Si/Al film with excellent cycle performance as anode material for lithium-ion battery, J. Alloys Compd. 657 (2016) 559–564.

[246] L. Zhang, L. Zhang, L. Chai, P. Xue, W. Hao, H. Zheng, A coordinatively cross-linked polymeric network as a functional binder for high-performance silicon submicro-particle anodes in lithium-ion batteries, J. Mater. Chem. A 2 (2014) 19036–19045.

[247] G. Liu, S. Xun, N. Vukmirovic, X. Song, P. Olalde-Velasco, H. Zheng, V. S. Battaglia, L. Wang, W. Yang, Polymers with tailored electronic structure for high capacity lithium battery electrodes, Adv. Mater. 23 (2011) 4679–4683.

[248] Z. Zhao, J. Han, F. Chen, J. Xiao, Y. Zhao, Y. Zhang, D. Kong, Z. Weng, S. Wu, Q. H. Yang, Liquid metal remedies silicon microparticulates toward highly stable and superior volumetric lithium storage, Adv. Energy Mater. 12 (2022) 2103565–2103572.

[249] F. Chen, J. Han, D. Kong, Y. Yuan, J. Xiao, S. Wu, D.M. Tang, Y. Deng, W. Lv, J. Lu, F. Kang, Q.H. Yang, 1000 Wh L−1 lithium-ion batteries enabled by crosslink-shrunk tough carbon encapsulated silicon microparticle anodes, Nat. Sci. Rev. 8 (2021) nwab012.

[250] R.B. Cervera, N. Suzuki, T. Ohnishi, M. Osada, K. Mitsuishi, T. Kambara, K. Takada, High performance silicon-based anodes in solid-state lithium batteries, Energy Environ. Sci. 7 (2014) 662–666.

[251] R. Okuno, M. Yamamoto, Y. Terauchi, M. Takahashi, Stable cyclability of porous Si anode applied for sulfide-based all-solid-state batteries, Energy Procedia 156 (2019) 183–186.

[252] I. Kovalenko, B. Zdyrko, A. Magasinski, B. Hertzberg, Z. Milicev, R. Burtovyy, I. Luzinov, G. Yushin, A major constituent of brown algae for use in high-capacity Li-ion batteries, Science 334 (2011) 75–79.

[253] M.H. Park, M.G. Kim, J. Joo, K. Kim, J. Kim, S. Ahn, Y. Cui, J. Cho, Silicon nanotube battery anodes, Nano Lett 9 (2009) 3844–3847.

[254] X.H. Liu, L. Zhong, S. Huang, S.X. Mao, T. Zhu, J.Y. Huang, Size-dependent fracture of silicon nanoparticles during lithiation, ACS Nano 6 (2012) 1522–1531.

[255] T.A. Yersak, J. Shin, Z. Wang, D. Estrada, J. Whiteley, S.H. Lee, M.J. Sailor, Y. S. Meng, Preparation of mesoporous Si@PAN electrodes for Li-ion batteries *via* the *in-situ* polymerization of PAN, ECS Electrochem. Lett. 4 (2015) A33–A36.

[256] Y.J. Nam, K.H. Park, D.Y. Oh, W.H. An, Y.S. Jung, Diagnosis of failure modes for all-solid-state Li-ion batteries enabled by three-electrode cells, J. Mater. Chem. A 6 (2018) 14867–14875.

[257] J.M. Whiteley, J.W. Kim, D.M. Piper, S.H. Lee, High-capacity and highly reversible silicon-tin hybrid anode for solid-state lithium-ion batteries, J. Electrochem. Soc. 163 (2015) A251–A254.

[258] T.A. Yersak, S.B. Son, J.S. Cho, S.S. Suh, Y.U. Kim, J.T. Moon, K.H. Oh, S.H. Lee, An all-solid-state Li-ion battery with a pre-lithiated Si-Ti-Ni alloy anode, J. Electrochem. Soc. 160 (2013) A1497–A1501.

[259] J.E. Trevey, K.W. Rason, C.R. Stoldt, S.H. Lee, Improved performance of all-solid-state lithium-ion batteries using nanosilicon active material with multiwalled-carbon-nanotubes as a conductive additive, Electrochem. Solid-State Lett. 13 (2010) A154–A157.

[260] J.Y. Kim, J. Park, M.J. Lee, S.H. Kang, D.O. Shin, J. Oh, J. Kim, K.M. Kim, Y. G. Lee, Y.M. Lee, Diffusion-dependent graphite electrode for all-solid-state batteries with extremely high energy density, ACS Energy Lett 5 (2020) 2995–3004.

[261] J.Y. Kim, J. Park, S.H. Kang, S. Jung, D.O. Shin, M.J. Lee, J. Oh, K.M. Kim, J. Zausch, Y.G. Lee, Y.M. Lee, Revisiting TiS_2 as a diffusion-dependent cathode with promising energy density for all-solid-state lithium secondary batteries, Energy Storage Mater. 41 (2021) 289–296.

[262] H. Li, Z. Chen, Z. Kang, W. Liu, Y. Chen, High-density crack-resistant Si-C microparticles for lithium ion batteries, Energy Storage Mater. 56 (2023) 40–49.

[263] M. Jiang, D.L. Danilov, R.A. Eichel, P.H.L. Notten, A review of degradation mechanisms and recent achievements for Ni-rich cathode-based Li-ion batteries, Adv. Energy Mater. 11 (2021) 2103005–2103048.

[264] D. Zuo, G. Tian, X. Li, D. Chen, K. Shu, Recent progress in surface coating of cathode materials for lithium ion secondary batteries, J. Alloys Compd. 706 (2017) 24–40.

[265] H. Wang, Z.D. Hood, Y. Xia, C. Liang, Fabrication of ultrathin solid electrolyte membranes of β-Li_3PS_4 nanoflakes by evaporation-induced self-assembly for all-solid-state batteries, J. Mater. Chem. A 4 (2016) 8091–8096.

[266] K.V. Kravchyk, F. Okur, M.V. Kovalenko, Break-even analysis of all-solid-state batteries with Li-garnet solid electrolytes, ACS Energy Lett 6 (2021) 2202–2207.

[267] M. Balaish, J.C. Gonzalez-Rosillo, K.J. Kim, Y. Zhu, Z.D. Hood, J.L.M. Rupp, Processing thin but robust electrolytes for solid-state batteries, Nat. Energy 6 (2021) 227–239.

[268] S.K. Otto, L.M. Riegger, T. Fuchs, S. Kayser, P. Schweitzer, S. Burkhardt, A. Henss, J. Janek, *In situ* investigation of lithium metal-solid electrolyte anode interfaces with TOF-SIMS, Adv. Mater. Interfaces 9 (2022) 2102387–2102396.

[269] M. Yousaf, U. Naseer, A. Imran, Y. Li, W. Aftab, A. Mahmood, N. Mahmood, X. Zhang, P. Gao, Y. Lu, S. Guo, H. Pan, Y. Jiang, Visualization of battery materials and their interfaces/interphases using cryogenic electron microscopy, Mater. Today 58 (2022) 238–274.

[270] J. Wan, Y.X. Song, W.P. Chen, H.J. Guo, Y. Shi, Y.J. Guo, J.L. Shi, Y.G. Guo, F. F. Jia, F.Y. Wang, R. Wen, L.J. Wan, Micromechanism in all-solid-state alloy-metal batteries: Regulating homogeneous lithium precipitation and flexible solid electrolyte interphase evolution, J. Am. Chem. Soc. 143 (2021) 839–848.

[271] Z. Liu, Q. Yu, Y. Zhao, R. He, M. Xu, S. Feng, S. Li, L. Zhou, L. Mai, Silicon oxides: A promising family of anode materials for lithium-ion batteries, Chem. Soc. Rev. 48 (2019) 285–309.

[272] R. Miyazaki, N. Ohta, T. Ohnishi, K. Takada, Anode properties of silicon-rich amorphous silicon suboxide films in all-solid-state lithium batteries, J. Power Sources 329 (2016) 41–49.